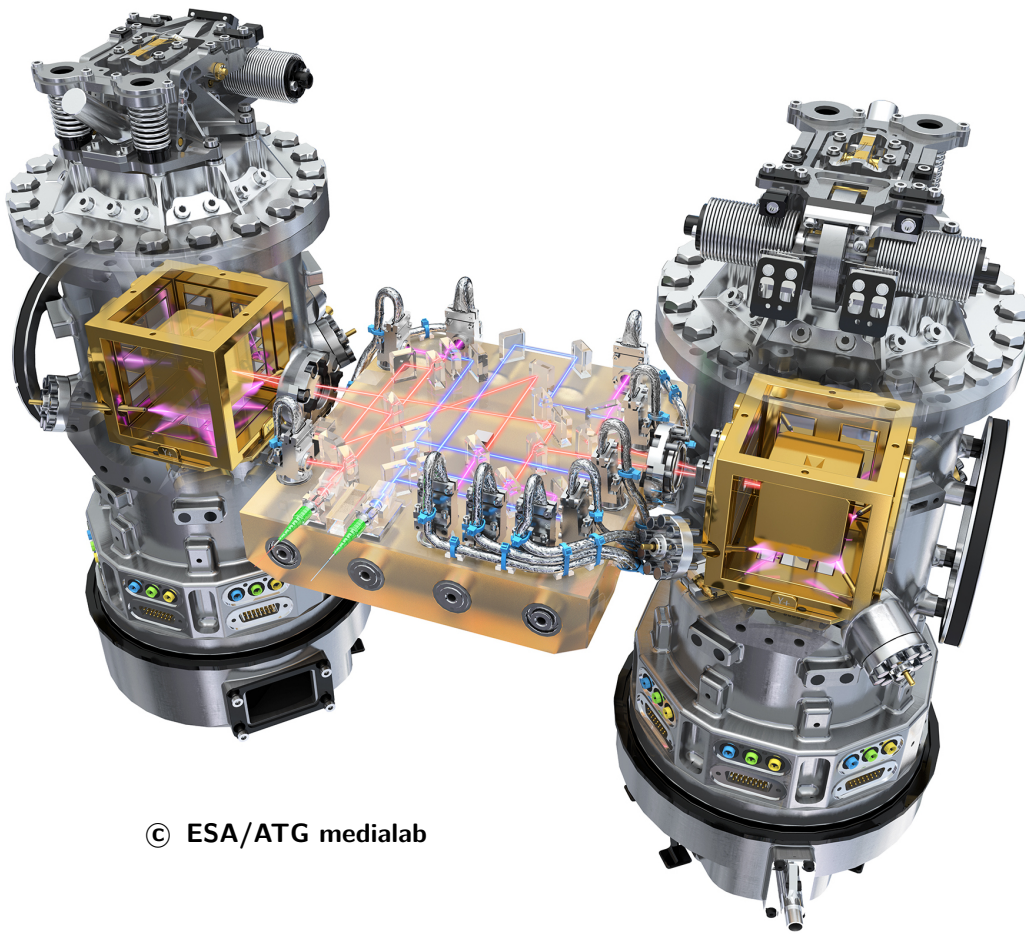




MAX PLANCK INSTITUTE FOR
GRAVITATIONAL PHYSICS
(ALBERT EINSTEIN INSTITUTE)

LPF Final Report for the German Contribution to the Nominal Mission



© ESA/ATG medialab

LPF Team, Germany



Title: LPF Final Report for the German Contribution to the Nominal Mission

Release date: June 25, 2018

Issue: 1

Status:

Organisations:

Max Planck Institute for Gravitational Physics

Albert Einstein Institute

Airbus DS GmbH

OHB System AG

Tesat Spacecom GmbH & Co. KG

For the Laser Interferometer Space Antenna (LISA)

Contents

List of Acronyms	x
List of Authors	xv
I. Introduction	1
1. Scope of the document	3
2. LISA Pathfinder: An overview	5
2.1. The Optical Metrology System	6
II. Development of mission operations	13
3. Operations concept	15
3.1. The operational environment	15
4. Software development	17
4.1. LTPDA	17
4.1.1. Development	18
4.1.2. Analysis Objects	18
4.1.3. The LTPDA Repository	18
4.1.4. Scale, Releases and Testing	19
4.2. The LPF Data Analysis Extension Module	20
4.3. Mock Data Challenges	21
5. Experiment design and the mission timeline	23
5.1. Experiments to results	23
5.2. Experiment Timeline	24
5.2.1. Week One	26
5.3. Simulation campaigns, Team building and training	30
5.3.1. STOC Exercises	31
5.3.2. STOC Simulations	31
5.3.3. LTPDA and data analysis training	33
III. In-orbit operations	35
6. Science operations	37
6.1. Introduction	37



6.2.	$\Delta g(t)$ calibration	37
6.2.1.	Further corrections on the $\Delta g(t)$ measurements	39
6.3.	Sensing Cross-Coupling	40
6.3.1.	The Cross Talk Problematic	40
6.3.2.	A Simple Time Dependent Cross Talk Model	41
6.3.3.	The Time Independent Cross Talk Model	42
6.3.4.	The Engineering Days Experiments	42
6.3.5.	Life Analysis of the Engineering Days Experiments	44
6.3.6.	Further Analysis of the Engineering Days	45
6.3.7.	Need for another Cross Talk Experiment	45
6.4.	Drift mode investigation	45
6.4.1.	The Goal and Design of the Experiment	45
6.4.2.	The working principle	46
6.4.3.	The drift mode during the nominal operations phase	46
6.4.4.	Data Analysis	47
6.5.	OMS vs GRS calibration	48
6.5.1.	Longitudinal calibration	50
6.5.2.	Angular calibration	51
6.6.	Laser frequency noise stabilisation and interferometer path length differences	60
6.6.1.	Laser Frequency Noise Stabilisation	60
6.6.2.	Measurements of Interferometer Pathlength Differences	60
6.6.3.	Conclusion	61
6.7.	Optical Pathlength Difference (OPD) noise investigations	62
6.8.	Relative Intensity Noise and interferometer path length differences	62
6.8.1.	Introduction	62
6.8.2.	Experiments	64
6.8.3.	Noise over position	65
6.9.	Differential Wavefront Sensing	69
6.9.1.	Introduction	69
6.9.2.	DWS in-orbit	71
6.9.3.	The DWS step experiment	73
6.10.	OMS timing investigation	78
6.10.1.	Optical Metrology System (OMS) science data timing	78
6.10.2.	Housekeeping (HK) data timing	79
6.10.3.	Mixed timing OMS Transfer Functions (TFs)	79
6.10.4.	Resampling artefacts	81
6.11.	Longterm monitoring of PD sensitivity and TM reflectivity	83
6.11.1.	Introduction	83
6.11.2.	TM reflectivity measurement	83
6.11.3.	Photodiode sensitivity measurement	85
6.12.	Long term monitoring of LTP hardware	88
6.12.1.	Introduction	88
6.12.2.	Monitored parameters	88
6.12.3.	The monitoring activities	90
6.12.4.	Results	92



Acknowledgements	93
List of Figures	95
List of Tables	99
Bibliography	99



List of Acronyms

AAF	Anti-Aliasing Filter
ADC	Analog-to-Digital Converter
AEI	Albert Einstein Institute in Hannover
ao	Analysis Object
AOM	Acousto-Optic Modulator
APC	AstroParticule et Cosmologie, Universite Paris Diderot
ASD	Airbus Space and Defence, Germany
ASU	Airbus Space and Defence, UK
ATC	UK Astronomy Technology Centre
CAD	Computer Aided Design
CET	Central European Time
CLG	Closed-Loop Gain
CLTF	Closed-Loop Transfer Function
CMM	Coordinate Measurement Machine
CMS	Charge Management System
Co-PI	Co-principal Investigator
COTS	Commercial off the shelf
DC	Direct Current
DDS	Data and Diagnostic Subsystem
DDS	Data Distribution System
DFACS	Drag Free and Attitude Control System
DFT	Discrete Fourier Transform
DLR	Deutsches Luft- und Raumfahrtzentrum (German Space Agency)
DMU	Data Management Unit
DWS	Differential Wavefront Sensing
ECSS	European Cooperation for Space Standardisation
EGSE	Electrical Ground Support Equipment



EH	Electrode Housing
EM	Engineering Model
EMP	Experimental Master Plan
ESA	European Space Agency
ESOC	European Space Operations Centre, Darmstadt, Germany
ETH	Eidgenoessisch-Technische Hochschule, Zuerich, Switzerland
FDIR	Failure/Fault Detection, Isolation/Identification and Recovery
FEE	Front-End Electronics
FF	Fast Frequency
FFT	Fast Fourier Transform
FIOS	Fibre Injector Optical Sub-Assembly
FM	Flight Model
FP	Fast Power
FPGA	Field Programmable Gate Array
FT	Fourier Transform
GRM	Ground Reference Model
GRS	Gravitational Reference Sensor/System
GSE	Ground Support Equipment
GUI	Graphical User Interface
HW	Hardware
HK	Housekeeping
iABG	Industrieanlagen-Betriebsgesellschaft mbH
ICE	Instrument Evaluation Configuration
IDL	Interferometer Data Log
IEEC	Institut d'Estudis Espacials de Catalunya, Barcelona, Spain
I/F	Interface
IIR	Infinite Impulse Response
IFO	Interferometer



ISS	Inertial Sensor Subsystem
KT	Kaiser Trede
L3	The 3rd L-class mission in the ESA Cosmic Vision Program
LA	Laser Assembly
LCA	LTP Core Assembly
LCU	Laser Control Unit
LISA	Laser Interferometer Space Antenna
LMU	Laser Modulator Unit
LPF	LISA Pathfinder
LTP	LISA Technology Package
LTPDA	LTP Data Analysis Software Toolbox
MOC	Mission Operations Centre
MPG	Max Planck Gesellschaft (Max Planck Society)
NASA	National Aeronautics and Space Administration, USA
NPRO	Non-Planar Ring Oscillator
OB	Optical Bench
OBI	Optical Bench Interferometer
OBC	Onboard Computer
OBT	Onboard Time
OGSE	Optical Ground Support Equipment
OLG	Open-Loop Gain
OLTF	Open-Loop Transfer Function
OMS	Optical Metrology System
OPD	Optical Pathlength Difference
OSTT	On-Station Thermal Tests
PD	Photodiode
PFM	Proto-Flight Model/Pre-Flight Model
PI	Principal Investigator



PM	Phasemeter
PMU	Phasemeter Unit
PRDS	Phase Reference Distribution System (for laser interferometry)
PT	Phase Tracking
PZT	Piezo-Electric Transducer
QPD	Quadrant Photodiode
RAM	Random Access Memory
RF	Radio Frequency
RIN	Relative Intensity Noise
RLU	Reference Laser Unit
RMS	Root Mean Square
RS	Requirement Specification
SBDFT	Single-Bin Discrete Fourier Transform
SC	Spacecraft
SDP	System Data Pool
SEPD	Single Element Photodiode
SF	Slow Frequency
SID	System Identification
SNR	Signal-to-Noise Ratio
SoW	Statement of Work
SP	Slow Power
SRD	Science Requirement Document
SSC	Source Sequence Counter
SSM	State Space Model
SSMM	Solid-State Mass Memory
STOC	Science Technology Operations Centre
SW	Software
TBC	To Be Confirmed



TBD	To Be Defined
TC	Telecommand
TF	Transfer Function
TIA	Trans-impedance Amplifier
TM	Test Mass
TMS	Test Mass Simulator
TN	Technical Note
TRR	Test Readiness Review
UGL	University of Glasgow, UK
UOB	University of Birmingham
UTN	University of Trento, Italy
VEGA	<i>Vettore Europeo di Generazione Avanzata</i> , Italian for Advanced Generation European Carrier Rocket
WBS	Work Package Breakdown Structure
WP	Work Package
w.r.t	with respect to



List of Authors

Name	Organisation
Karsten Danzmann	AEI
Gerhard Heinzl	AEI
Martin Hewitson	AEI
Jens Reiche	AEI
Michael Tröbs	AEI
Gudrun Wanner	AEI
Michael Born	AEI
Heather Audley	AEI
Nikos Karnesis	AEI
Andreas Wittchen	AEI
Sarah Paczkowski	AEI
Brigitte Kaune	AEI
Lennart Wissel	AEI

Part I.

Introduction

1. Scope of the document

This document presents the work and results of the LISA Pathfinder (LPF) mission, from the development phase (phase B/C) through to the end of the nominal mission (phase E). It has been prepared by the Max Planck Institute for Gravitational Physics (Albert Einstein Institute), Hannover, Germany, with support from Airbus DS GmbH, OHB Systems AG and TESAT Spacecom GmbH & Co. KG.

2. LISA Pathfinder: An overview

The Laser Interferometer Space Antenna (LISA) is a cornerstone mission of the European Space Agency (ESA) and is planned to be the first space-based gravitational wave observatory. It will detect gravitational waves in the frequency range of 10^{-5} to 1 Hz, lower frequencies than are detectable with ground-based observatories. LISA is due to be developed within the European Space Agency's (ESA) Cosmic Vision Program as the third large mission (L3), with launch foreseen around 2034.

In order to demonstrate the feasibility of the LISA mission, a technology demonstration mission, LISA Pathfinder (LPF), was designed. It aimed to demonstrate some of the key technologies required for the future space-based gravitational wave detector, LISA, including:

- the ability to maintain a test mass in free-fall such that it follows only the local geodesics of spacetime. For this purpose, the following items were developed:
 - inertial sensors to shield the test masses from disturbances, and including local read out and actuation based on electrostatics.
 - the caging mechanism to hold the test masses securely during the high mechanical launch loads and to release them in a controlled way.
 - the Drag Free and Attitude Control System (DFACS).
 - the charge management system.
- the use of interferometry with picometre precision.
- the use of microNewton thrusters.

After more than ten years of development, the LPF satellite was launched on the 3rd of December 2015 at 5.04 CET onboard a VEGA rocket from Europe's space mission launch centre in Kourou, French Guiana. The final LPF orbit was a Lissajou orbit around the L1 Earth-Sun Lagrange point. In this orbit, the satellite was around 1.5 million km from the Earth, and at a near constant separation and orientation relative to the Sun. This allowed operation in a very stable thermal and mechanical environment.

After the satellite reached its orbit around L1 there followed one month of spacecraft commissioning, three months of LISA Technology Package nominal operations and three months of the USA's Disturbance Reduction System (DRS) nominal operations and a period of extended mission.

LISA Pathfinder, shown in Figure 2.1, is built around two free-floating test masses, one is in free fall while the other is actuated to follow the first, acting as a drag-free reference for the satellite. The main mission objective was to verify and analyse the drag-free performance of the test masses at the level of spurious accelerations below a requirement of $3 \cdot 10^{-14} \text{ m s}^{-2}/\sqrt{\text{Hz}}$ at mHz frequencies, thereby demonstrating the functionality of the

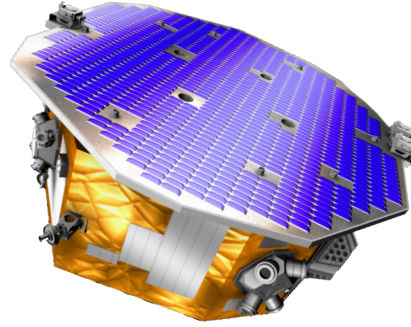


Figure 2.1.: An artist's impression of the LISA Pathfinder satellite. Image courtesy of ESA.

associated drag-free spacecraft control. The first results were published in [1], and showed performance levels exceeding the requirements by a large factor.

Located at the core of the LISA Pathfinder satellite, the LISA Technology Package (LTP), shown in Figure 2.2, is the main measurement system. It includes the two test masses, each of which is inside an electrode housing and a vacuum tank, as well as the Optical Metrology System (OMS), the first precision laser interferometer in Space. The OMS provides the input to the Drag Free and Attitude Control System (DFACS) that maintains the free-fall condition of test mass one (TM1) and the suspended condition of test mass two (TM2).

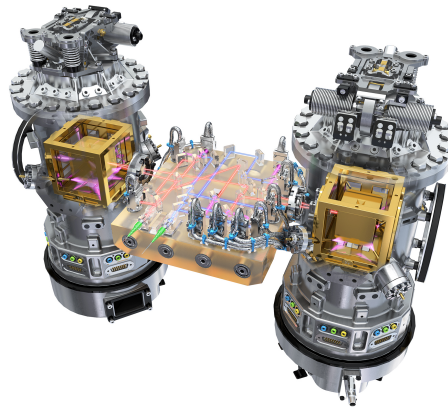


Figure 2.2.: A CAD rendering of the LISA Technology Package, which comprise the test masses and the subsystems required for the interferometric readout of six degrees of freedom. Image courtesy of ESA and ATG medialab.

2.1. The Optical Metrology System

The Optical Metrology System comprises the subsystems that are required for the continuous, low noise readout of six degrees of freedom:

- the displacement of test mass one (TM1) relative to the spacecraft, x_1

- the displacement of test mass two (TM2) relative to test mass one , x_{12}
- the angular fluctuations of TM1, ϕ_1 and η_1
- the angular fluctuations of TM2, ϕ_2 and η_2

These parameters are defined relative to the axis connecting the two test masses, as shown in Figure 2.3. A block diagram showing the subsystems that make up the OMS is shown in Figure 2.4.

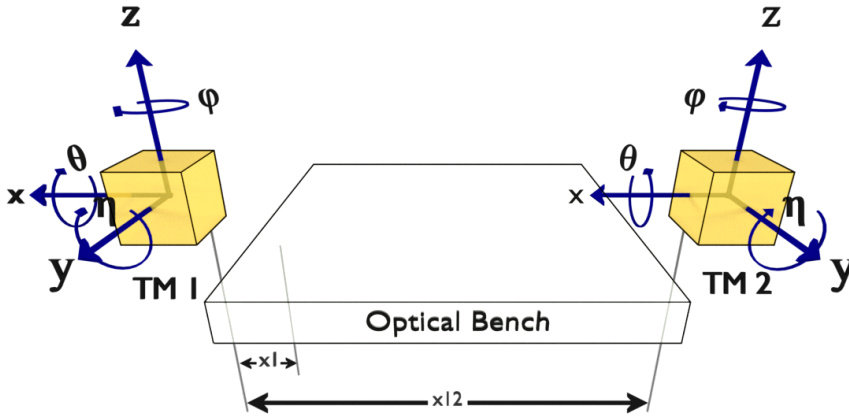


Figure 2.3.: Shown is a schematic view of the optical bench surrounded by the two test masses. The x_1 interferometer measures the change in distance between the optical bench and test mass one. The differential x_{12} interferometer measures the relative change in distance between the two test masses. Rotations around the z and y axis are measured via Differential Wavefront Sensing (DWS), yielding ϕ and η for each test mass.

The Reference Laser Unit (RLU), containing a single ND:YAG NPRO laser, produces a 1064 nm beam which is transmitted via a single-mode optical fibre to the Laser Modulation Unit (LMU). The beam is split into two parts of equal power via a beamsplitter. Each of these beams passes through an Acousto-Optic Modulator (AOM), and is frequency shifted to give a relative frequency difference of $+f_{\text{het}}=1$ kHz. These beams are now referred to as the measurement and the reference beam respectively. They are coupled onto the optical bench via polarisation-maintaining fibres and fibre couplers (It should be noted that the fibre for the reference beam longer than the fibre for the measurement beam to account for differences in the beam paths on the optical bench), and are collimated and near Gaussian. On the optical bench, the measurement and reference beams form four interferometers, as shown in Figure 2.5:

- X1 (1): The X1 interferometer is used to measure the displacement and angular fluctuations of TM1.

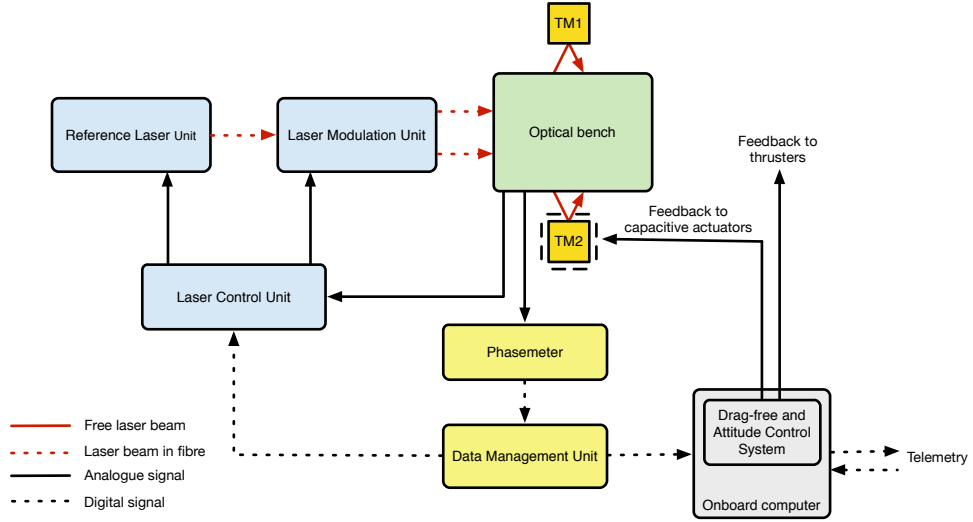


Figure 2.4.: A block diagram showing the subsystems that make up the Optical Metrology System in blue, green and yellow. The grey boxes show the link between the OMS outputs and the Drag-Free and Attitude Control Systems (DFACS).

- X12 (12): The X12 interferometer measures the displacement and angular fluctuations of TM2 relative to TM1.
- Reference (R): The reference interferometer output is subtracted from the other interferometers during processing in the DMU in order to suppress common mode noise that originates before the beams are input onto the optical bench. It also provides the input signal to the Optical Pathlength Difference (OPD) control loop. This loop provides feedback to two PZT actuators in the LMU, one in the path of each beam, which act to adjust the relative pathlengths.
- Frequency (F): The frequency interferometer has an intentional pathlength difference between the two beams in order to allow laser frequency noise to be suppressed via the frequency control loop (see Section 6.6.1). This is a nested loop, with a ‘fast’ part that controls a PZT actuator on the laser crystal, and a ‘slow’ part that acts on the laser crystal temperature.

Additionally, a small fraction of each beam is split off by a beamsplitter directly after it is input onto the optical bench and is measured by the equivalent of a single-element photodiode (SEPD). These signals are used as a measure of the beam power, and are the inputs to the power control loops. These loops, one for each beam, act on the radio frequency (RF) input of the AOM, and adjust the amount of light diffracted into each beam.

The output from each interferometer is read out by two InGaS quadrant photodiodes, a nominal photodiode (A) and a redundant photodiode (B). The photocurrent from each quadrant becomes the input for the Phasemeter Unit (PMU). In the PMU, the photocurrent is converted to a voltage by a trans-impedance amplifier (TIA), low-pass filtered, and then digitised by an analogue-to-digital convertor (ADC). A single-bin discrete Fourier Transform (SBDFT) is then performed at the heterodyne frequency, f_{het} . The real and imaginary

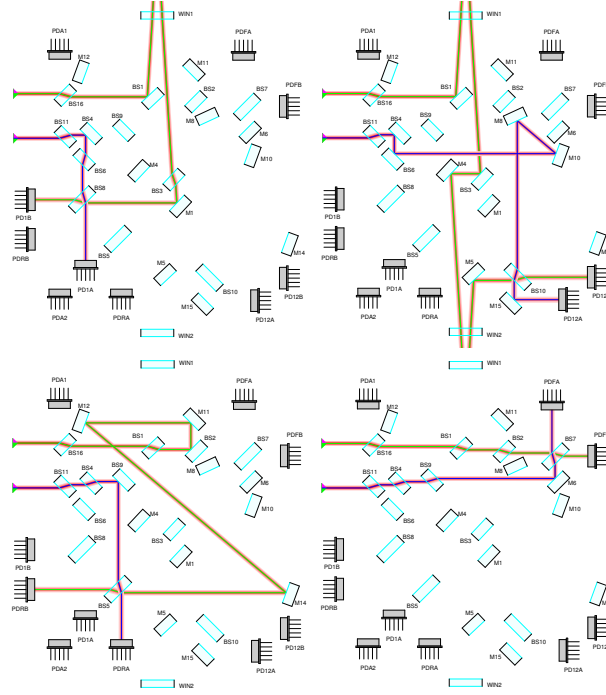


Figure 2.5.: The four interferometers on the OB shown separately. TM1 is above the top and TM2 below the bottom of each picture. Top left: x_1 , top right: x_{12} , bottom left: Reference and bottom right: Frequency.

components of the SBDFT at the heterodyne frequency, $z_{i,\hat{j},k}$ and $y_{i,\hat{j},k}$, as well as the dc (mean) value, $d_{i,\hat{j},k}$, are the output signals from the phasemeter. In the notation used here, i represents the interferometer (1, 12, F, R), \hat{j} represents the respective photodiode quadrant (\hat{A} , \hat{B} , \hat{C} , or \hat{D}), and k is A or B for the nominal or redundant photodiode respectively. These values, one for each channel of each interferometer, become the inputs for the Data Management Unit (DMU).

The processing that takes place in the DMU to calculate the main scientific measurements is shown in full in Figure 2.6. The $z_{i,\hat{j},k}$, $y_{i,\hat{j},k}$ and $d_{i,\hat{j},k}$ signals from the PMU are converted from integer to floating point numbers, scaled with c-coefficients before quadrant relabelling is applied to ensure the correct pairing of the nominal and redundant photodiode quadrants in each interferometer. Based on the quality of the output from each photodiode quadrant, channel selection is used to determine which photodiodes will be used in the subsequent calculations. Under nominal conditions, the mean value of the nominal and redundant photodiodes will be used for the calculation of the main science outputs:

- **displacements:** The raw phase of the signal in each interferometer, φ_i , is calculated from the real and imaginary components of the SBDFT. A phase tracking algorithm is applied in order to track test mass displacements larger than π , and the reference interferometer output is subtracted from the other interferometer outputs to give the processed phase, Ψ_i . By taking into account the geometry of the beams incident on

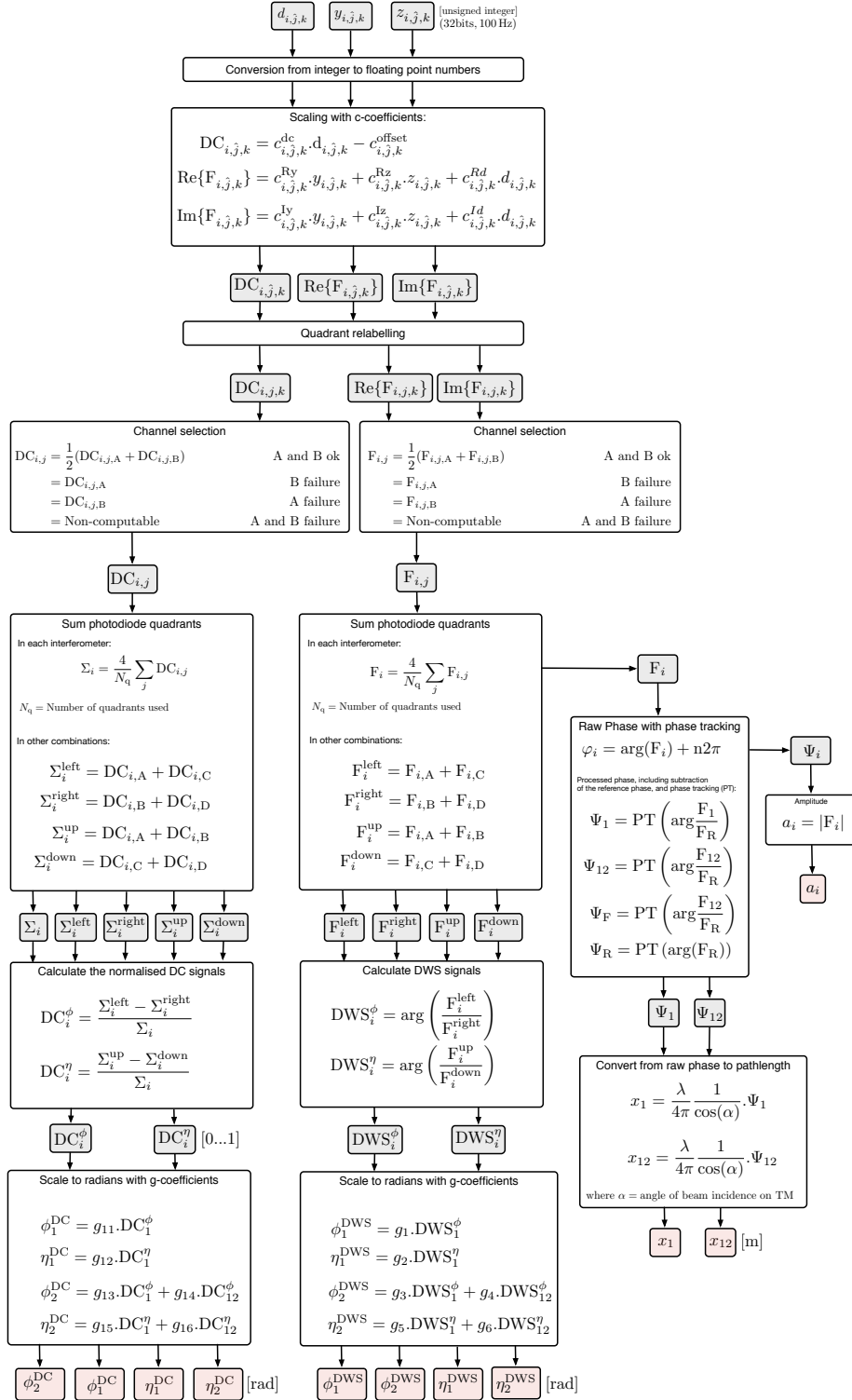


Figure 2.6.: A flow chart depicting the signal processing in the DMU [2] [3] [4].



the test masses, the Ψ_1 and Ψ_{12} processed phase signals are converted to pathlength to give the required x_1 and x_{12} displacements.

- **Angular test mass motions:** There are two methods used to calculate the ϕ and η test mass angles:
 - **Differential Power Sensing (DPS)**, also referred to as DC: The DPS provides a rough estimate of the centre of the beam power on the photodiode. These values are used to provide a rough alignment signal for each interferometer, where the horizontal misalignment of each TM, $\phi_i^{\text{DPS}}/\phi_i^{\text{DC}}$, is determined by calculating the normalised difference in the mean power between the left and right sides of the photodiode. Similarly, the vertical misalignment of each TM, $\eta_i^{\text{DPS}}/\eta_i^{\text{DC}}$, is determined from the normalised difference in the mean power between the top and bottom of the photodiode.
 - **Differential wavefront sensing (DWS):** Differential Wavefront Sensing (DWS) is an interferometric measurement technique which uses the relative tilt of the interfering wavefronts in each interferometer to calculate the angle of the test masses. These angles drive the Drag-Free Attitude Control System (DFACS) when the spacecraft is in nominal science mode. The x_1 interferometer is used to derive the test mass one angles ϕ_1^{DWS} and η_1^{DWS} . For test mass two, the differential x_{12} readout is combined with test mass one angles to calculate ϕ_2^{DWS} and η_2^{DWS} . This is done by demodulating the individual segments of Quadrant-Photodiodes (QPD) to compare the relative phase difference between the wavefronts of the interfering measurement and reference beams for groups of two complementary quadrants per photodiode. This is described in detail in 6.9.1.

Part II.

Development of mission operations

3. Operations concept

During the science operations phase, sequences of experiments were carried out with the aim to establish a detailed physical model of the system, while at the same time bringing the system to the optimal operating point where the purest level of free-fall could be achieved. To do this, teams of scientists took shifts at the European Space Operations Centre (ESOC) in Darmstadt where they analysed the data as it came down from the satellite and scheduled the experiments that followed. Due to the short mission life-time, all experiments were planned and tested in advance and arranged into short, medium and long-term plans. The short-term plan constituted 7 days of science operations time-line which could be executed autonomously onboard the satellite. Planning what comes next required the experiment of the previous days/weeks to be analysed promptly in order to inform the up-coming schedule. In addition to these front-line analysis teams, other members of the LISA Pathfinder science community were co-located at remote data centres (such as the one established at the APC in Paris) where they could combine their skills and experience to perform deeper analysis of the data.

The analysis of the experiments under such time-pressure requires a number of elements to be in place. A robust data analysis toolbox is needed so that confident decisions can be made based on the results as they arrive. An easy data access system is needed to allow the scientists fast and concurrent access to the raw data as it comes off the satellite, as well as to provide a centralised storage system where analysis results can be exchanged and archived. For each investigation that will be executed on-board, simulations will need to be run to validate the command sequences and the expected system behaviour, and analysis procedures will need to be developed to allow the scientists on-duty to step through the analysis and deliver the results needed to answer the operational questions of the day.

The planning of mission operations for LISA Pathfinder required development and work in a number of areas, and these are discussed in the following chapters.

3.1. The operational environment

The operational environment for LISA Pathfinder required the bringing together of three teams: The mission control engineers (MOC), the ESA Science Operations engineers (STOC), and the science data analysis team. By ensuring a tight interaction between the teams, including common-tools, co-location during operations, and common training forming a common language, the science operations of LPF ran extremely smoothly, where all involved were able to adapt to new situations and incoming results in a robust and dynamic manner.

Understanding the operations environment can best be done by following the data through the entire process. Figure 3.1 shows schematically how the data flows down from the satellite into the STOC where it is converted into the format used by the data analysis tools and ingested into a database where it can be accessed by the data analysis teams on duty. In the other direction, the flow of generation of commanding is shown, where the experiment

design originates from the scientists, is processed by operations engineers, and eventually (after going through the validation and testing cycle discussed in Section 5.2) ends up as a sequence of commands sent to MOC for upload to the satellite.

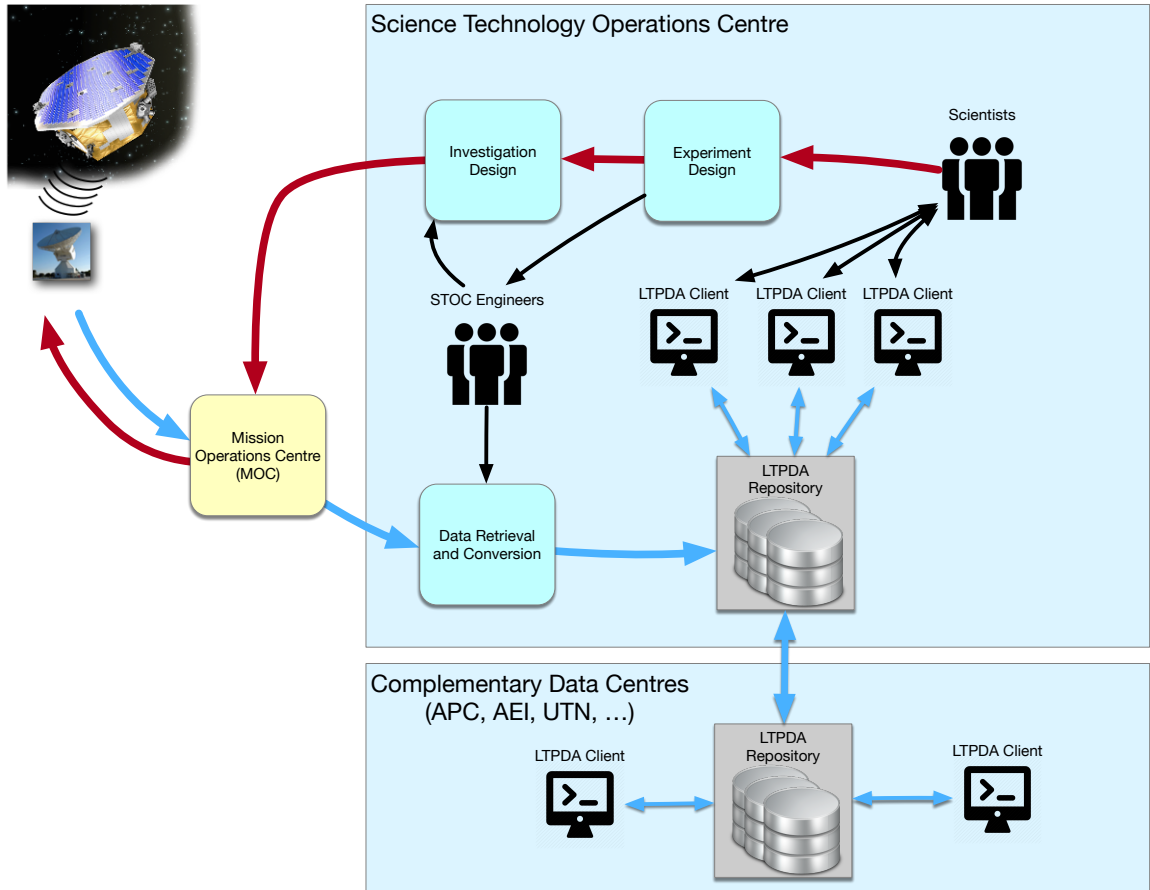


Figure 3.1.: A schematic view of the data flow and responsibilities and interactions between STOC, MOC and the scientists.

4. Software development

The primary software development was focussed on the core LTPDA Toolbox, a MATLAB toolbox implementing an object-oriented data analysis framework with full tracking of all operations and a rich feature set tailored to instrument data analysis. On top of this, mission specific functionalities were added in the form of an extension module for LTPDA.

4.1. LTPDA

The need to perform quasi online data analysis in a robust and flexible way led to a series of requirements on the data analysis software. In particular, the software needed to be user-friendly, thoroughly tested, and able to cope with on-the-fly analysis design.

The need to have accountable and reproducible analysis results to avoid information loss between LPF and LISA, was also identified. The aim was to avoid having analysis results in the form of plots/figures/documents without full details of the supporting analysis. In addition, in order to ensure that the data and results of the mission have a long life time, they were to be stored to disk in an ASCII file format.

Since contact with the spacecraft was limited to a few hours per day, a limited amount of time was available between receiving the data from a particular experiment and uploading of tele-commands to alter the mission timeline based on the results of that experiment. Hence, the data from the last experiment needed to be analysed quickly so that any necessary action could be taken to optimise the subsequent experiments. To speed up the analysis, multiple scientists needed to access and analyse the data in a concurrent way. As such, a centralised data repository was implemented to deliver and receive data analysis products.

In order to perform the data analysis for LTP a software tool was been developed to meet the demanding requirements discussed above. This tool is referred to as LTPDA (see [14] for a high-level description). It is a MATLAB[®]¹ toolbox which implements an object-oriented data analysis environment composed of different classes: user-classes which can be manipulated by the user, and non-user-classes which provide the supporting framework. Each *user* class represents a different LTPDA object, for example, the `ao` class implements the functionality of Analysis Objects described below.

LTPDA includes algorithms and objects for:

- pre-processing of time-series data;
- performing spectral analysis of various kinds;
- performing digital filtering via IIR and FIR filters;
- constructing pole/zero models;

¹MATLAB itself is a commercial software product by Mathworks[®] for numerical computing.



- constructing state-space models;
- system identification and parameter estimation;
- and much more.

4.1.1. Development

The development of LTPDA started in 2007 as a combined work of the AEI, the University of Trento (Italy), ICE in Barcelona (Spain), ATC in Paris (France), with contributions from other institutes within the LPF community, and continued right up to, and throughout the mission science operations. The development team was run and coordinated from the AEI, and employed a central source control repository (CVS then later GIT), continuous integration (via a dedicated test machine and a mix of test-driven development and function driven development). The team was typically composed from about 20 scientific researchers, with full-time additional support of at least one software engineer, and part-time support from testing engineers.

The software can be found under the following web page <https://www.elisascience.org/ltpda/> and the latest version used during the mission operations can be found under git@gitlab.aei.uni-hannover.de:ltpda/ltpda_lpfops.git.

LTPDA is a MATLAB toolbox that uses an object-oriented approach to data analysis. LTPDA Objects are processed through a data analysis pipeline. At each analysis step, a record is kept of exactly what algorithm was applied to which object and with which parameters. In this way, the result of a particular data analysis is one or more objects, each containing the final result as numerical data together with a full processing history of how the result was achieved.

The latest version by February 2017 is V2.94.

4.1.2. Analysis Objects

The requirement to have accountable and reproducible data analysis products led to the concept of Analysis Objects (AOs). An AO aims to capture much more than just numerical data. For example, an AO may represent a time-series, and as such will contain a vector of time-stamps and a vector of data values, together with additional information, like a sample rate and a start time, and most importantly, a full account of any processing steps that the object has gone through.

Keeping all this information together in this compact form allows analysis results to be viewed, reproduced, reused, or inspected at a later date. This concept is developed further to include other types of objects (not just numerical data objects), like digital filters, parametric models, and different transfer function representation. The tracking of the full processing history requires that all analysis algorithms properly deal with the history of any input AOs.

4.1.3. The LTPDA Repository

As described above, it was a requirement of the mission to have a data distribution scheme that allowed concurrent access to the mission data. For this, the LTPDA team developed the LTPDA Repository. Such a repository consists of a central database server in which

LTPDA objects and associated meta-data can be stored. These objects can be searched for, submitted, and retrieved directly from within MATLAB using LTPDA toolbox functions.

In addition, the repository has a web-interface which can be used by administrators to manage databases and users, as well as by users to search for, view, and retrieve LTPDA objects via a web browser.

Multiple LTPDA Repositories are installed in various institutions involved in LPF. They are in daily use and currently store 10's of thousands of LTPDA objects. During mission operations, a number of LTPDA repositories were also installed at ESA's STOC in a high redundancy scheme, ensuring continuous access to the mission data for the scientists involved in the operations. All raw data downloaded from the satellite was converted each day to AOs and uploaded to daily databases within the LTPDA repositories. The results from different analysis, as well as derived data products, were also stored in these repositories. Figure 4.1 shows a screenshot of one of the STOC repositories at the end of operations.

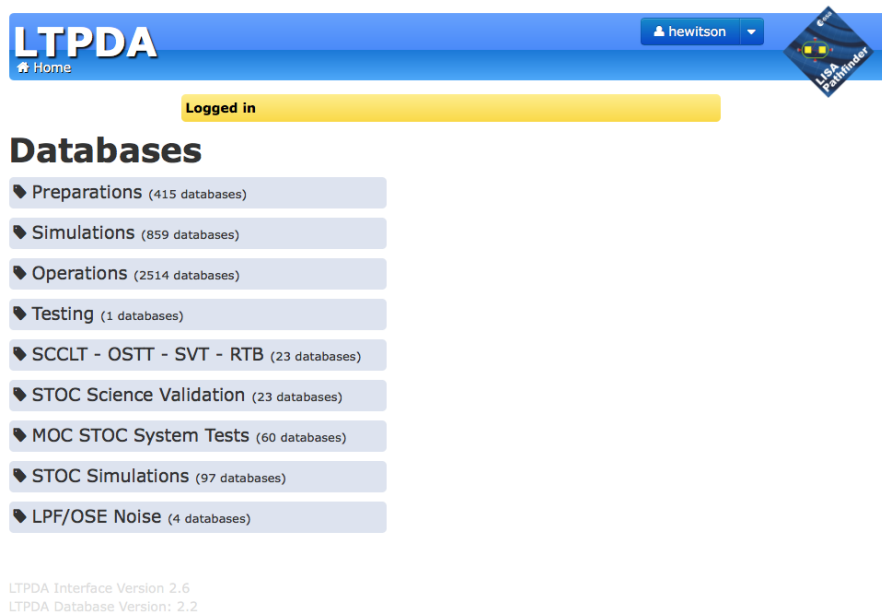


Figure 4.1.: A view of the main web interface of one of the operational LTPDA repositories, showing the large number of databases populated and used throughout mission development and operations.

4.1.4. Scale, Releases and Testing

Since the development began at the beginning of 2008, the LTPDA team has released about 50 versions, together with various snapshot versions, and a number of formal deliveries to ESA for use in the STOC. During mission operations, a dedicated delivery scheme was put in place to ensure scientists on duty could have access to the latest version of the software without introducing instabilities in the code. This involved the setting up of a Change

Control Board (CCB) to review and monitor any changes to the toolbox, and the continuous running of unit and system tests, discussed below.

During this time, the development team has also written over 13000 unit tests which are run every few hours on dedicated test machines. A number of the releases are designated as deliverables to ESA. For these releases, we also carry out system testing campaigns. Such a campaign typically involves make a few release candidates, each of which is tested by a team of professional system testing engineers. During the campaign it is the job of the development team to track and fix, where possible, any bugs submitted by the system testers. During development the LTPDA team delivered 3 versions to ESA and carried out 3 system testing campaigns. As such, the LTPDA toolbox can be considered to be in a mature state; it consists of about 200,000 lines of MATLAB source code and includes about 240 methods (functions) in the AO class alone. It has a comprehensive user-manual currently running to around 700 pages. Altogether, the toolbox development represents at least 20 man-years of development time.

Figure 4.2 shows a graphical view of the GIT repository activity in terms of numbers of commits per month over the course of the development of LTPDA. Figure 4.3 shows the number of lines of code in the core toolbox over the period of development, showing both the scale of the project and the development activity. Figure 4.4 gives an alternative view of the development activity, this time showing the commits to the git repository grouped by institution, clearly showing the significant effort located at the AEI.

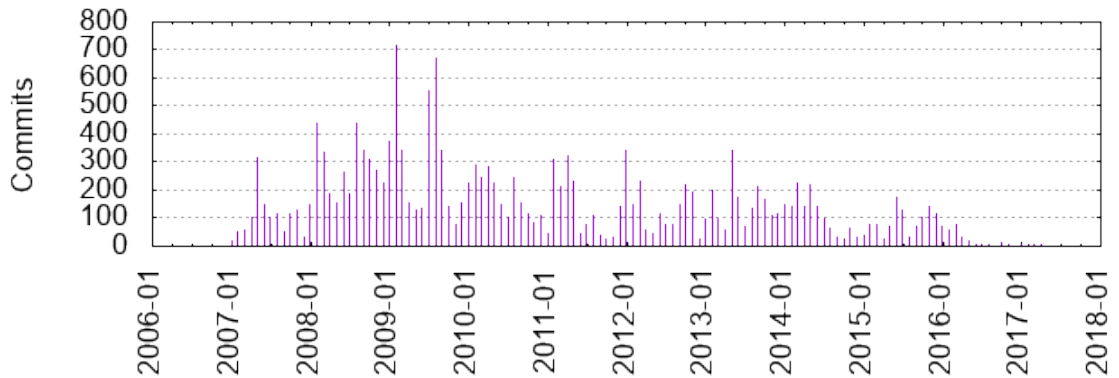


Figure 4.2.: Commits to the LTPDA git repository per month over the course of the development of LTPDA.

4.2. The LPF Data Analysis Extension Module

It was quickly recognised in the early days of developing LTPDA that the toolbox was more generally useful than just for LPF. As such, the core LTPDA toolbox was, from the beginning, released to the public. To allow end users to develop domain-specific functionality within LTPDA, the team implemented an extension module feature in the toolbox. This allows end users to tailor the toolbox to their own needs, extending the functionality through new methods, new classes or any other MATLAB based routines. One such extension was

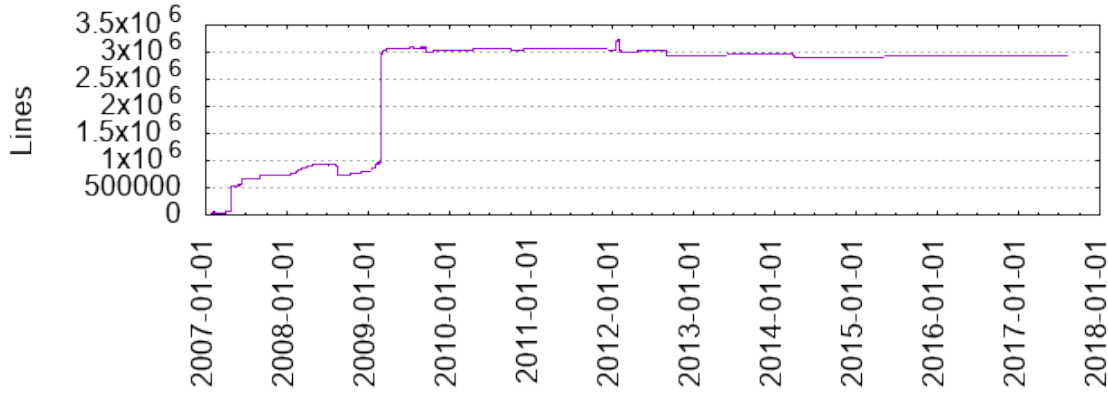


Figure 4.3.: Lines of code in LTPDA over the course of the development.

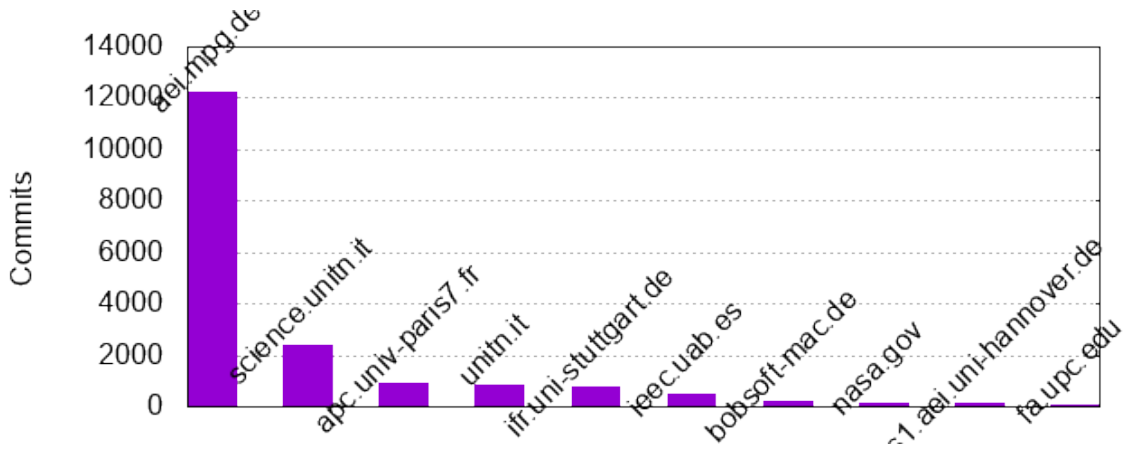


Figure 4.4.: The number of commits to the LTPDA git repository grouped by institution.

developed by the LISA Pathfinder Data Analysis team – The LISA Pathfinder Data Analysis Module (LPF_DA_Module).

4.3. Mock Data Challenges

Creating a data analysis toolbox to do ‘general’ instrument data analysis results in a very broad scope. To help identify the most important algorithms needed for the analysis of the LPF experiments, a series of Mock Data Challenges (MDCs) were initiated. By simulating some of the key experiments that were intended to run on LPF, the team was able to both develop a common description of these experiments and the analysis needed for them, and to design and implement a number of key algorithms needed. It also allowed for the identification, implementation and testing of a large suite of ‘standard’ analysis tools, ensuring that the development was focussed in the correct areas. More details on the MDCs can be found in [14, 15, 16, 17].

5. Experiment design and the mission timeline

5.1. Experiments to results

A number of steps are required to go from the concept of a physical experiment to the actual execution on board the satellite, and then the subsequent data analysis. The main aspects of this process are described below.

Experiments Design of each top-level experiment, such as system identification of x -axis parameters. This is a physical description of the experiment to be performed

Design investigations Design one or more investigations to implement the experiment on the satellite. This involves definition of the environment on the satellite, translation of physical experiment into a set of commands which can be executed on-board, and definition of the experiment timeline.

Implement investigations Having a design for an investigation on paper is only the first step. Following this, the investigation had to be implemented in the Mission Planning tool at ESA's Science Technology Operations Centre (STOC). During that process, all commands and their parameters are verified against the mission database. Usually a period of iteration follows to ensure the correct and implementable investigation design.

Simulated data Having an investigation implemented in the STOC means that a mock commanding timeline can easily be produced and fed through the mission simulator to produce a set of simulated data. Often during this design process, different simulated data sets were produced allowing for iteration and optimisation of the investigation design following inspection of the data.

Analysis Procedure Once an investigation is implemented and simulated at STOC, there follows a period of design work to identify the analysis that should be done. This does not involve writing code yet, but rather producing a procedural, algorithmic, mathematical description of the analysis, starting from the raw data produced by the investigation, and ending in a definition of the output analysis products. The aim of such documents was to produce a baseline on which a pipeline could be designed, and a prescription of the actions to take when doing this analysis on-line during operations.

Design pipeline The abstract description of the analysis needed for a particular experiment needs to be realised in an actual analysis pipeline. Within LTPDA, a data analysis pipeline infrastructure was developed to allow for the chaining together of logical units of analysis into complete and complex pipelines. Such logical units of analysis are



called pipeline steps, and where possible, the design of these steps was done to ensure maximum reusability across pipelines. An example pipeline is shown in Figure 5.1.

Implement pipeline Implementation of a pipeline involves identification of the pipeline steps, and then implementation of adaption of existing steps for this case. Bringing the steps together, and defining the top-level interface results in an implemented pipeline.

Driver script Running a pipeline is done via a so-called ‘driver script’. Pipelines themselves are highly configurable, allowing them to adapt to the experimental data as it is being analysed. But before flight we established baseline parameterisation of each pipeline based on simulation campaigns. The driver scripts associated with each pipeline capture this baseline configuration, and allow for rapid implementation and running during operations.

Test cases As in all aspects of the data analysis software in LPF, pipelines also need to be carefully tested. At the lower level, each pipeline step can be tested, ensuring a robust basis for building pipelines out of these individual elements.

System tests Due to the complex nature of these pipelines, we decided upon a series of simulation campaigns as the best way to exercise all aspects of this process, from experiment design, investigation design, through data analysis. These campaigns also provided the perfect environment for training the team. See Section 5.3 for more discussion on this aspect.

Most of these activities were organised and directed from within the Data Analysis team, for which the AEI had the lead. The work involved the whole data analysis team, a collaboration of about 30 scientists from various institutions of the LISA Pathfinder collaboration. Figure 5.2 shows this development process in a graphical form.

5.2. Experiment Timeline

The experiment timeline was the core element that coordinated the daily science operations of the mission. The timeline is built from a sequence of investigation and configuration blocks. Each investigation block encapsulates a set of commands that carry out the particular experiment we want to perform, whereas a configuration block sets the system in to a particular state, for example switching to a particular DFACS mode, or setting a particular actuation authority. So the block sets up the environment for the experiment, and the investigation details the commanding needed.

The process to go from an experiment concept to a sequence of commands that can run on the satellite required many steps with a lot of validation and testing along the way. Assembling the experiments into a mission plan (a timeline) was done at a high level in the science team, resulting in coherent blocks of activity of about one week in length. Each weekly plan was then simulated (often multiple times) on the mission simulator to ensure correctness of the commanding, the data returned, and, via analysis, the experiment designs.

Figure 5.3 indicates the steps needed to take an experiment plan from concept through to execution. The members of the science team initiate the process with an experiment concept. This is then passed to the project scientist for review. The plan is then assigned a

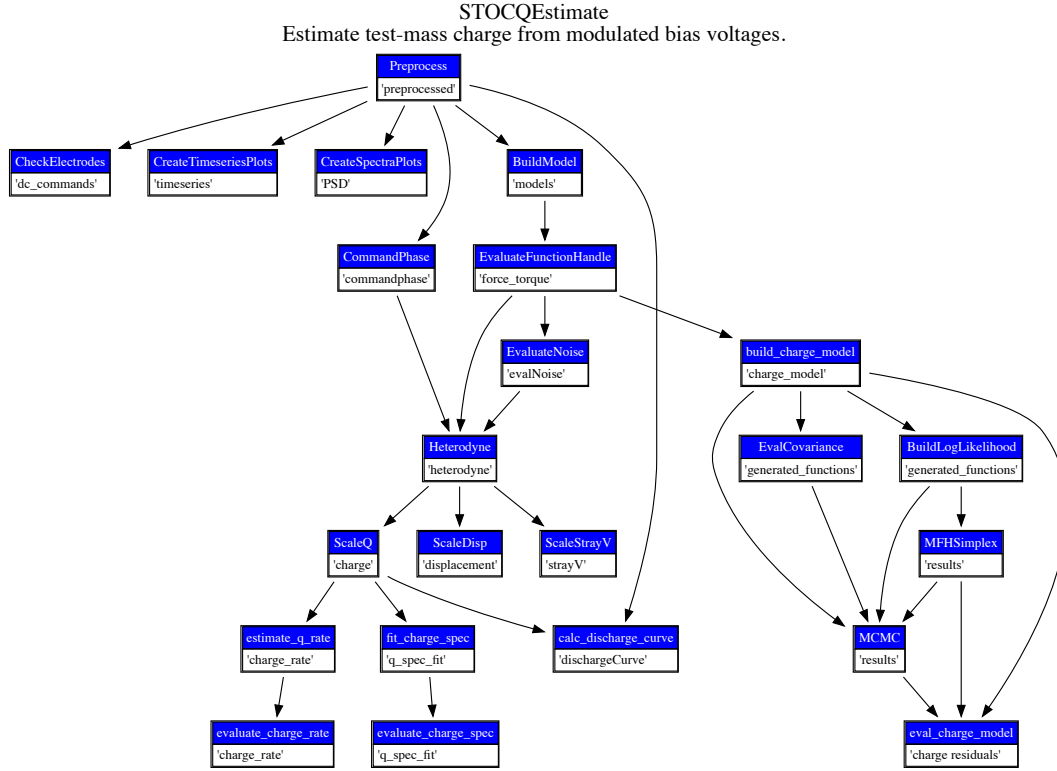


Figure 5.1.: An flowdiagram of one of the pipelines used during science operations. This particular pipeline describes the analysis needed to estimate the charge on each test mass having performed the associated investigations on-board.

required level of validation. For example, reuse of existing investigations in a similar context need only functional verification, whereas new investigations or new contexts require full simulation. The plan is then implemented in the planning tool at the STOC. The tool then outputs an intermediate description of the plan in a so-called ISIF file to allow review of the implementation by the project scientist (and often delegated to the science time). If any discrepancies were found, an iterative process would begin to identify and correct them. Once that process is completed, the Payload Operations Request (POR) could be generated, and passed to the simulator for execution, if needed. When fully validated, the POR would be sent to the Mission Operations Centre (MOC) for scheduled upload to the satellite.

A wealth of different experiments were designed for the mission, each one being broken down into its requisit investigations and configurations. Figure 5.4 shows the collection of investigations into experimental topics for the entirety of the nominal mission phase. During this time, 85 unique investigations were executed, using 31 unique configuration blocks.

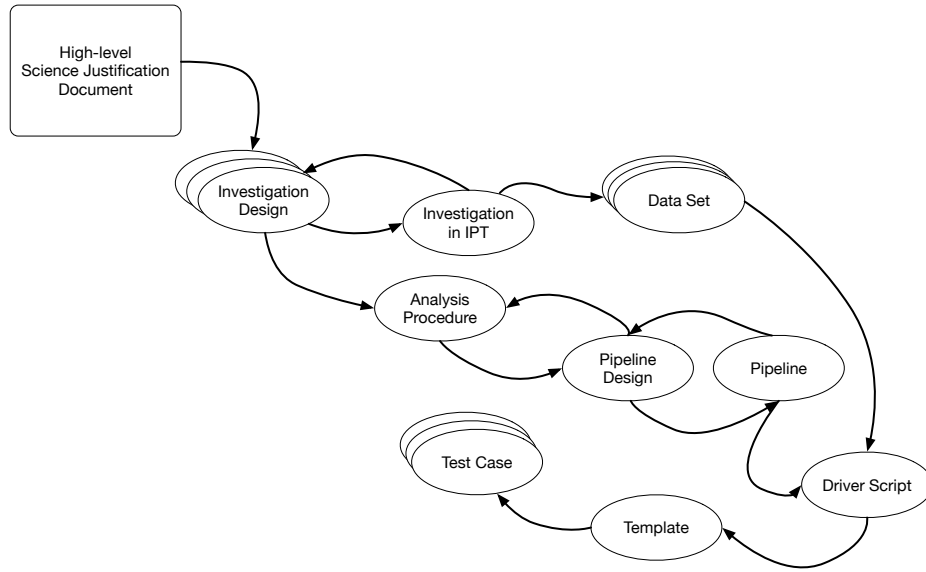


Figure 5.2.: A process flow of the steps needed to go from a conceptual physical experiment through a series of investigations executed on the satellite and finally to the data analysis results. Each of the boxes represents a Pipeline Step, and all flows shown in the diagram can be executed via dedicated driver scripts.

5.2.1. Week One

To give a flavour of the complexity involved in running the diverse and interleaved sequence of experiments that were carried out on LISA Pathfinder, the first week of operations is described here at the ‘concept’ level. Each weekly plan includes a summary, assumptions, and goals, and for each day in the plan, the setup is discussed, and the timeline specified in terms of sequential investigations. The is to provide sufficient justification to allow validation of the timeline. The daily schedule is composed of rows, each row detailing a particular investigation, and specifying the start and stop time, the high-level description of the investigation, its alpha-numeric identifier, and its duration in minutes.

Introduction First partial week of science operations, starting with a hand-over from commissioning in science mode and ending with the first station keeping day (which should occur each Saturday). The handover occurs immediately after the end of Airbus Science Run 11 (measurement of dc potentials) which means that our first POR would start the next morning at 08:00. Science Run 11 will end about 2 hours after the GS pass (Science Runs 9 and 11 require 10.5 hours). So assuming we stay in science mode we will have about 9 hours of noise measurement when our POR starts. I also assume that we will have SDM19 activated at the end of run 11 (TBC with MOC).

The plan assumes that commissioning has taken place according to the plan given in version 2.1 of S2-ESC-PL-5610 LPF Commissioning Implementation Plan.

Assumptions We assume the following is known from commissioning:

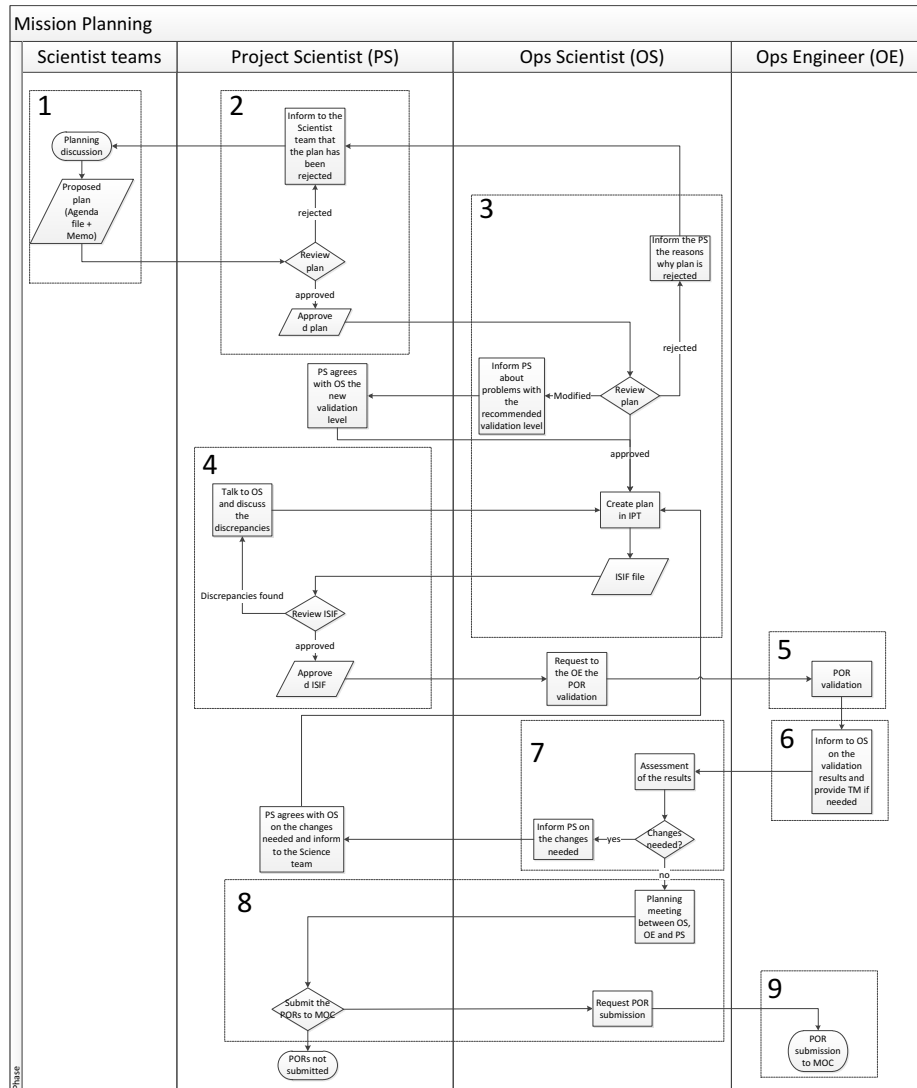


Figure 5.3.: A schematic view of the steps needed to validate an experiment from concept to execution.

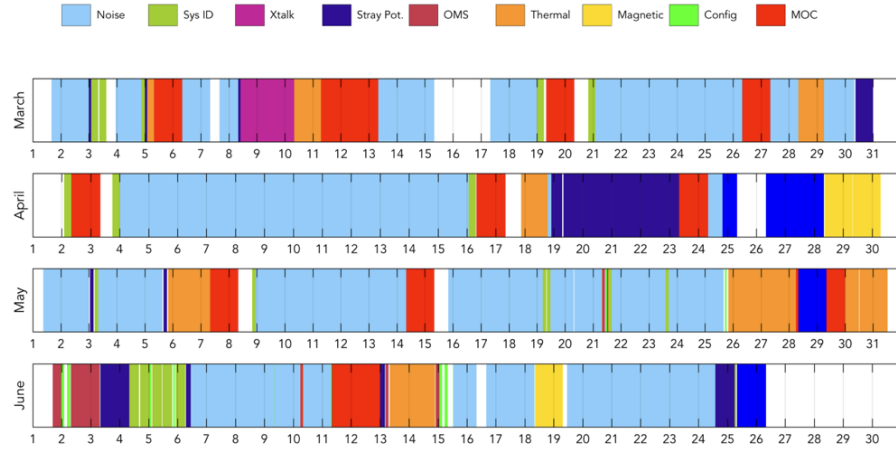


Figure 5.4.: A calendar view of the nominal operations phase showing the breakdown of the time into classes of investigation.

1. The OMS is operating nominally with a noise performance similar to that of the OSTT, i.e. a performance towards higher frequencies of around $3 \text{ pm}/\sqrt{\text{Hz}}$. The working point experiments in Run 9 have confirmed that locking on a phase of 0 gives the best noise performance with regards any amplitude or phase noise coupling.
2. The temperature around the TM housings is about 293 K with a stability around $5 \times 10^{-6} \text{ K}/\sqrt{\text{Hz}}$.
3. The sensing noise from the inertial sensor front-end electronics is around $2 \text{ nm}/\sqrt{\text{Hz}}$.
4. DFACS science mode 1.2 can easily be reached and is stable for long periods (days).
5. A nominal alignment (including polarity) between the OMS and the GRS has been established and is part of the baseline configuration for science mode. This includes angular offsets to minimise cross-talk/piston effects, as calculated from Science Run 5.
6. The measured charge rate is such that we can aim for discharging once per week during station keeping.
7. The fast discharge system works and requires two hours per test mass to discharge to an acceptable level. It is assumed this will be done during the MOC window each week.
8. The differential test mass acceleration has been measured to be stable on time-scales of hours at a level of around $10 \text{ fm s}^{-2}/\sqrt{\text{Hz}}$ around 3 mHz.
9. The total stiffness of TM2 along x has been measured to be around the nominal value of $-2 \times 10^{-6} \text{ s}^{-2}$.
10. The gain of the x-axis suspension actuation has been calibrated to be unity at the percent level.
11. All cross-talks are much smaller than the ICD values. No major ‘broken’ element of the system has been identified.



12. The pressure within the TM housings has been shown to be lower than 10^{-5} Pa.
13. The stray EH potentials have been measured and a dx of less than 100 mV with an error smaller than 10 mV has been estimated, thus allowing us to compensate within about 10 mV.
14. Science data handling behaves nominally in that a typical day of data contains no significant gaps and the equipment time-stamps are usable to re-stamp the data.

Goals By the end of week one we should achieve the following:

1. Establish a baseline noise performance and stability. Catalogue the presence of lines, glitches, etc.
2. Verify the calibration accuracy of Δg (residuals during sys id).
3. Confirm low levels of angular cross-talk into Δg .
4. Confirm the charge rate over longer times.
5. Confirm the X12 common-mode rejection is at a negligible level ($< 10^{-4}$)

DOY60: 01.03.16, (08:00 – 08:00) Continue the Sci1.2 noise measurement which started after Science Run 11 ended in commissioning.

08:00 – 16:00 Empty investigation of 8 hours duration. inv00008:V001 [28800]
 16:00 – 00:00 Empty investigation of 8 hours duration. inv00008:V001 [28800]
 00:00 – 08:00 Empty investigation of 8 hours duration. inv00008:V001 [28800]

DOY61: 02.03.16, (08:00 – 08:00) Continue noise measurement. By this time we will have collected enough noise to have a decent PSD measurement (16 averages) of Δg down to about 0.2 mHz.

Charge estimates of both masses to continue monitoring and establishing rate stability.

x -axis sys id experiments with low amplitudes to allow us to confirm the stiffness measurements made in commissioning, and the calibration of the applied force along x on TM2. We also confirm here that our Δg model is complete and is not missing any transfer function component (additional poles or zeros or delays).

08:00 – 16:00 Empty investigation of 8 hours duration. inv00008:V001 [28800]
 16:00 – 00:00 Empty investigation of 8 hours duration. inv00008:V001 [28800]
 00:00 – 01:00 Charge Estimate TM1 (low amps). inv04011_003 [3600]
 01:00 – 02:00 Charge Estimate TM2 (low amps). inv04021_003 [3600]
 02:00 – 05:00 Drag-free Injections (10nm scale). inv01101:V003 [10800]
 05:00 – 08:00 Suspension Injections (10nm scale). inv01102:V003 [10800]



DOY62: 03.03.16, (08:00 – 08:00) Explore cross-talk levels through guidance injections in the different degrees of freedom. Here we do the angular degrees of freedom; the linear degrees of freedom come in week 2. These should be low amplitude injections, just enough to explore the dynamics around the working point, and to confirm that no significant cross-talk terms are visible.

Charge estimates of both masses to continue monitoring and establishing rate stability.

(These crosstalk experiments are placeholders since a proper design of these experiments is missing. In general, they are likely to be longer than this since low frequencies need to be injected as cross-talk is likely to play a significant role at frequencies below 1 mHz. This is especially true for the SC motions, where we already have expectations of some coupling of SC jitter at lower frequencies.)

08:00 – 12:00	Guidance eta1 (low amps).	inv01167_002	[14400]
12:00 – 16:00	Guidance eta2 (low amps).	inv01173_002	[14400]
16:00 – 20:00	Guidance phi1 (low amps).	inv01168_003	[14400]
20:00 – 00:00	Guidance phi2 (low amps).	inv01174_003	[14400]
00:00 – 05:00	Guidance Eta.	inv01161:V001	[18000]
05:00 – 06:00	Charge Estimate TM1 (low amps).	inv04011_003	[3600]
06:00 – 07:00	Charge Estimate TM2 (low amps).	inv04021_003	[3600]
07:00 – 08:00	Empty investigation of 1 hour duration.	inv00001:V001	[3600]

DOY63: 04.03.16, (08:00 – 08:00) Finish crosstalk injections.

Charge estimates of both masses to continue monitoring and establishing rate stability.

Long noise measurement before going into station keeping.

08:00 – 13:00	Guidance Phi.	inv01162:V001	[18000]
13:00 – 21:00	Empty investigation of 8 hours duration.	inv00008:V001	[28800]
21:00 – 05:00	Empty investigation of 8 hours duration.	inv00008:V001	[28800]
05:00 – 06:00	Empty investigation of 1 hour duration.	inv00001:V001	[3600]
06:00 – 07:00	Charge Estimate TM1 (low amps).	inv04011_003	[3600]
07:00 – 08:00	Charge Estimate TM2 (low amps).	inv04021_003	[3600]

5.3. Simulation campaigns, Team building and training

Preparation for LISA Pathfinder science operations necessarily included a significant amount of simulation and training. Simulations played an essential part in many aspects of the preparation:

- definition of the experiments, investigations and configurations;
- development and testing of analysis routines;
- exercising and testing the operational environment and tools;
- and training of the team and operational teams.

For different purposes, a number of simulation types were used. These are briefly described below.



5.3.1. STOC Exercises

STOC Exercises were regular meetings of the core science operations team and the STOC engineers. The aims of these events was to:

- aid in developing and testing the STOC environment and tools;
- identify S/C level commanding and procedures to allow preparation of investigations and configurations;
- and to exercise the whole data chain.

Starting early in 2009 and running all the way to the summer before launch, 44 of these events were conducted. Lasting typically 2 or 3 days, with preparation and follow-up, they represent a significant effort in development and played a crucial role in ensuring a smooth operations environment, with a well prepared set of tools and investigations, all of which were the building blocks for successful science operations. Typically 2 or 3 members of the science team were present, depending on the expertise required, and they were joined by the operations engineers at ESAC where the events were typically held.

5.3.2. STOC Simulations

With the building blocks of the mission put in place via STOC Exercises and other development, there was a need to bring that all together to test and validate the operations concept. This was done by designing ‘mock’ experiment timelines lasting from a few days to a couple of weeks. These timelines were then simulated and analysis teams were assigned shifts to do the analysis in quasi-real-time, as in the real mission operations. Through this process we all exercised the interaction of different experiments, resulting in valuable information to aid in the design of the experiment timeline during operations.

The first STOC simulation took place in June 2012 and lasted for 3 days. Its main purpose was to establish a timetable for operations and to exercise the interactions between on-line data analysis teams, and off-line teams. Figure 5.5 shows a schematic overview of the interactions and activities that were exercised during the first STOC Simulation.

The second STOC simulation took place in November 2012, and lasted 4 days, with a focus on exploring the interaction of a particular set of experiments to check for timing conflicts, and analysis problems.

A further 4 STOC simulations took place, the last one in November 2015, which lasted 3 days and focused on interactions between MOC and STOC.

The longest, STOC Simulation 5, lasted nearly 2 weeks and tested the full operations scenario. It took place in September 2015, and set the scene for the science operations just before launch.

Each simulation represented a significant investment of effort, both from the ESA operations team, and the science operations and data analysis team. In each case, a few weeks of preparation was needed to

- define the scientific content,
- prepare the experiment descriptions,

Activities

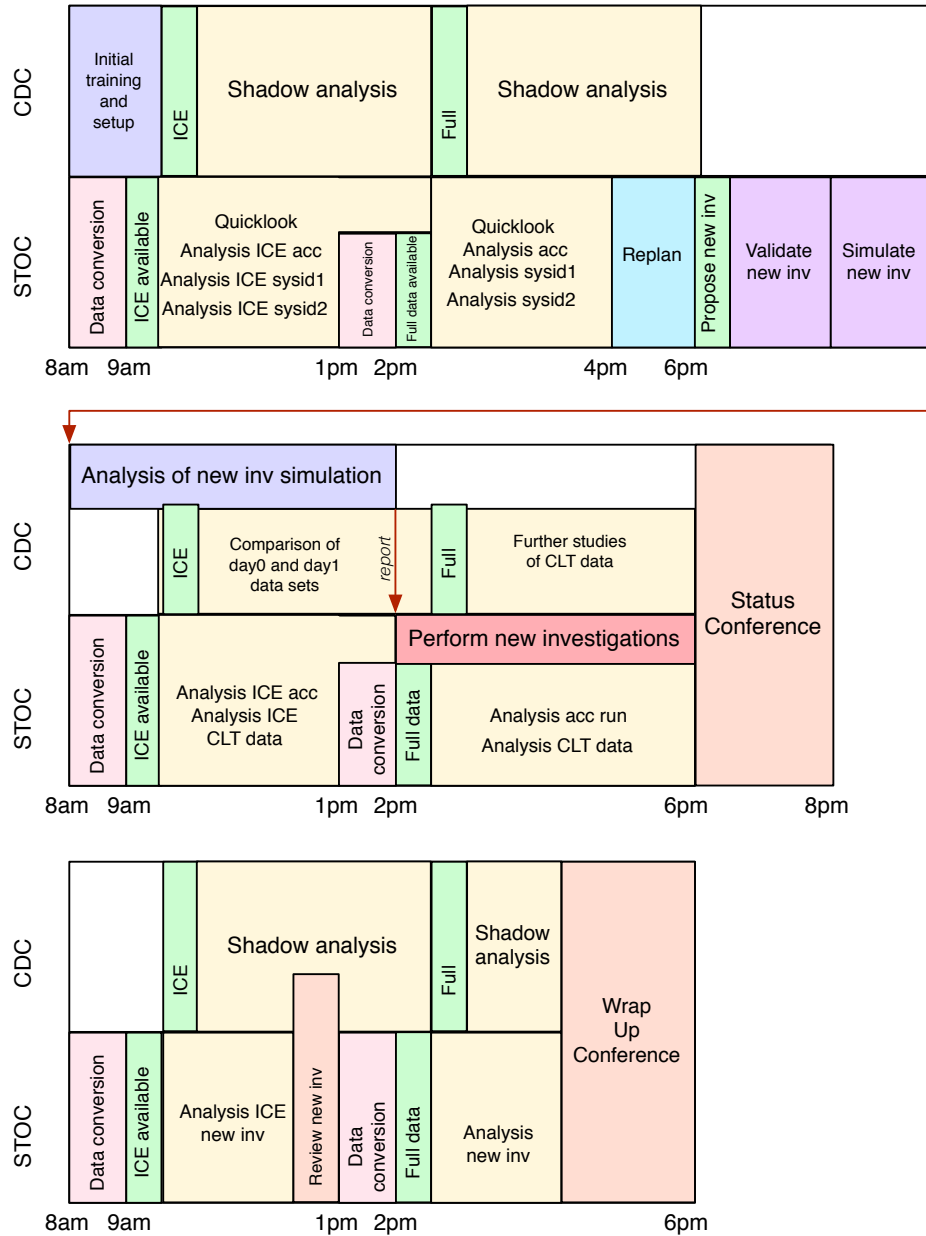


Figure 5.5.: A schematic of the interactions and activities testing in STOC Simulation 1.



- implement the needed investigations and configurations,
- develop and test analysis tools and pipelines,
- define a shift schedule,
- prepare and train the team
- validate the operational tools.

Achieving this required a series of telecons and meetings, test readiness reviews, change control boards for software, and training sessions.

Each simulation was also followed by off-line analysis, follow up telecons, and wrap-up and results meetings.

5.3.3. LTPDA and data analysis training

A critical aspect of the preparation for science operations included comprehensive training of the team. As well as needing to be fluent in the physics and experiments of the mission, the team members needed to become experts in the use of LTPDA and the data analysis pipeline. Although data analysis shifts were sometimes targetted to experts in a particular experiment, this was not always the case, and not always appropriate. A number of experiments were repeated regularly, and this required that all team members be able to understand and analyse such experiments.

Training of the team was conducted in various ways:

- Dedicated LTPDA training sessions. The LTPDA development team developed two detailed tutorials which were exercised in hands-on workshops, and made available for offline training of new team members.
- Focussed data analysis training sessions were organised to train team members in the use of the data analysis pipelines, and to familiarise them with the data involved and the expected results of a whole wealth of different experiments.

Part III.

In-orbit operations

6. Science operations

6.1. Introduction

The following sections describe experiments and tasks that were performed by members of the AEI LPF team, alongside the LPF collaboration, during the mission.

6.2. $\Delta g(t)$ calibration

It was shown in [1] that the LPF mission exceeded all expectations by measuring differential acceleration between the two test-masses at the level of $5.2 \pm 0.1 \text{ fm s}^{-2}/\sqrt{\text{Hz}}$ for frequencies of 0.7 to 20 mHz. In order to make this measurement of the differential acceleration, it is necessary to estimate the key dynamical parameters of the system. For that reason, several system identification experiments were performed throughout the duration of the mission (see figure 6.1).

These experiments are the so-called x-axis system calibration investigations, and they refer to the dynamics along the sensitive longitudinal interferometer measurement. In this section we discuss the design of aforementioned experiments, the strategies followed for their analysis, and the further calibration steps for the $\Delta g(t)$ quantity.

The starting point is the dynamics of the three-body system of LPF, which can be written

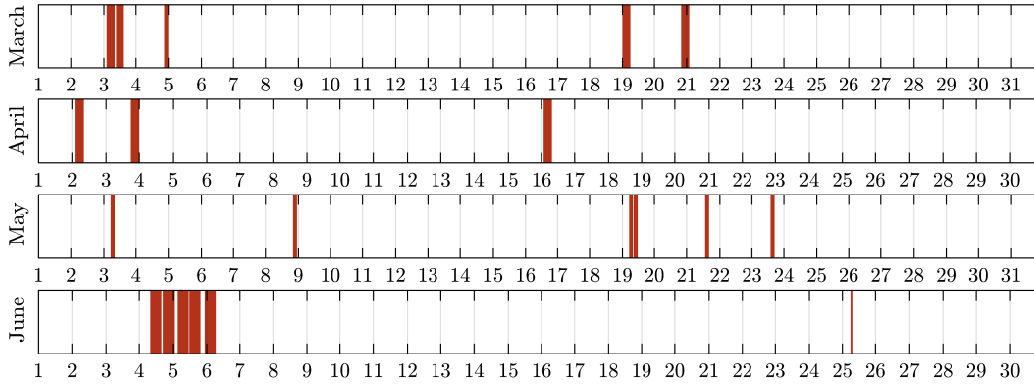


Figure 6.1.: The system identification experiments during nominal mission operations. This type of experiment needed to be performed in regular intervals, in order to estimate the dynamical parameters of the system, or to assess the stationarity of the system.

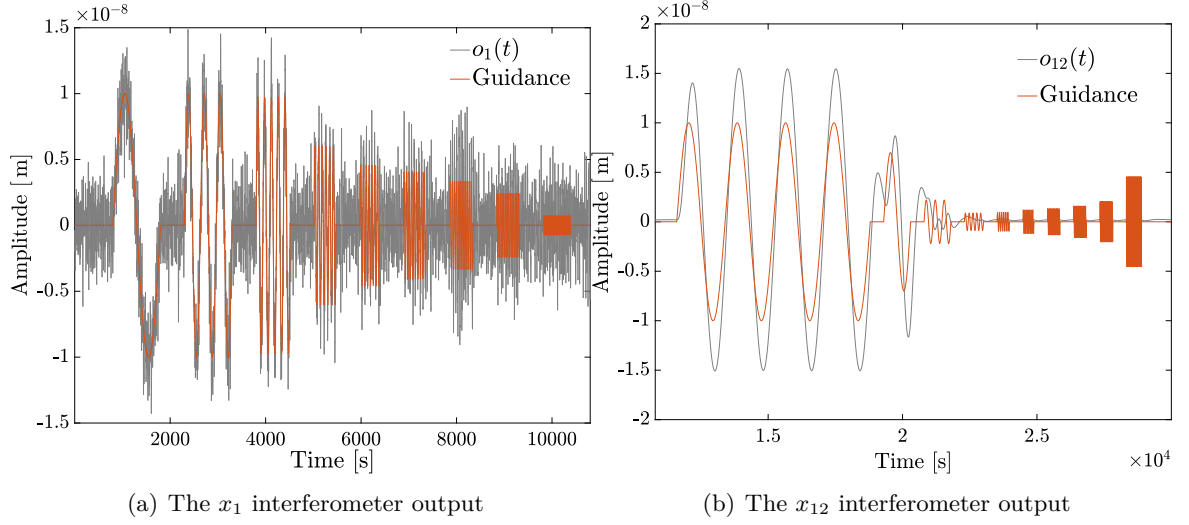


Figure 6.2.: Batteries of injections during the system identification experiment. *Left*: Injection sinusoidal signals (red) into the drag-free loop. The response of the system as recorded by the o_1 interferometer is shown in grey. *Right*: The same philosophy applies to the suspension loop as well. The measurement of the o_{12} interferometer is again shown in grey. Source: [18].

as:

$$\Delta g(t) \equiv \ddot{o}_{12}(t) - \lambda_2 \frac{f_{x2}}{M_2}(t - \tau) + \omega_2^2 o_{12}(t) + \Delta \omega^2 o_1(t) + \Delta g_{X\text{-talk}} \quad (6.1)$$

where the different elements of eq. (6.1) are

$$\begin{aligned} o_i & \text{--The interferometer outputs.} \\ \lambda_2 & \text{--The gain coefficient of the applied force } f_{x2} \text{ on TM2.} \\ M_2 & \text{--The mass of TM2.} \\ \tau & \text{--A delay coefficient.} \\ \omega_2^2 & \text{--The stiffness of TM2} \\ \Delta \omega^2 & \text{--The differential stiffness.} \\ \Delta g_{X\text{-talk}} & \text{--Various cross-talk terms.} \end{aligned} \quad (6.2)$$

The idea behind the system identification experiments is to excite the system by injecting known sinusoidal signals, simulating fake interferometer readouts, and studying the reaction of the system. For the x-axis case we injected a frequency sweep type of signal, which in essence is inducing TM motion with maximum amplitude of 10 nm (see figure 6.2). The same principles apply to the cross-talk experiments as well (see section 6.3), where we inject in different degrees of freedom on both TMs and the spacecraft.

During operations the analysis had to be performed online and almost in real time. Therefore whenever possible we linearised the model of the dynamics to reduce the complexity.



An equivalent linearised version of eq. (6.1) is the following:

$$\Delta g \equiv \ddot{o}_{12}(t) - \lambda_2 f_{x2}(t) + C_1 \dot{f}_{x2}(t) + \omega_2^2 o_{12}(t) + \delta \omega^2 o_1(t) + \Delta g_{\text{X-talk}}, \quad (6.3)$$

where the C_1 coefficient is a linearised delay coefficient. The dynamics of eq. (6.3) allow us to use an iterative re-weighted least square fitting scheme [19], where the problem reduces to solving a set of linear equations at each iteration of the algorithm. This procedure, at the n -th iteration, can be explained as a form of a χ^2 :

$$\chi_n^2 = N_s \sum_{j \in Q} \frac{|\tilde{r}_j(\vec{\theta}_n)|}{|\tilde{r}_j(\vec{\theta}_{n-1})|}. \quad (6.4)$$

where \tilde{r} is the residuals in frequency domain, j is the given frequency bin $\in [1, Q]$, and N_s is the number of averages for the spectrum calculations. For more demanding calculations, where either the model is not linear, or for analysing the complete set of experiments in a single fit scheme, we used sampling methods, like Markov Chain Monte Carlo [20]. We start by assuming a likelihood function of the form of

$$\pi(y|\vec{\theta}) = C \times e^{-\frac{1}{2}(y - h(\vec{\theta})|y - h(\vec{\theta}))} = C \times e^{-\chi^2/2}. \quad (6.5)$$

Here, we have assumed that the measured data set is $y = h(\vec{\theta}) + n$, with $h(\vec{\theta})$ being the *template* depending on the parameters $\vec{\theta}$ and n the noise. The $(\cdot|\cdot)$ denotes the noise weighted inner product

$$(a|b) = 2 \int_0^\infty df \left[\tilde{a}^*(f) \tilde{b}(f) + \tilde{a}(f) \tilde{b}^*(f) \right] / \tilde{S}_n(f), \quad (6.6)$$

between two real time series a and b . The tilde ($\tilde{\cdot}$) denotes the operations in frequency domain, and the asterisk ($*$) the complex conjugation. S_n is the one-sided Power Spectral Density (PSD) of the noise. The PSD of the noise is assumed known in eq. (6.5), but this might not be the case during the measurements (non-stationarity, outliers). For that reason we also used different formulations (after some assumptions), like in [21] or [19]. For the cases where there were no spurious events in the data, the fitting of the system identification experiments were proven to be of good quality, since the residuals were calculated to be at the same level as the noise.

6.2.1. Further corrections on the $\Delta g(t)$ measurements

In [18], it was shown that at lower frequencies, the inertial forces associated to space-craft slow rotation contributed to the differential acceleration $\Delta g(t)$. The SC rotation introduced apparent forces on the TMs, that the suspension control tries to compensate in order to keep the TMs at their nominal distance. Therefore, it is necessary to subtract this effect from the acceleration noise in eq. (6.1). The centrifugal contribution to the differential acceleration between the two TMs is then given by

$$\Delta g_\Omega = \ddot{x}_2 - \ddot{x}_1 = (\omega_\phi^2 + \omega_\eta^2)(x_2 + x_1), \quad (6.7)$$

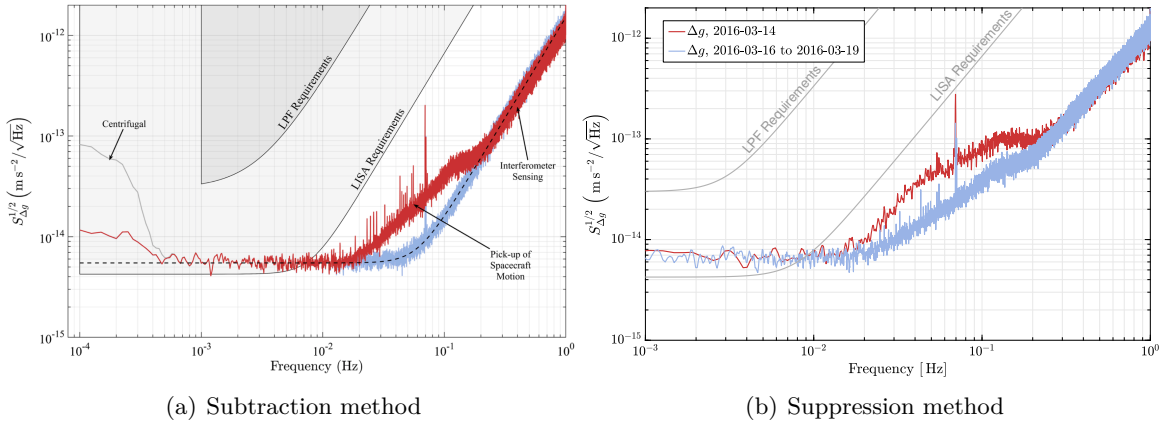


Figure 6.3.: (a): Result taken from [1], showing that the bulge at 200-20 mHz can be subtracted. (b) In this figure, no subtraction was performed. Instead the reduction was achieved by a realignment of the test masses prior to the second noise run.¹

where ω_ϕ and ω_η are the SC angular velocities around z and y, respectively. The ω_ϕ and ω_η terms appearing in the Δg_Ω equation are calculated from data retrieved by the Autonomous Star Tracker signal in the form of quaternions, together with the mean applied torques on the TMs.

In addition to the inertial forces contribution we subtract cross-coupling originating from the space-craft high frequency jitter, leaking into the differential acceleration measurement (in the frequency band between 200 mHz - 20 mHz). In order to measure this contribution we performed a fit to a model, which is in essence a linear combination of measurements from the gravitational reference sensor. Following this strategy we were able to subtract this cross-coupling effect, but the model does not provide any real physical information about the actual cross-talk mechanisms responsible for this acceleration noise. More information can be found in [18] and [22], or in section 6.3.

6.3. Sensing Cross-Coupling

This section discusses the cross-coupling of angular and lateral motion into the main interferometer readout signal Δg , as mentioned in [1] and discussed in [22]. We restate results published in these two documents and describe the various experiments performed to characterize and mitigate the cross coupling. For convenience, some paragraphs have been directly copied from [22].

6.3.1. The Cross Talk Problematic

The effect of sensing cross-talk is directly visible in fig. 6.3(a) which was taken from the primary LPF publication [1]. In this figure, the sensing cross-talk is the primary cause of the bulge in 200 mHz - 20 mHz frequency band. The task now is to characterize the cross



coupling in order to suppress it. That means, we now try to find a model for $\Delta g_{\text{X-talk}}$ that can be used to subtract the coupling from Δg as defined via the Sys-ID section:

$$\Delta g \equiv \ddot{o}_{12}(t) - \lambda_2 f_{x2}(t) + C_1 \dot{f}_{x2}(t) + \omega_2^2 o_{12}(t) + \delta \omega^2 o_1(t) + \Delta g_{\text{X-talk}}. \quad (6.1)$$

In an ideal system, o_{12} should only sense differential longitudinal displacement of the two test masses. In reality however, also lateral and vertical displacements as well as rotations of either a test mass or the spacecraft couple into o_{12} . This is a natural but unwanted cross-talk which we investigated with several experiments during LISA Pathfinder operations in order to find a model for $\Delta g_{\text{X-talk}}$ that fully describes the coupling and allows a suppression of this unwanted effect by a realignment of the test masses. In principle, there are two optional ways on how to define $\Delta g_{\text{X-talk}}$ and process with the sensing cross-talk. In [1] it was shown, that it is possible to subtract the cross-coupling noise directly resulting in the blue curve in fig. 6.3(a). This was achieved by fitting a comparably simple model to the data, with excellent results, as shown in fig. 6.3(a). However, this technique has several disadvantages: First of all, the model provides no interpretation what the coefficients physically mean, and therefore no explanation how the cross-coupling could be suppressed. Secondly, it was proven that the model assumed is not the only model allowing a fit and subtraction with low residuals. Instead, there is a set of models, performing comparably well. Finally, the fit coefficients vary over the mission duration for more than three sigma, and this variation cannot be explained with the model adopted.

For these reasons, there is a still ongoing effort, to build a physical model, which can describe the cross-coupling over the entire mission duration with a constant set of parameters, and can be used without adaptation for any set of data to subtract the bulge. Preliminary results have been used already in the early mission phase, to realign the test masses and thereby directly reduce the amount of cross coupling. In fact, fig. 6.3(a) shows a noise run performed in April 2016 (2016-04-08 to 2016-04-14), which was after a first realignment of the test masses had already reduced the amount of cross-talk. This will be further discussed in the next section.

6.3.2. A Simple Time Dependent Cross Talk Model

One possible simple model that can be used for a subtraction like shown in Fig 6.3(a) is:

$$\Delta g_{\text{X-talk}} = C_1 \ddot{\phi}[t] + C_2 \ddot{\eta}[t] + C_3 \ddot{y}[t] + C_4 \ddot{z}[t] + C_5 \bar{y}[t] + C_6 \bar{z}[t] + \delta_{\text{ifo}} \ddot{x}_1[t]. \quad (6.8)$$

Each term in this equation defines a cross-coupling of spacecraft motion to the differential acceleration measurement:

- All but the last summand are cross-coupling terms, because ϕ, η, y, z are orthogonal coordinates to the differential readout along x . See fig. 2.3 for a definition of the coordinate system.
- The annotation \bar{k} with $k \in \{\phi, \eta, y, z\}$, defines a mean motion of both test masses along k , which is a description of the spacecraft motion along $-k$.

¹Please note: the slight difference in curvature around 3 mHz in the LPF requirements in the two figures results from different notations: while in fig. 6.3(a) correlated noise sources were assumed, we chose in fig. 6.3(b) the notation for uncorrelated noise sources.

- The last summand, describes a residual coupling of spacecraft motion along x entering the differential readout. As the term ‘differential readout’ indicates, Δg is defined as $\Delta g = \ddot{x}_2 - \ddot{x}_1$ (neglecting here corrections such as for applied or inertial forces). It should therefore be insensitive to any common-mode motion, where $\ddot{x}_2 = \ddot{x}_1$. Since spacecraft motion effectively shows as common test mass motion, Δg should not sense spacecraft motion. However, there is a residual leakage, because the interferometer readout response is not identical to TM1 motion as to TM2 motion, such that $\Delta g = k_2 \ddot{x}_2 - k_1 \ddot{x}_1$ with $k_2 \approx k_1 \approx 1$. The small difference between k_1 and k_2 causes the residual cross-coupling.

6.3.3. The Time Independent Cross Talk Model

This model is currently still work in progress and can therefore not be shown yet. To allow however an understanding of how such a model looks like, we can define it in a very general way as:

$$\Delta g_{\text{X-talk}} = \frac{d^2}{dt^2} f(\phi, \phi_0, \eta, \eta_0, y, y_0, z, z_0, \dots) . \quad (6.9)$$

In such a model, the fit coefficients C_i of the time dependent model are replaced by directly physically interpretable parameters like for instance calibration constants ϕ_0, η_0, y_0, z_0 of the measured angles ϕ, η , and measured displacements y, z . Due to the physical motivation of the model, the time independent model becomes non-linear, and contains fit coefficients multiple times and in factors with other coefficients which makes the fitting of the data specifically complicated.

6.3.4. The Engineering Days Experiments

In the third week of operations a set of experiments was performed which was dedicated to reduce the amount of sensing cross talk by realignment of the test masses. Unlike all other experiments, this was performed with life data, which shaped the name ‘Engineering Days Experiments’. In order to realign both test masses in ϕ , on the first day (on DOY075, i.e. March 15 2016) a number of injections in the ‘y1-y2-plane’ was performed, that means in the plane span by both test masses moving along their y-axis (see fig. 2.3 for a definition of the coordinate system). As an example, fig. 6.4 shows a 10 mHz common mode test mass motion of 1 μm amplitude injected at DOY075 starting from 7:50 UTC and the resulting cross coupling into the differential readout o_{12} . The lateral motion of the second test mass denoted by y_2 is hidden in this figure behind the lateral motion of TM1 (y_1), which shows how well the test masses moved in common mode. The differential readout o_{12} shows a nanometer drift behavior which is of no significance here. However, the oscillation visible in o_{12} clearly visualizes the unwanted cross coupling of motion along y_1 and y_2 .

Likewise, fig. 6.5 shows a 10 mHz differential test mass motion with 0.5 μm amplitude injected at DOY075 starting from about 9:03. At this time there was only little drift in o_{12} which makes the cross coupling in this figure more visible.

Both figures show injections for nominal test mass orientations. During DOY075, both test masses were slewed to several angular offsets in $\phi_{1,2}$ which were then tested for cross coupling with common mode and differential mode injections like those shown in fig. 6.4 and fig. 6.5.

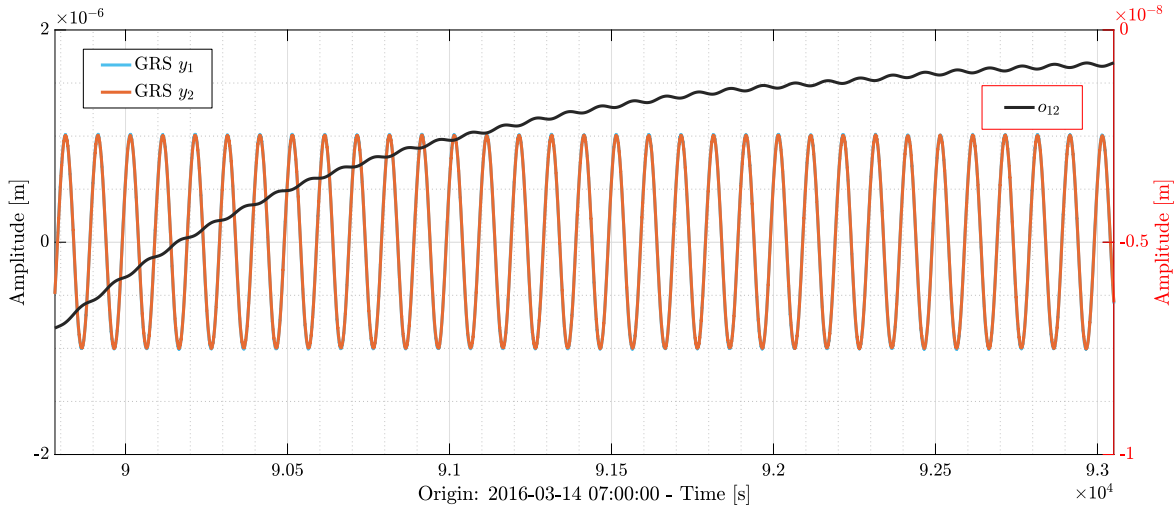


Figure 6.4.: Injection of common mode motion of both test masses in y-direction. The raw differential readout o_{12} shown in black comprises an oscillation caused by cross coupling of the injected lateral motion.

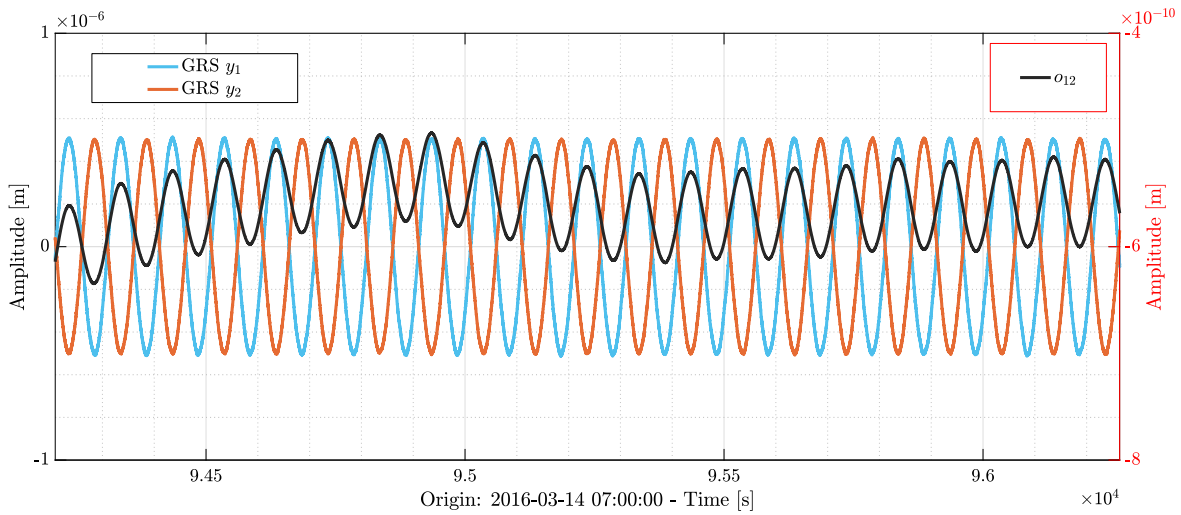


Figure 6.5.: Injection of a differential motion of both test masses in y-direction. The raw differential readout o_{12} shown in black comprises a strong oscillation caused by cross coupling of the injected motion.

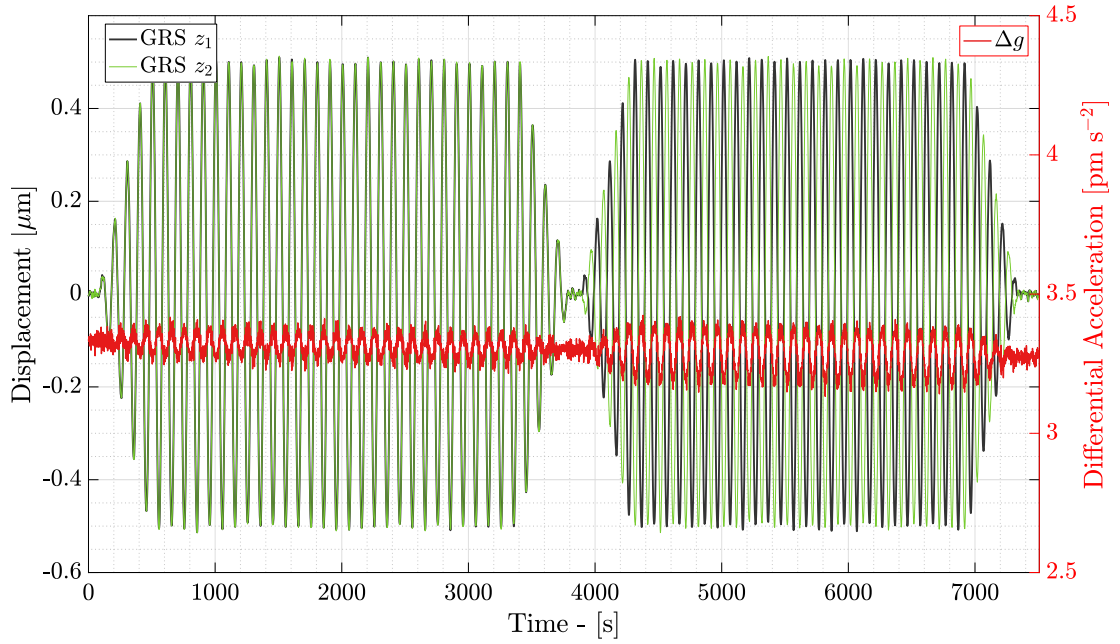


Figure 6.6.: Example of $z_{1,2}$ injections performed during the engineering days cross-talk experiment performed on 2016-March-16. The labels ‘GRS $z_{1,2}$ ’ indicate, that the shown vertical test mass displacement (z_1, z_2) is taken from the Gravitational Reference Sensor readout. This figure has been previously published in [22].

For the realignment of the test masses in angle η , a comparable set of injections at different offsets was performed on the following day (DOY076, i.e. March 16 2016) in the ‘z1-z2-plane’, so the plane spun by test mass motion along their z-axis. Fig. 6.6 shows common mode and differential mode injections and the resulting cross coupling - here directly to Δg .

6.3.5. Life Analysis of the Engineering Days Experiments

On the first day of the Engineering Days, we analyzed the incoming data life with a very simple version of a time independent (physical) model. After the first set of experiments, we thereby found a first result on what angular offsets in ϕ should be commanded to the test masses in order to reduce the coupling. It quickly proved, that the used model was insufficient, because the coupling did not reduce as expected. During the following set of experiments however, a minimum point of the coupling could be located, the test masses were realigned and the coupling was reduced as expected.

On the following day, the same procedure was performed in the z1-z2-plane using again the simple model which had already shown inconsistencies. Nevertheless, it was possible to determine alignment offsets in $\eta_{1,2}$, which were then applied and the coupling was reduced. As an outcome of this experiment, the found offsets were placed permanently into DFACS, such that the alignment of the test masses stayed on the found offsets.



6.3.6. Further Analysis of the Engineering Days

After the Engineering days, we continued to develop the system model explaining all relevant coupling mechanisms. The model was iterated multiple times switching from linear models to non-linear models, taking into account more and more effects. At the end of mission operations we did have very promising results, which seemed to explain all present data sets. Based on those analyses, the test masses were slewed again on DOY176 (Jun 24, 2016) slightly changing $\phi_{1,2}$ and $\eta_{1,2}$ again, but now applying also offsets in $y_{1,2}$ and $z_{1,2}$. As a result, these new set points were placed in DFACS and the cross coupling was further mitigated.

6.3.7. Need for another Cross Talk Experiment

After the second TM realignment, another noise run was performed and analysed together with the noise runs prior to the realignment. Unfortunately, the model failed to explain the new noise run, showing that it still was not sufficiently general. The cause of this was the lateral realignment of test masses applied with the new set points. All data that was present before was for rotated but not shifted test masses, and this could fully be described by the present model. The offsets in $y_{1,2}$ and $z_{1,2}$ however, were not sufficiently described by this model. Therefore, a new experiment was planned for missions extension to fully test the parameter space. Due to time constraints, this was performed in two steps: first a short cross talk experiment which lasted 5 hours and was run on DOY020 (Jan 20, 2017) followed by a long cross talk experiment which lasted 48 hours and was run on DOY036 to DOY037 (Feb 05 to 06, 2017).

6.4. Drift mode investigation

6.4.1. The Goal and Design of the Experiment

As described in full detail in [23], after much efforts both in the laboratories and at system engineering level, a current best noise estimate before launch was developed. It suggested a noise level well below the requirements. Moreover, it lead to the expectation that the direct forces on the test mass would not be limiting towards the lower end of the LPF measurement band and below. Instead, the expected contribution from the electrostatic actuation noise would be dominating. This is undesired for two reasons: First, the measurement of the residual acceleration due to the direct forces on the test mass is what should be measured with LPF and not the noise of a subsystem that can be fairly well characterised with a torsium pendulum facility on Earth [24]. The second reason is even more significant: in LISA, the actuation scheme will be different and there will not be actuation along the sensitive measurement axis. In other words, the strong contribution from actuation is not representative for LISA and thus, we would like to avoid this also in the technology demonstrator mission. Unfortunately, this is not straightforward to implement. For simplicity, let us consider the situation along the x-axis only. One TM is not controlled along this axis, our free-falling test mass, generally called TM1. The satellite follows the motion of this test mass along x, as implemented in the drag-free control loop. Now, imagine the reference TM, the so-called TM2, would move in the opposite direction along x. Then, the satellite could not follow both of them at the same time and a drag-free control would not be possible. To prevent this

from happening, the reference test mass is constantly actuated along the x direction. The necessary force from electrostatic actuation is calculated by the so-called suspension loop. This is the main reason for the acutation noise. In addition, the actuation along x and ϕ is using the same electrodes. That is why the actuation along ϕ , which is constantly required, also produces noise along x .

6.4.2. The working principle

Intuitively, the first idea is to just switch off the actuation. However, due to satellite integration tolerances, it was expected that the masses of the different elements on the satellite could not be balanced perfectly such that a remaining local gravitational field of 0.65 nm s^{-2} [25]. would move the test mass out of the recommended position range of $5 \mu\text{m}$ [26] before a measurement at 0.1 mHz could be made. The drift mode or free-flight experiment solves this problem. The key idea is to replace the constant control of the TM2 along x by intermittent control only. This means, TM2 is subject to a short force impulse, a so-called kick, and then left free-falling along its x direction for a certain period, the so-called drift. The experiment was designed to have approximately 349 s of drift and 1 s of kick [27]. In the original design, the electrostatic actuation system goes to the so-called wide range mode (WR) during the kicks and is in the high-resolution mode (HR) during the drift phases [28]. Following the requirements [29], in the WR, the maximum force that can be applied is higher ($9.38 \times 10^{-7} \text{ N}$ compared to 2.21 nN in HR) but the acutation is also noisier by a factor of 15 compared to the HR mode. Originally, in the HR mode, the so-called nominal actuation authority is set. A second version of the drift mode experiment, in which the ϕ degrees of freedom of both TMs together with the x -direction of the reference TM are controlled, was also designed. Further details on this mode can be found in [30]. However, it was not applied during the nominal LTP operations phase.

6.4.3. The drift mode during the nominal operations phase

The nominal design of the drift mode experiment was executed on DOY 161, that is from 08.30 UTC on 2016-06-09 until 2016-06-10 6.34 UTC. Figure 6.7 shows an example data stretch of free-fall data. The fact alone that this intermittent control mode was in stable operation during the whole experiment is remarkable. Preliminary results, to be published soon, indicate that the noise level at this time is significantly lower than during a standard noise measurement with nominal acutation authority. This is in good agreement with the actuation noise models [25]. Due to exceptional balancing of all satellite components, the DC part of the local gravitational field on LPF is roughly around and below 50 pm s^{-2} [1]. One of the main contributions is the laser radiation pressure, followed by the gas level in the cold-gas thruster tanks. This allows us to reduce the actuation authority already in the standard noise measurement. As expected, a smaller acutation authority also leads to smaller actuation noise. Indeed, we could reduce the actuation level to such extend that it seems to be no longer the dominating noise contribution at the lower part of the measurement band. This very low actuation level is called URLA and is characterised by the actuation authority of 50 pN along x_2 and 1 pN m along ϕ_2 , respectively. The remainder of the acutation noise in the URLA configuration seems to arise to a large fraction from the ϕ control. The reduction of the actuation authority was also applied to the drift mode experiment during the drift

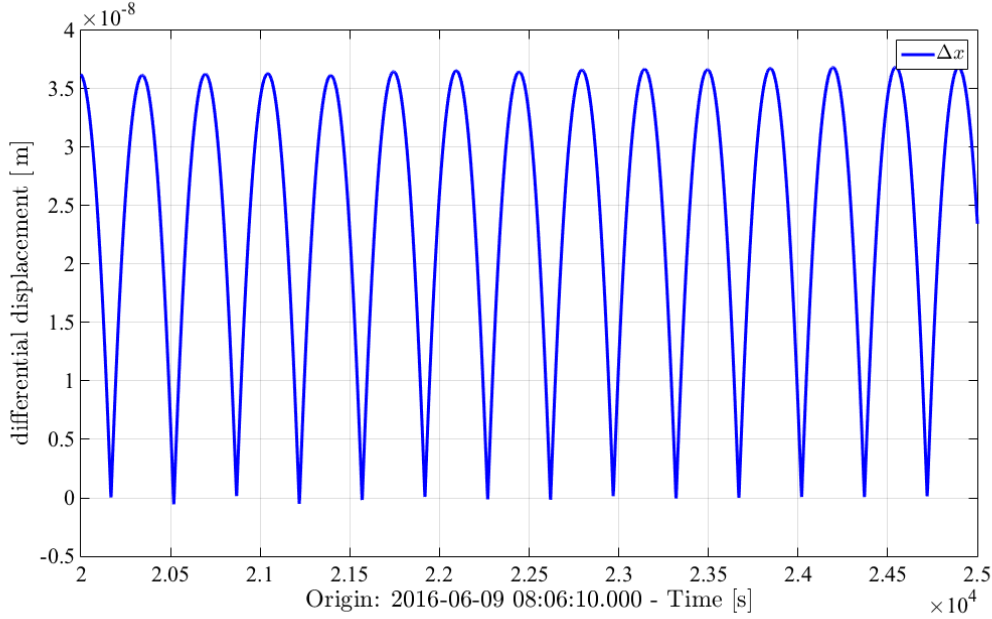


Figure 6.7.: An example data segment of drift mode or free-fall data from the first run of the experiment to illustrate the typical quasi-parabolas. The data has been preprocessed with the respective standard procedure and downsampled to 1 Hz.

phases. As the applied forces on the TMs along x are zero in this experiment per definition, this applies to the other degrees of freedom, especially the rotation along ϕ . Thus, it is expected that the noise levels in the standard science run and in the re-configured drift mode experiment are compatible. However, the drift-mode or free-flight experiment still provides valuable insight into the actuation noise because it would allow us detect actuation noise effects that are independent of the actuation authority. If no such effects are found, the experiment provides a valuable confirmation of the main science measurement. In the nominal operations phase, one run of this experiment with the URLA configuration during the flights has been performed from 2016-06-10 7.32 UTC until 2016-06-11 7.25 UTC. In between DRS operations and during the mission extension, this experiment has been repeated and significantly improved.

6.4.4. Data Analysis

Data analysis for the drift mode experiment is more demanding than for many other LPF experiments. It consists of three main steps: first the residual differential acceleration Δg has to be calculated. Second, the spectrum has to be estimated despite the presence of periodic data gaps. The third and last step is to estimate the bias introduced by the method used to cope with the gaps and to correct for it.

To estimate Δg for the drift mode or free-fall experiment, one has to follow the same principles of Δg calibration as for a standard noise measurement, as outlined in Section



6.2. However, there are some differences. In the drift mode experiment, we also have to estimate the DC differential acceleration and its linear change with time. Moreover, we also need the differential stiffness ω_{12} which can often be neglected in other experiments. On the other hand, the pick-up of satellite motion by the OMS is of lesser importance for this experiment because we are mainly interested in the low frequency behaviour. And by design of the experiment, the gain and delay of the actuation of TM 2 along x is irrelevant. We have developed and tested three different options to fit the free-flights, the details of which are to be published elsewhere.

After these parameters have been estimated and the residuals have been formed, the spectrum of the remaining fluctuations of the residual acceleration has to be estimated. However, the data during the kicks is significantly more noisy, especially if the electrostatics are in WR mode, than during the quiet drift periods and therefore has to be ignored when trying to estimate the spectrum of the small residual acceleration. Thus, we can speak of data with periodic gaps. The main challenge with the spectral estimation is that with a drift duration of 349 s, the interesting frequency range for electrostatic actuation (0.1 mHz-1 mHz) is not easily accessible. In the LPF collaboration, three main approaches to solve this problem have been developed. These are the so-called Blackman-Harris method developed by a team of University of Trento and tested on the local torsion pendulum [31] [32], the constrained Gaussian gap-patching approach, whose development was led by J.I. Thorpe [27] and the windowing approach, which will be the focus for this document.

The key idea of the windowing approach is to construct a window that smoothly goes to zero during each kick which is multiplied to the time-series of Δg prior to spectral estimation. This is illustrated in Figure 6.8. This approach was developed by A. Grynagier, who found a Hahn window to be optimal for this case [33]. However, let us note that due to the excellent performance of the OMS, the amount of high-frequency noise that can leak into the estimate of the low frequency behaviour is reduced. This is an advantage in general but especially for approaches using a window with less suppression of spektral leakage.

As a third step the bias of the amplitude spectral density estimated using the aforementioned window has to be assessed. It can be easily seen that there is a bias and that it is necessary to correct for it if one applies the windowing analysis code to a standard noise measurement and compares the result to the result obtained with the standard amplitude spectral density estimation. Such a bias also occurs when using the Blackman-Harris method. For both methods, we can only estimate the bias by assuming the shape of the true underlying spectrum is known. Details of this procedure, as well as a comparison of the results obtained with the different methods, will be reported in a future publication.

6.5. OMS vs GRS calibration

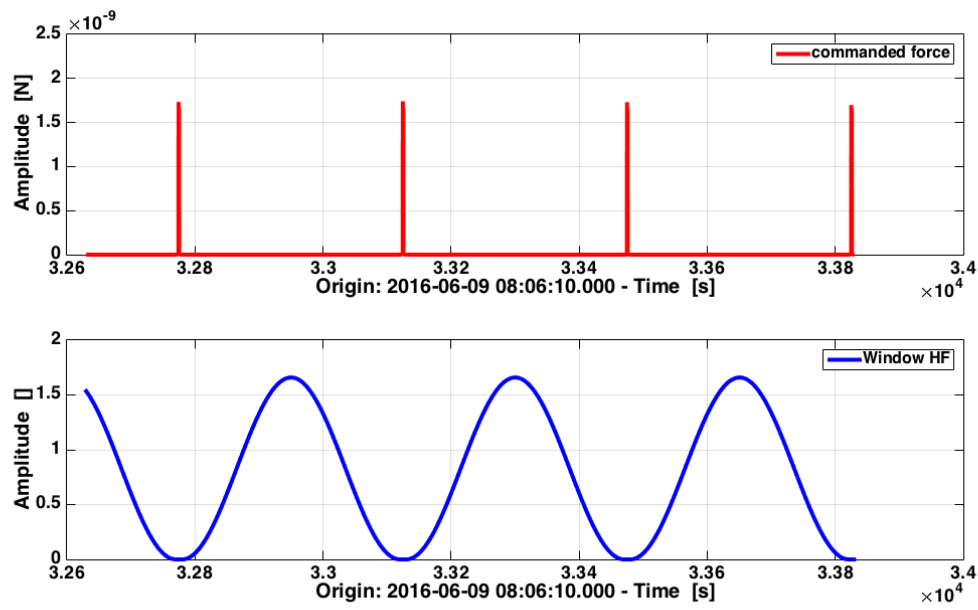


Figure 6.8.: An example data segment of the first free-fall run showing that the window goes to zero during the kick. The upper plot shows the commanded force impulses and the lower plot shows the window function that smoothly goes to zero during each kick.

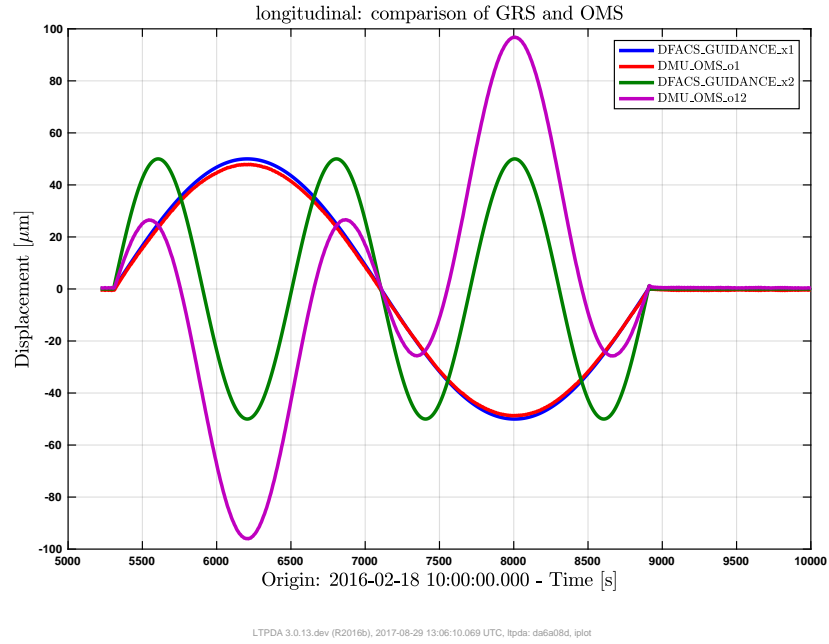


Figure 6.9.: The time series of OMS measurement of o1 (red) and o12 (purple), and the guidance injection into DFACS on the x axis of TM1 (blue) and TM2 (green). The motion measured in o12 is the result of the simultaneous movement of TM1 and TM2, both test masses move in the same x direction initially.

The test mass motion and position is measured with two readout schemes, for one we have the Gravitational Reference System, and the Interferometric System.

Test mass motion measured by these two should agree in direction and amplitude, during the commissioning of the OMS a few experiments were performed to test these systems against each other. To this end sine waves were injected into the x1, x2, phi1 and eta1 on DOY049, and in phi2 and eta2 on DOY050. In the following subsections the results of these experiments will be discussed.

6.5.1. Longitudinal calibration

As a first experiment two sine waves were injected on the longitudinal axis, one on TM1 with one cycle per hour, and one on TM2 with three cycles, both with an amplitude of $50 \mu\text{m}$.

The DFACS is set to NOM2, here the test mass control loop uses the GRS measurement as reference, and the GRS signal is also used as reference for injections. Here we compare the guidance injection to the optical measurement. In the OMS measurement of o1 we can see test mass motion of $48 \mu\text{m}$, which is $2 \mu\text{m}$ less than injected.

From this we arrive at a scaling factor of 0.96.

Before and after this injection the test mass held at its nominal zero position, here we see a difference of $\sim 0.5 \mu\text{m}$, an offset between the two systems is expected and can be corrected.

The o12 signal measures the differential signal between TM1 and TM2, the resulting

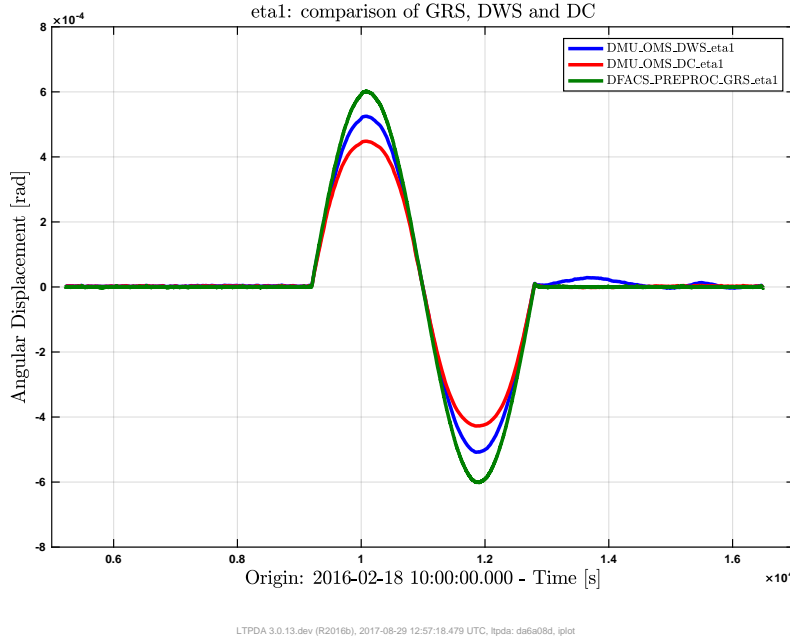


Figure 6.10.: The time series of the injection in eta1, performed on DOY049. Plotted is the injected signal (green), and the measured value of DWS (blue) and DC (red).

signal on o12 is therefore the combination of the injections on TM1 and TM2. From the combination of the two signals the first maximum should have an amplitude of $27.6 \mu\text{m}$, but only $26.5 \mu\text{m}$ is observed. We arrive at a scaling factor of 0.96 as well, the offset of the zero position between the two signals is at $\sim 0.43 \mu\text{m}$.

6.5.2. Angular calibration

The test mass angular orientation is read out in three ways, we have the signal of the GRS which is measured with capacitive sensing, the DC measurement where the test mass orientation is calculated from the spot position of the measurement beam on the QPDs, and the DWS signal which is calculated from the phase signal on individual photodiode quadrants. Sometimes the DC angular measurement is called DPS measurement, short for Differential Power Sensing. As for the longitudinal experiment sine waves are injected into DFACS, and the GRS signal is used as reference. The measured signals of the optical readout are compared with the injection, the main interest is in the DWS signal since this is used for the following experiments. Time series of these injections can be found in figures 6.10, 6.11, 6.12 and 6.13.

A signal with one cycle per hour and an amplitude of $600 \mu\text{rad}$ was injected in eta1, phi1, eta2 and phi2. The following coupling factors were calculated:

$$\text{eta1_DC} = 0.854 * \text{GRS_eta1}$$

$$\text{eta1_DWS} = 0.905 * \text{eta1_GRS}, \text{ for } \text{eta1} > 0$$

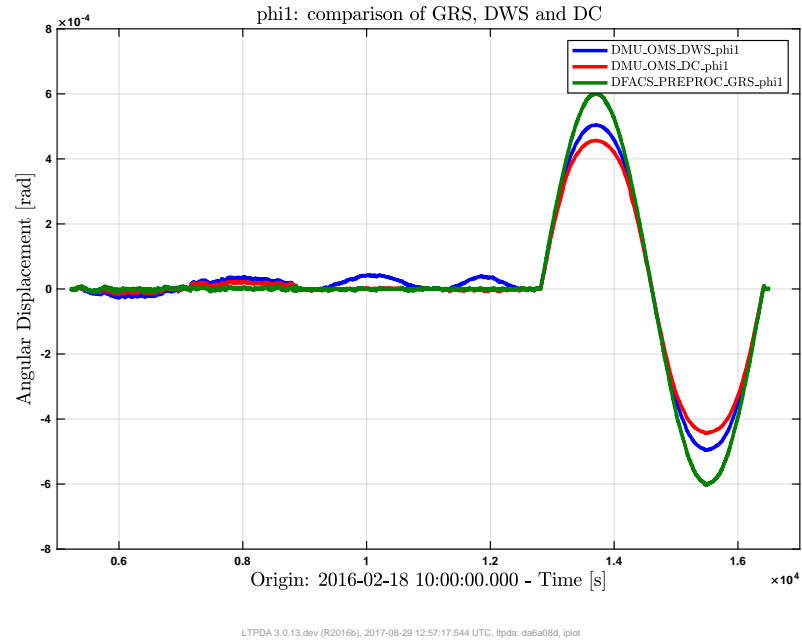


Figure 6.11.: The time series of the injection in phi1, performed on DOY049. Plotted is the injected signal (green), and the measured value of DWS (blue) and DC (red).t

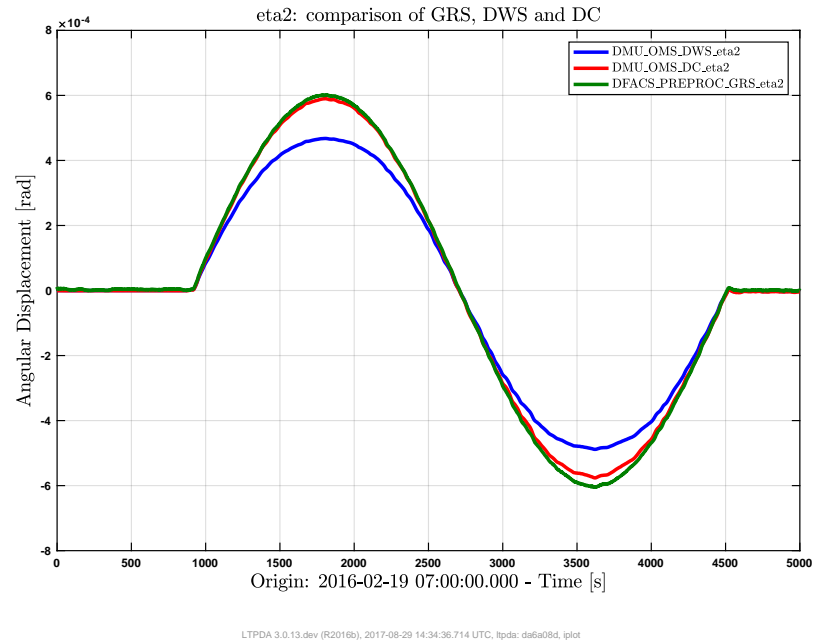


Figure 6.12.: The time series of the injection in eta2, performed on DOY050. Plotted is the injected signal (green), and the measured value of DWS (blue) and DC (red).

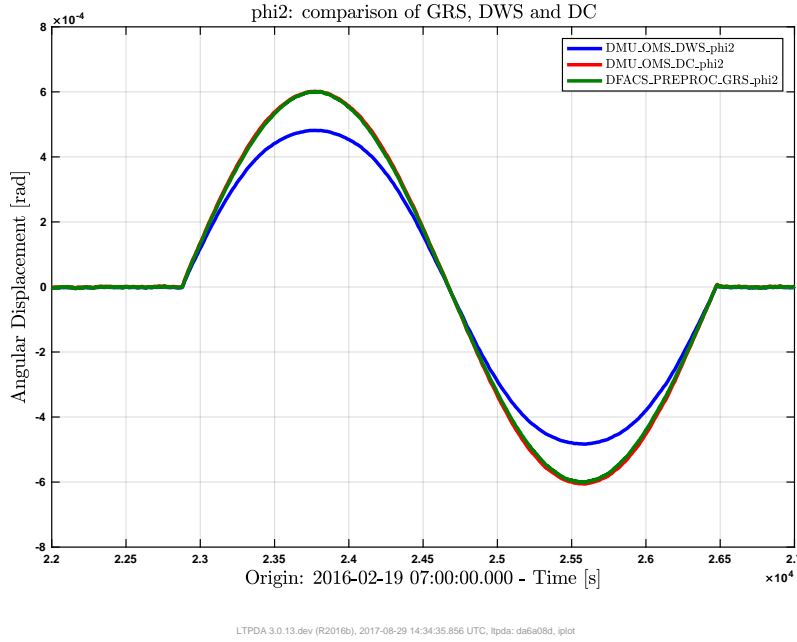


Figure 6.13.: The time series of the injection in phi2, performed on DOY050. Plotted is the injected signal (green), and the measured value of DWS (blue) and DC (red).

$$\text{eta1_DWS} = 0.893 * \text{eta1_GRS}, \text{ for } \text{eta1} < 0$$

$$\text{phi1_DC} = 0.833 * \text{GRS_phi1}$$

$$\text{phi1_DWS} = 0.94 * \text{phi1_GRS}, \text{ for } |\text{phi1}| < 150 \text{ murad}$$

$$\text{phi1_DWS} = 0.909 * \text{phi1_GRS}, \text{ for } 150 \text{ murad} < |\text{phi1}| < 300 \text{ murad}$$

$$\text{eta2_DC} = 0.778 * \text{GRS_eta2}$$

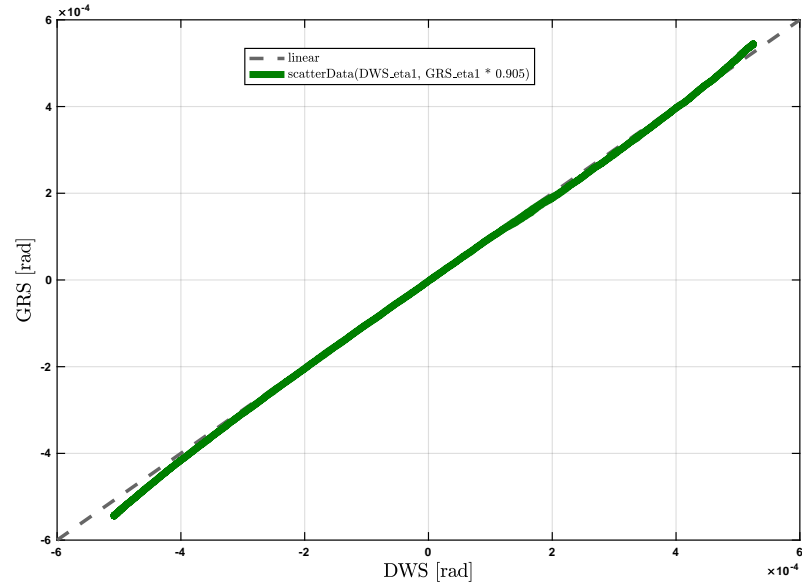
$$\text{eta2_DWS} = 0.983 * \text{GRS_eta2}$$

$$\text{phi2_DC} = 1.003 * \text{GRS_phi2}$$

$$\text{phi2_DWS} = 0.801 * \text{GRS_phi2}$$

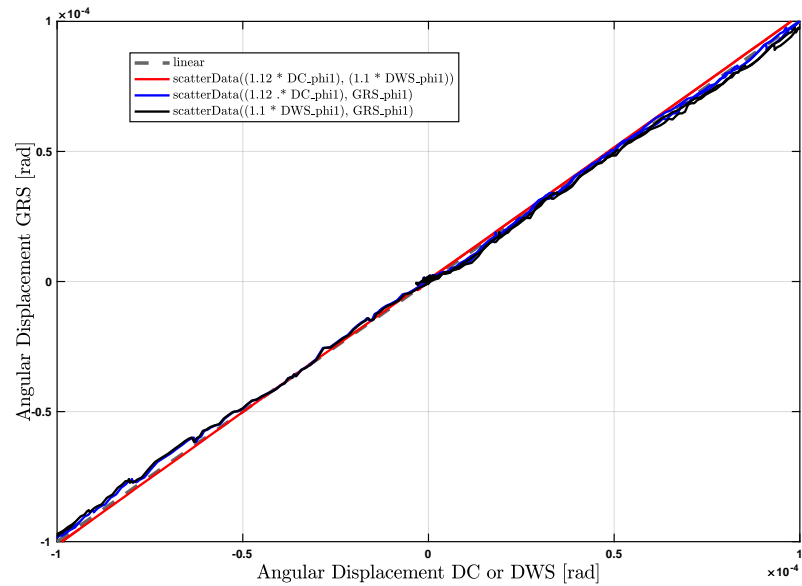
The coupling factors were fitted with a scatter plot between GRS measured angle, the fitting range was chosen to be near zero, an example plot of this fit can be found in figure 6.14 and 6.15. This scatter plot was analysed for all angles, within $200 \mu\text{rad}$ the different angular measurements are in agreement with each other, for bigger offsets nonlinear effects lead to offsets between the measurements. It's hard to tell which measurement to trust for bigger offsets, to further investigate this discrepancy the contrast of o12 and o1 can be plotted over the measured angular displacement.

The contrast is a parameter that describes how well the measurement beam and reference beam overlap on the photodiode, when the test mass angle is changed the contrast changes.



LTPDA 3.0.13.dev (R2016b), 2017-08-30 12:09:03.005 UTC, ltpda: dasa08d, ipilot

Figure 6.14.: The correlation between GRS injection and DWS measurement of eta1, after the DWS is calibrated.



LTPDA 3.0.13.dev (R2016b), 2017-08-30 14:52:51.248 UTC, ltpda: dasa08d, ipilot

Figure 6.15.: The correlation between GRS injection and DWS measurement of phi1, after the DWS is calibrated.

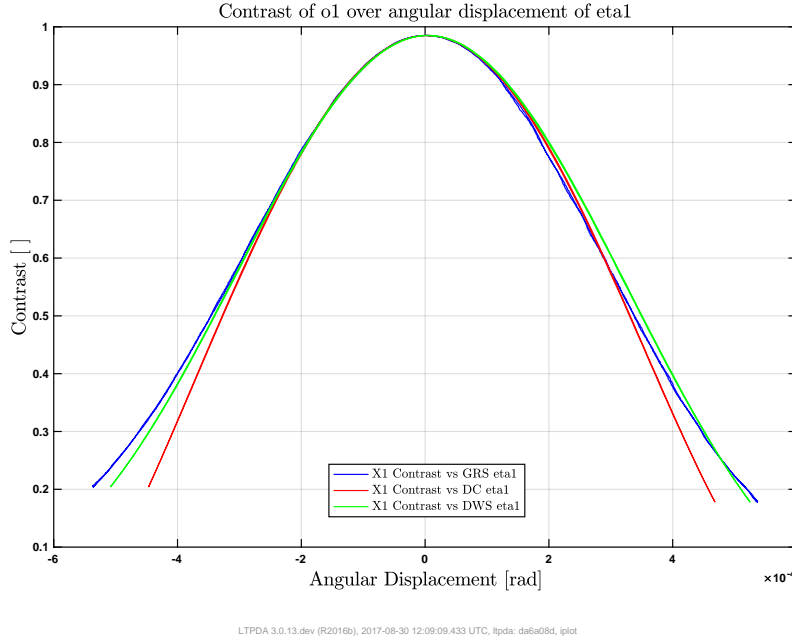


Figure 6.16.: The contrast of o1, plotted over the angular displacement of eta1 measured by the OMS and GRS, after the calibration. The difference between the different measurement schemes for bigger test mass offsets is easily visible.

The test masses were well aligned at the beginning of the measurement, big injections into the test mass angle reduce the contrast. Another way to compare the different measurements of the test mass angular orientation is a comparison of the contrast in o1 and o12 over test mass orientation, measured in different ways. For smaller angles these measurements agree, at bigger test mass offsets we can see the the graphs diverge. The fitted values were optimised for smaller test mass angular offsets, the plots of the contrast over different angular measurements can be found in figures 6.16, 6.17, 6.18, 6.19, 6.20 and 6.21.

The analysis of this experiment is ongoing.

A similar analysis was performed with data from the DWS step experiment as described in section 6.9.3. Using the parallel running DWS and GRS measurements the scatter shown in figure 6.22 is used to fit a straight line of the form

$$\alpha^{\text{GRS}} = G\alpha^{\text{DWS}} + d \quad (6.10)$$

to find calibration parameters for the sensors when torques are exerted in both angular degrees-of-freedom. From the fit it follows for a gain G and an offset d that

$$\eta_2^{\text{GRS}} = (1.1309 \pm 6.2 \times 10^{-5})\eta_2^{\text{DWS}} + (-7.895 \times 10^{-6} \pm 8 \times 10^{-9}) \text{ rad}, \quad (6.11)$$

$$\phi_2^{\text{GRS}} = (1.0968 \pm 4.6 \times 10^{-5})\phi_2^{\text{DWS}} + (17.980 \times 10^{-6} \pm 6 \times 10^{-9}) \text{ rad}. \quad (6.12)$$

From this linear model we find that the GRS is measuring between 9.9 % to 13.1 % larger values which are additionally offset by a constant during the DWS step experiment. The

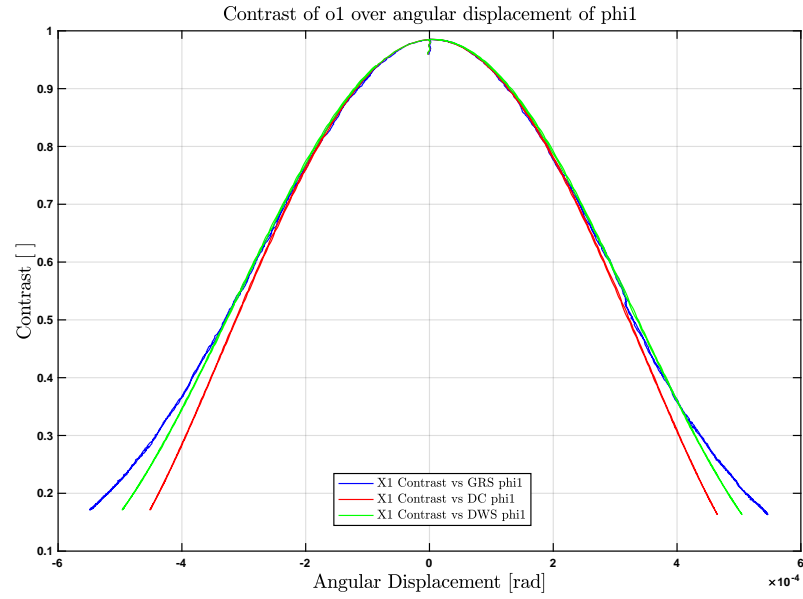


Figure 6.17.: The contrast of o1, plotted over the angular displacement of phi1 measured by the OMS and GRS, after the calibration.

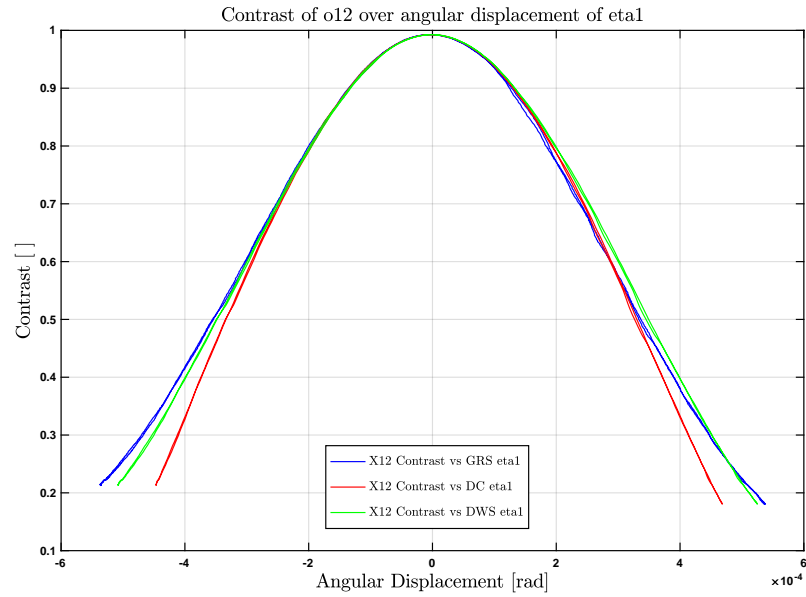


Figure 6.18.: The contrast of o12, plotted over the angular displacement of eta1 measured by the OMS and GRS, after the calibration.

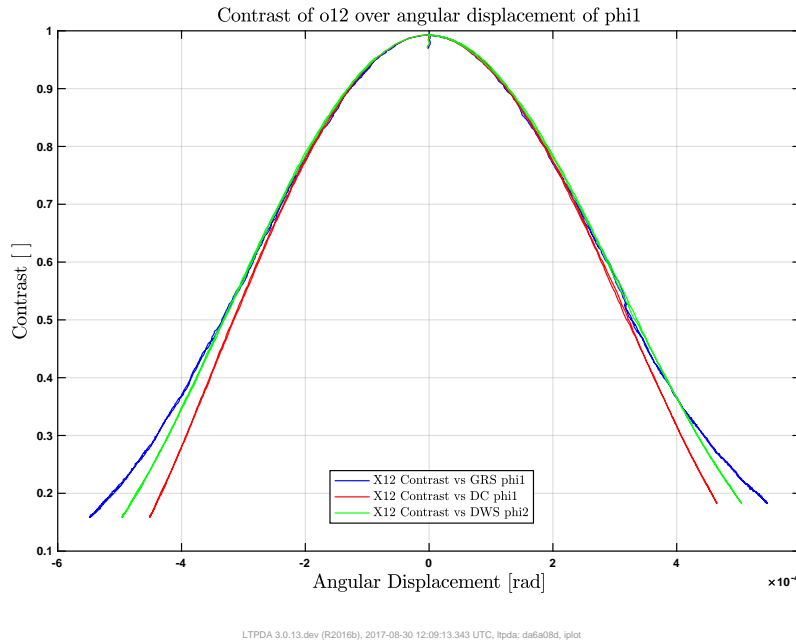


Figure 6.19.: The contrast of o12, plotted over the angular displacement of phi1 measured by the OMS and GRS, after the calibration.

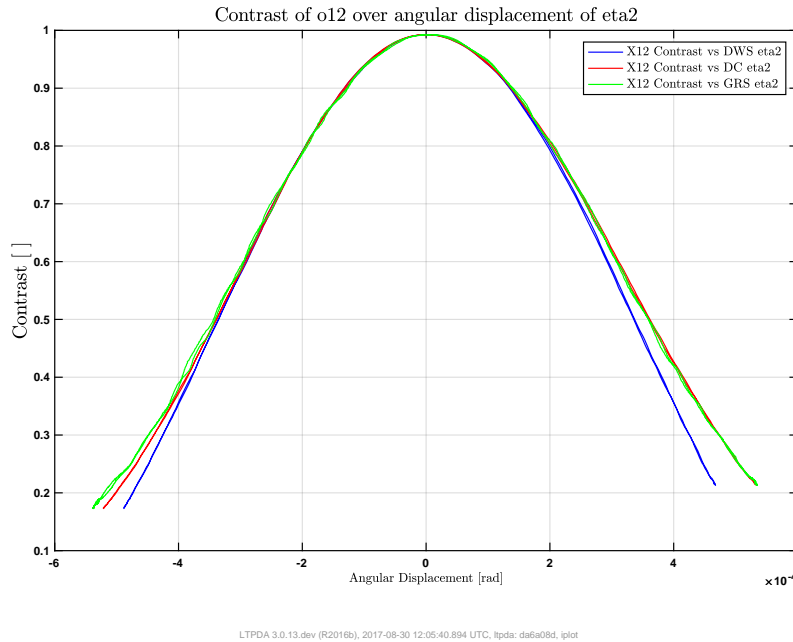


Figure 6.20.: The contrast of o12, plotted over the angular displacement of eta2 measured by the OMS and GRS, after the calibration.

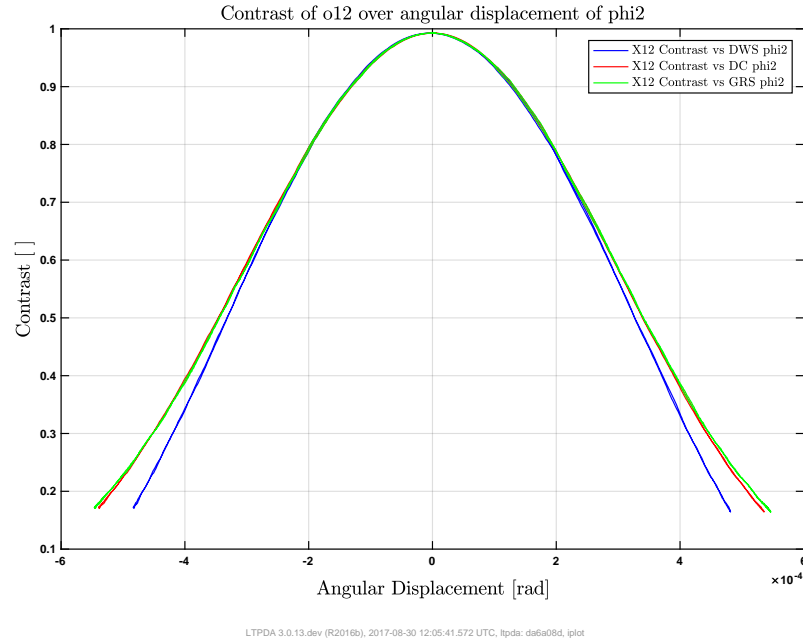


Figure 6.21.: The contrast of o12, plotted over the angular displacement of phi2 measured by the OMS and GRS, after the calibration.

linear relation appears to be valid except for large slews as shown in the smaller cut-out pictures. A possible explanation might depend on beam offsets on the photodiodes, which affects the interpretation of the actual test mass angle for a given set point.

6.6. Laser frequency noise stabilisation and interferometer path length differences

One possible noise contribution which has been known for a long time is the laser frequency noise. In general, laser frequency noise, δf , produces a phase noise, $\delta\phi$, in an interferometer if the light in the measurement beam does not travel exactly the same distance as in the reference beam. The difference of these two lengths is called a path length difference or an arm length mismatch, denoted Δs [34]. In a real interferometer, the path length difference is never exactly zero. This is also the case of the four interferometers on LISA Pathfinder. To minimise this undesired noise, there are two approaches, which are both used on LISA Pathfinder. We try to stabilise the laser frequency with a dedicated control loop to minimise the laser frequency noise, δf , and the utmost care was taken during the construction and integration of the satellite to have minimal path length differences, Δs .

6.6.1. Laser Frequency Noise Stabilisation

In LISA Pathfinder, the laser frequency noise is measured by a dedicated interferometer on the highly stable optical bench. Its most important characteristic is the intentional path length difference of 0.382 m [35]. It occurs in the fibres between the laser modulator unit and the optical bench. On the optical bench itself, the path of the two beams in the frequency interferometer is equally long. This intentional path length mismatch amplifies the frequency noise.

The measurement of the frequency interferometer is the input to the digital frequency stabilisation control loop. The frequency control loop is implemented digitally in the data management unit (DMU) and operates at 100 Hz. It is a nested loop containing both a fast frequency controller and actuator and a slow frequency controller and actuator [36]. The fast frequency actuator is a piezo which acts on the laser crystal and the slow frequency actuator is a heater [37].

The aforementioned control loop has been characterised in flight during dedicated experiments. The aim was to ensure that the loop performs as expected. In these experiments, a sinusoidal probing function was injected into the fast frequency controller error signal. The selected amplitude was 0.05 rad and eight frequencies from 0.011 Hz to 1.123 Hz were chosen. Each sinusoid lasted for 20 cycles at the respective frequency. Moreover, open-loop and closed-loop measurements of the laser frequency noise have been undertaken. During the nominal LPF mission, the frequency noise is downloaded at 1 Hz for most of the time to minimise the telemetry load. Thus, the long term monitoring can only be done with this data.

6.6.2. Measurements of Interferometer Pathlength Differences

We can measure the arm length mismatch in the interferometers X1, X12 and Ψ_R from the coupling of laser frequency noise into the respective interferometer. The path length difference is measured best when we amplify the frequency noise at known frequencies. To this end, we use sinusoidal injections similar to the loop characterisation experiment but at frequencies of 1.123 Hz and 2.879 Hz. The signals are injected for approximately half an hour each to improve the signal-to-noise-ratio. In the first version of the arm length mismatch

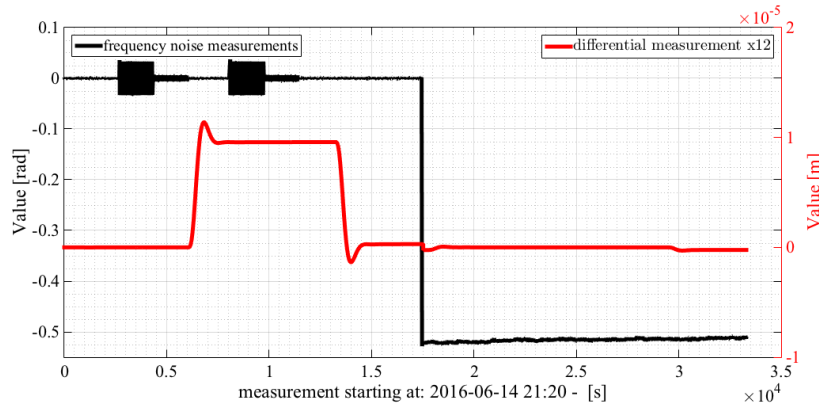


Figure 6.23.: The concept of the arm length mismatch experiment. The black trace (corresponding to the left y -axis) shows the laser frequency noise measurement. The two sets of two injections are clearly discernible. The DC value of the signal is at a lower level during the open-loop measurement. The distance between the two test masses is shown in red (refer to right y -axis). The second set of modulations is taking place at the offset position. Some transients are discernible.

experiment, the aforementioned signals have been injected two times. During the first set of injections, the reference test mass was at its nominal position and during the second set of injections, the same test mass was offset by approximately $9.5 \cdot 10^{-6}$ m. This allows us to check the two measurements for consistency and to get the sign of the mismatch. In the arm length mismatch experiment, these two sets of two injections each are followed by an open-loop measurement of the laser frequency noise at the original position of the reference test mass. From the increased noise, we can estimate again the arm length mismatch but with larger errors. The strategy of this experiment is summarised in Figure 6.23. The experiment was successfully executed on June 14th 2016. The arm length mismatch can be estimated best with this dedicated experiment.

6.6.3. Conclusion

On LISA Pathfinder, there is a dedicated interferometer to measure the laser frequency noise. This signal is used by a digital nested control loop which stabilises the laser frequency. A similar scheme is also being discussed for LISA. The interferometer path length differences on LISA Pathfinder are measured with a dedicated experiment which was successfully executed during the nominal mission on June 14th 2016. Analysis of this experiment and the control loop characterisation is ongoing and the results will be reported in a future publication.



6.7. OPD noise investigations

During LISA Pathfinder (LPF) operations many OPD relevant investigations were performed. A few preliminary results are published in [38].

The investigations focus on the following points.

- OPD control loop characterisation
- OPD noise and comparison between open and closed control loop
- OPD noise coupling into the other Interferometers (IFOs)
- OPD actuator step size

Analyses of these experiments are ongoing and the results will be reported in a future publication.

6.8. Relative Intensity Noise and interferometer path length differences

6.8.1. Introduction

In the first mission studies and noise projections Relative Intensity Noise (RIN) did not play a major role, and many steps were taken to suppress the other noise sources researched, for example with control loops 6.7, 6.6.1 and with careful design of the optical bench and readout system 2.

These steps were very successful, and as a result the overall sensing noise level is very low, and Relative Intensity Noise was found to be one of the limiting noise sources at higher frequencies. RIN is a property of the laser, and these intensity fluctuations are frequency dependant. From a theoretical analysis it was found that the coupling of RIN to the phase measurement of the measurement interferometers is dependant on the phase difference between the measurement interferometer signal and the reference interferometer signal. The derivation of this dependency will be published in a future paper.

The Optical Metrology System (OMS) uses heterodyne interferometry, as described in Section 2, the laser beam is split in two and Acousto Optic Modulators (AOMs) are used to shift the relative frequency of the two beams so that they have a difference of f_{het} , for LISA Pathfinder f_{het} is 1 kHz. In each interferometer the two beams are interfered on the recombination beam splitter, which creates a beatnote at f_{het} . This interference signal is measured by the photodiodes as a current change, and a transimpedance amplifier then converts this to a voltage fluctuation which is read out by the phasemeter. The phasemeter measures the phase of the signal at the heterodyne frequency. When the test mass moves, the optical path length of the measurement beam changes, and this in turn results in a change in the phase of this phasemeter output signal. The displacement of the test mass is calculated from this measured phase change.

A bandpass filter removes all other frequencies from the signal, and only noise in this narrow frequency band around the heterodyne frequency has an impact on the signal.

RIN at the heterodyne frequency couples directly into the phase measurement in the same way that the signal does. Additionally, RIN at twice the heterodyne frequency ($2f_{\text{het}}$) also



couples to the phase. Intensity fluctuations at $2f_{\text{het}}$ can also produce an interference signal at f_{het} .

These noise signals can not be separated from the intentional heterodyne signal in the phase calculation. Relative Intensity fluctuations with frequencies in the measurement band are suppressed by the phasemeter in the phase calculation, and they do not couple to the phase measurement to first order. These laser power fluctuations may lead to radiation pressure noise on the test mass, this noise source is not part of this discussion.

The signal in each interferometer is measured by two photodiodes, one from each port, or output, of the recombination beamsplitter and the outputs are called the symmetric and antisymmetric signals. These two signals are subtracted from another, in a method called balanced detection, the heterodyne signal has a phase difference of π between the two ports, thus a subtraction increases the signal strength by a factor 2. Whereas most noise sources are either subtracted or add quadratically, and the signal to noise ratio is improved. The coupling of $1f_{\text{het}}$ RIN noise to the signal has no sign difference between the two ports, and is subtracted from the final interferometer signal.

RIN at $2f_{\text{het}}$ couples in the same way as the heterodyne signal, and is not removed by balanced detection, but is also amplified by a factor of 2 in amplitude. An interesting detail for the later comparison of balanced to unbalanced detection is that the signal-to-noise ratio of $2f_{\text{het}}$ RIN does not change between the two measurement schemes.

The reference interferometer is built entirely on the optical bench and its measurement beam is not reflected from either of the test masses. It therefore measures phase fluctuations not caused by test mass motion, but due to relative pathlength fluctuations that occur prior to the light being input onto the highly stable optical bench. The measurement of this optical pathlength noise is used in the OPD control loop to suppress it, this is discussed in section 6.7.

To further suppress noise common to both interferometers the reference signal is subtracted from the measurement signal.

Since Relative Intensity Noise is a property of the laser beams it is the same in both interferometers, therefore $2f_{\text{het}}$ RIN is subtracted in normal operations. The reference interferometer also uses balanced detection, and does not contain $1f_{\text{het}}$ RIN.

This intensity noise is on the phase signal, the phase signal can be visualised as a phasor in the complex plane. If the signal in the measurement interferometer and the reference interferometer have a different phase, so the phasors, or vectors, point in different directions in the complex plane, the subtraction of $1f_{\text{het}}$ RIN does not work properly any more. This can easily be seen if one thinks of the subtraction and addition of vectors in 2D space. From the viewpoint of electrical signals this is not easily obvious however, and the exact properties of this subtracted signal with respect to the phase difference of the two signals was derived from the basic heterodyne signals. This derivation is the subject of a paper currently in development.

The phase between the measurement and reference signals changes when the test mass is moved, and we see an increase in noise at high frequencies if the test mass is moved from its nominal position.

6.8.2. Experiments

In this analysis we look at properties of the optical readout, all the analysis is performed in displacement, the units we use are [fm] and $\left[\frac{\text{fm}}{\sqrt{\text{Hz}}}\right]$. Most other LPF data analysis concerns forces on the test mass, and is therefore performed in the acceleration domain, with the units $\left[\frac{\text{fm}}{\text{s}^2}\right]$ and $\left[\frac{\text{fm}}{\text{s}^2\sqrt{\text{Hz}}}\right]$.

Two dedicated experiments were performed to measure the coupling of relative intensity noise to the length measurement. The aim of the first one was to confirm the theoretical noise-over-position behaviour for the flight optical metrology system, since balanced detection is on it is expected that RIN at $1f_{\text{het}}$ is removed from the signal, but RIN at $2f_{\text{het}}$ should still be present.

In the second experiment, balanced detection is switched off, and the subtraction properties of $1f_{\text{het}}$ RIN are measured.

In preparation for the mission, similar experiments were performed with an engineering model of optical bench in the laboratory at the AEI in Hannover. Due to the more noisy ground setup, additional RIN had to be fed into the measurement so that the effect was visible over the other noise sources. These lab experiments confirmed there was something worth investigating, and these initial experiments helped to design a flight experiment.

The experiments are very simple, the test mass was moved to a number of offsets from its nominal zero-phase difference between measurement signal and reference signal, this corresponds to a test mass position of 0 nm. At each position we perform a noise measurement. The limiting factor in this experiment is the time it takes the test mass to move to the new offset and stabilise, relative to most other experiments the test mass moves far distances of tens of nanometers per step. The noise measurement at each step should be short enough to have a reasonable amount of steps, but long enough to have enough averages to calculate the noise between 0.4 Hz and 5 Hz with a reasonable error. See figure 6.24 for the time series of the first step experiment.

To confirm the predicted noise shape, the test mass was moved over a big parameter space in the first experiments, with steps of 10 nm or 30 nm the test mass is moved from -270 nm to 790 nm, this corresponds to phase differences between the signals between $-\pi$ to almost 3π . In this experiment the noise over position measured fits to the prediction made for the coupling of relative intensity noise at two times the heterodyne frequency. This was expected because RIN at $1f_{\text{het}}$ is subtracted with balanced detection.

At each position the noise spectrum is calculated, and we take the mean value of this noise spectrum over a frequency band. This band is selected to exclude the spikes at 1, 2, 3, and 4 Hz and the rising noise towards lower frequencies, see figure 6.25.

The results of this experiment were compared to the noise at different test mass positions for other experiments, namely the free fall experiment, but also for small test mass motions during noise runs. The noise shape of this dedicated experiment is consistent in the position behaviour to the other experiments. The amplitude of the noise changes with the status of the laser and is different for each experiment.

In the second experiment the focus is more on the coupling of RIN near the optimal positions, this version has a smaller total range since the shape itself was established but more points with smaller step sizes.

Additionally for each step balanced detection is turned off for 25 minutes, RIN at the heterodyne frequency is no longer removed from the signal in this timespan. This allows a

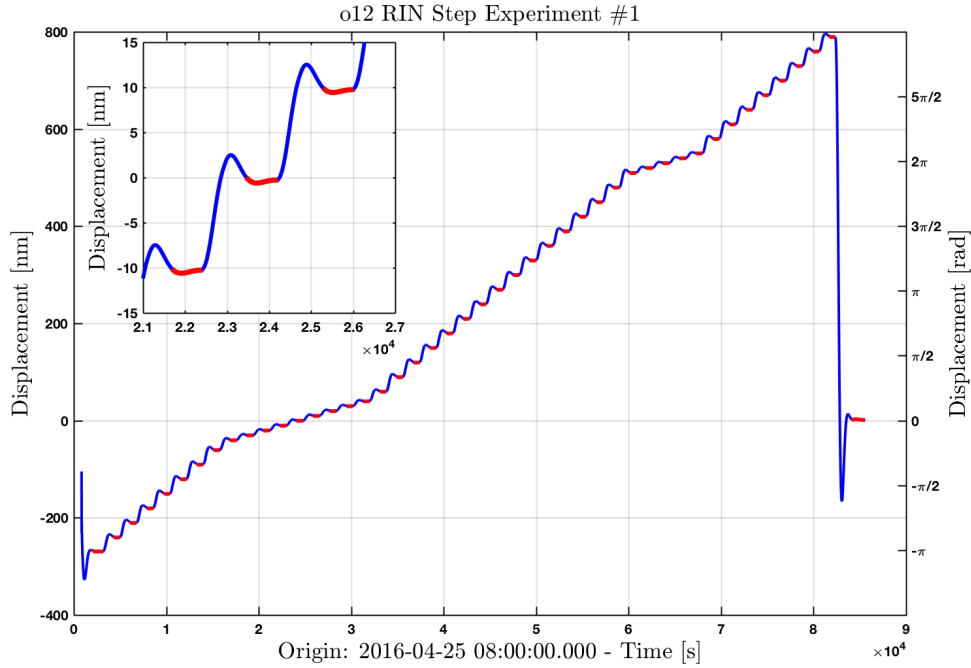


Figure 6.24.: The time series of the first step experiment, plotted in blue. At each step we select a quiet timespan, shown in red, and calculate average the noise level. The uncertainty on the test mass position comes from the drift during each step, the error is small compared to the range of test mass offsets.

direct comparison of the noise for the two settings for many test mass offsets. This setup aims to decouple the noise level of RIN at the heterodyne frequency, two times the heterodyne frequency, and the noise floor of ADC noise, electronic noise and shot noise. For some test mass offsets the o12, psiR and psiF signal is recorded at 100 Hz to further explain the noise behaviour at high frequencies. the test mass offset is 133 nm, which corresponds to a phase difference of $\frac{\pi}{2}$ between measurement and reference signal.

Due to a scheduling conflict with the cool down of the space craft before the start of the timeline the experiment did not run as planned. The timeline is cut short, and the temperature was not yet stable at the beginning of the experiment, which lead to an increase in noise.

For some of the steps we recorded 100 Hz data of the o12 signal, due to the high data rate the timespan is very short. In the plot 6.26 we show an example step of the second experiment.

In the same way as for the first experiment the noise for different test mass positions is calculated, some example spectra can be seen in figure 6.27, together with the IDL data for the same step.

6.8.3. Noise over position

For both step experiment the noise over position is calculated, in both cases for the frequency band between 0.55 Hz and 0.9 Hz. The distribution of steps is different, and since the

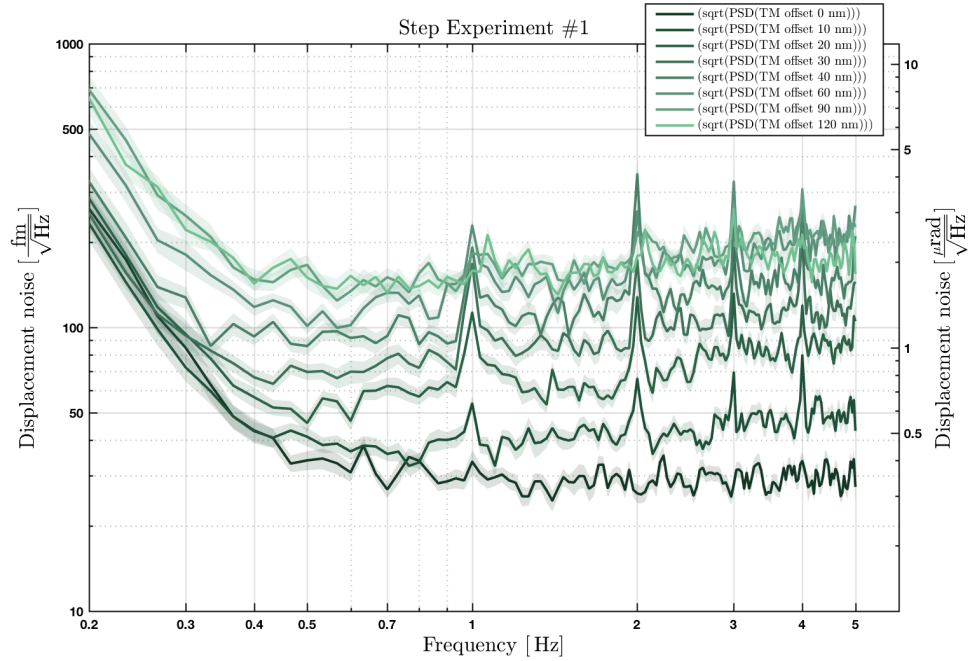


Figure 6.25.: Example spectra for test mass offsets between 0 nm and 120 nm, the spectra were calculated with 300 samples in each fft with an overlap of 50% and an Hanning window. The rise in noise for offsets towards a phase difference of π between the measurement and reference signal is visible, for the later analysis the average noise was calculated in the band between 0.55 Hz and 0.9 Hz. The analysis for higher frequencies is still ongoing.

experiments were performed almost a year apart at different temperatures and laser settings the amplitude of RIN is expected to be different, but the general behaviour should be the same. This is found to be true for the experiments performed.

A MCMC fit is used to calculate the RIN amplitude, implemented in LTPDA we use the following fit function:

```
% Parameters o12AB
params = [...
    LPFParam('r2_G', 130, 'fm Hz^(-1/2)', 'The Amplitude of RIN at 2kHz'),...
    LPFParam('noise_floor', 35, 'fm Hz^(-1/2)', 'noise floor')...
];

% Parameters o12A
params = [...
    LPFParam('r1_G_c', 130, 'fm Hz^(-1/2)', 'The Amplitude of RIN at 1kHz'),...
    LPFParam('noise_floor', 35, 'fm Hz^(-1/2)', 'noise floor')...
];

% Fit function
RIN1f = '(2*sqrt(2) * r1_G_c* sin(4*pi*0.5*1/(1064)*
```

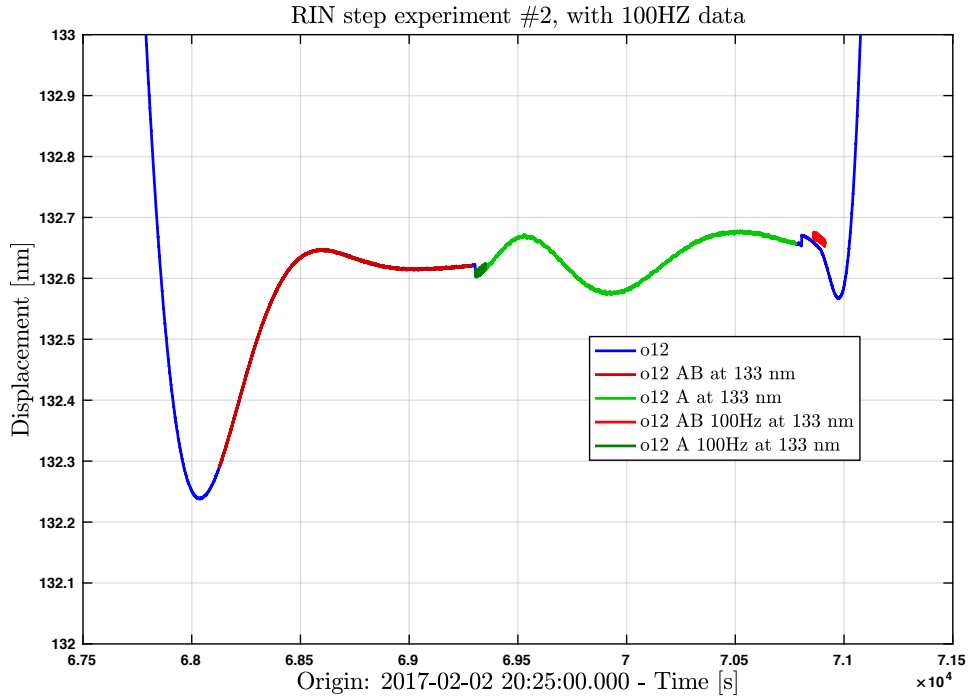


Figure 6.26.: An example step of the second step experiment. The timespan where balanced detection is on is shown in red, the shorter timespan in red is recorded at 100 Hz. Balanced detection is off in the green segments, again the shorter timespan is recorded at 100 Hz.

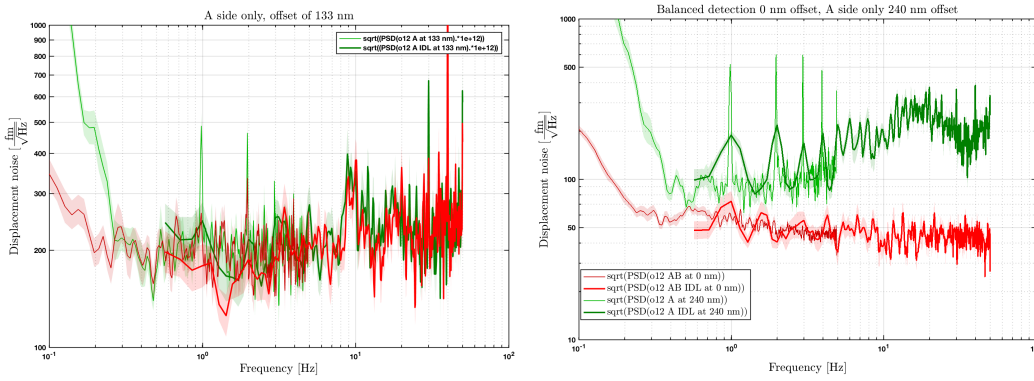


Figure 6.27.: The spectra were calculated with 700 samples in each fft with an overlap of 50% and BH92 window. In red is the measurement with balanced detection on, both 10 Hz data and 100 Hz data. Shown in green is the measurement with balanced detection off, also with 10 Hz and 100 Hz. The peaks visible for in the single side spectra are normally suppressed by balanced detection.



```
cos(2*pi*4.5/360) *(samples))).^2';  
RIN2f = '( sqrt(2) * r2_G * sin(4*pi* 1/(1064)*  
cos(2*pi*4.5/360) *(samples))).^2';  
floor = 'noise_floor.^2';  
  
% o12AB  
fit_function = [RIN2f '+' floor];  
% o12A  
fit_function = [RIN1f '+' RIN2f '+' floor];
```

The analysis for balanced detection is labeled with o12AB because the A side and B side of the interferometer are operational, in the unbalanced case only the A side is active. The A side of all interferometers is turned off, we're interested in the subtraction of this noise, and if only the measurement interferometer had one diode turned off then only in this signal $1f_{\text{het}}$ RIN would be present, and the reference signal would not have the same noise to subtract in the calculation of $o12 = x12 - xR$.

At first the fit included the frequency and an offset from zero, but these parameters were removed because the error on the result was reliably bigger than the difference to the expected values of 1064 nm and 0 nm, respectively.

The analysis is still ongoing, but it can already be said that balanced detection and the suppression of a reference, together with a careful analysis of the interferometrically optimal test mass position is important for noise suppression at higher frequencies.

The results of these experiments will help with noise projections on LISA, and with the efforts to reduce the impact of this test mass position dependant noise.

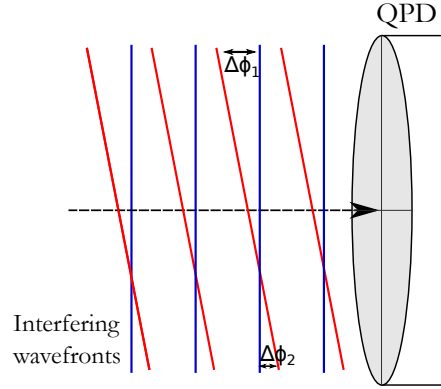


Figure 6.28.: The principle of Differential Wavefront Sensing. A tilted measurement beams interferes with a local reference such that a phase difference between the top and bottom or left and right parts of the profile can be detected by demodulating the single quadrants of a photodiode and comparing them to each other.

6.9. Differential Wavefront Sensing

6.9.1. Introduction

Differential Wavefront Sensing (DWS) is an interferometric measurement technique that is used in LPF OMS to determine the angular coordinates ϕ and η for each of the test masses. It drives the Drag-Free Attitude Control System (DFACS) when the spacecraft is in nominal science mode. The x_1 interferometer is used to derive the test mass one angles ϕ_1^{DWS} and η_1^{DWS} . For test mass two, the differential x_{12} readout is combined with test mass one angles to calculate ϕ_2^{DWS} and η_2^{DWS} . This is done by demodulating the individual segments of Quadrant-Photodiodes (QPD) to compare the relative phase difference between the wavefronts of the interfering measurement and reference beams for groups of two complementary quadrants per photodiode.

The working principle, shown in figure 6.28, is based on spatially varying phase differences between arriving wavefronts. They result in a change of the total phase distribution across all quadrants and can be used to detect beam tilts as a weighted phase average. DWS is often applied in auto-alignment schemes for gravitational wave detectors and has become a standard technique [39, 40, 41].

The LISA Pathfinder phasemeter processes all four photodetector quadrants A, B, C, D , using a Single-Bin Discrete Fourier Transformation (SBDFT), as described in Section 2.1. The resulting complex values, F , contain the encoded phase information and can be used to construct the groups of complementary quadrants:

$$F_i^{\text{left}} = F_{i,A} + F_{i,C}, \quad (6.13)$$

$$F_i^{\text{right}} = F_{i,B} + F_{i,D}, \quad (6.14)$$

$$F_i^{\text{up}} = F_{i,A} + F_{i,B}, \quad (6.15)$$

$$F_i^{\text{down}} = F_{i,C} + F_{i,D}, \quad (6.16)$$

where $i \in \{R, F, 1, 12\}$ refers to the respective interferometer.

By subtracting the left and right, and up and down quadrants according to

$$\begin{aligned} \text{DWS}^\phi &= \arg(F^{\text{left}}) - \arg(F^{\text{right}}), \\ \text{DWS}^\eta &= \arg(F^{\text{up}}) - \arg(F^{\text{down}}), \end{aligned} \quad (6.17)$$

the angular phase information can be extracted, while the equally distributed longitudinal phase cancels.

The DWS readout can be related to equivalent test mass angles for a certain linear range, as the beam tilt is directly influenced by the test mass orientation. The general relationship however, is non-linear with a linear regime only for small test mass tilts. The non-linearity originates from the interfering Gaussian beams. In [41] the three main factors are summarised:

- The measurement beam centre is translated during a test mass tilt, resulting in spatially separated interfering beams.
- The QPD slits cut off certain parts of the beams.
- Where there are large test mass rotations, destructive interference between wavefronts across the QPD can occur, causing phase jumps within the detector area.

In LPF, the raw DWS phase is assumed to be proportional to equivalent test mass angles over a range of at least $-100 \mu\text{rad}$ to $100 \mu\text{rad}$ test mass tilt, as shown in [42]. There, it was shown that the DWS signals are highly linear for an even larger range, but that the non-linearity of the DWS response is clearly visible for test mass angles exceeding $\pm 200 \mu\text{rad}$. The linear coupling factors k_i a given angular degree-of-freedom were determined during ground measurements with the flight model of the optical bench.

$$\begin{pmatrix} \text{DWS}^{\phi_1} \\ \text{DWS}^{\eta_1} \end{pmatrix} = \begin{pmatrix} k_1 & 0 \\ 0 & k_2 \end{pmatrix} \begin{pmatrix} \phi_1^{\text{DWS}} \\ \eta_1^{\text{DWS}} \end{pmatrix}, \quad (6.18)$$

$$\begin{pmatrix} \text{DWS}^{\phi_{12}} \\ \text{DWS}^{\eta_{12}} \end{pmatrix} = \begin{pmatrix} k_3 & 0 \\ 0 & k_5 \end{pmatrix} \begin{pmatrix} \phi_1^{\text{DWS}} \\ \eta_1^{\text{DWS}} \end{pmatrix} + \begin{pmatrix} k_4 & 0 \\ 0 & k_6 \end{pmatrix} \begin{pmatrix} \phi_2^{\text{DWS}} \\ \eta_2^{\text{DWS}} \end{pmatrix}, \quad (6.19)$$

They are typically in the order of ~ 5000 for the OMS. This huge magnification of test mass angles indicates the excellent sensitivity of DWS. Using equations 6.18 the DMU calculates the equivalent test mass angles by inverting the coupling factors



$$g_1 = \frac{1}{k_1} = -0.00020177563, \quad (6.20)$$

$$g_2 = \frac{1}{k_2} = 0.00020859408, \quad (6.21)$$

$$g_3 = -\frac{k_3}{k_1 k_4} = -0.0001751037, \quad (6.22)$$

$$g_4 = \frac{1}{k_4} = -0.00018910741, \quad (6.23)$$

$$g_5 = -\frac{k_5}{k_2 k_6} = 0.00018775076, \quad (6.24)$$

$$g_6 = \frac{1}{k_6} = -0.00019290123 \quad (6.25)$$

and applying them to the electrical phase according to

$$\phi_1^{\text{DWS}} = g_1 \text{DWS}^{\phi_1}, \quad (6.26)$$

$$\eta_1^{\text{DWS}} = g_2 \text{DWS}^{\eta_1}, \quad (6.27)$$

$$\phi_2^{\text{DWS}} = g_3 \text{DWS}^{\phi_1} + g_4 \text{DWS}^{\phi_{12}}, \quad (6.28)$$

$$\eta_2^{\text{DWS}} = g_5 \text{DWS}^{\eta_1} + g_6 \text{DWS}^{\eta_{12}}, \quad (6.29)$$

converting from the raw electrical phase in [rad] to equivalent test mass angle, typically in [μrad]. The signal description above can be found in many mission publications (in this case see [43]).

6.9.2. DWS in-orbit

This section gives an overview of the DWS performance during the mission, specifically before and after test mass re-alignment procedures. Parts of this work can also be found in [43, 44]. A non-perfect test mass alignment is causing the apparent noise excess between 20 mHz to 120 mHz in the differential spectrum (see [45]) of the longitudinal interferometer. The effect can be mitigated by subtracting a model, but it can also be physically reduced by re-aligning the test masses and thus minimizing the offending coupling. Every alignment results in a new TM orientation.

Figure 6.29 shows selected DWS spectra during noise runs before and after re-aligning the test masses and the angular sensitivity requirement, which is defined as

$$S_{\text{angular}}^{1/2} \leq 20 \times 10^{-9} \frac{\text{rad}}{\sqrt{\text{Hz}}} \sqrt{1 + \left(\frac{f}{3 \text{ mHz}} \right)^{-4}} \quad (6.30)$$

for $1 \text{ mHz} \leq f \leq 30 \text{ mHz}$ [46].

During the first engineering days on DOY75/76 (day-of-year, 2016) the test masses were

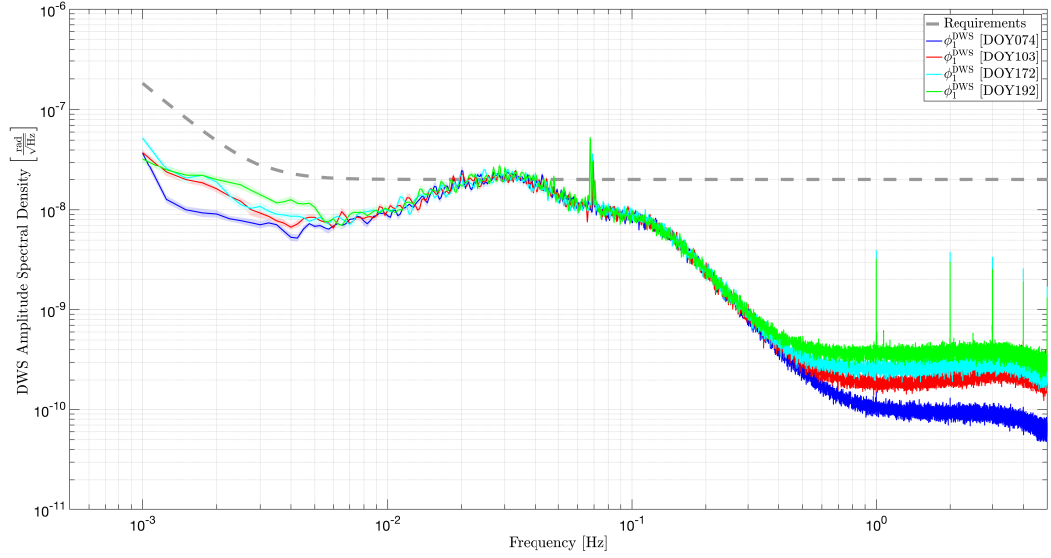


Figure 6.29.: Amplitude spectral density of ϕ_1^{DWS} for four selected dates. They cover the period before and after each of the test alignment procedures. In the frequencies above 0.8 Hz a quasi-flat noise floor is reached for each of the points. Harmonic peaks starting at 1 Hz are apparent and originate from the on-board clock. At lower frequencies real test mass motion seems to dominate the spectrum and is reaching the requirement around 30 mHz. The quasi-flat noise floor can be used to estimate an average noise performance. Another signal around 70 mHz is apparent but not yet identified.

set from $\text{DWS} = 0 \text{ urad}$ to

$$\eta_1^{\text{DWS}} = -3.5 \mu\text{rad}, \quad (6.31)$$

$$\phi_1^{\text{DWS}} = -59.25 \mu\text{rad}, \quad (6.32)$$

$$\eta_2^{\text{DWS}} = 3.5 \mu\text{rad}, \quad (6.33)$$

$$\phi_2^{\text{DWS}} = -21.35 \mu\text{rad} \quad (6.34)$$

and again on DOY171 to further improve the alignment with

$$\eta_1^{\text{DWS}} = -2.14 \mu\text{rad}, \quad (6.35)$$

$$\phi_1^{\text{DWS}} = -57.32 \mu\text{rad}, \quad (6.36)$$

$$\eta_2^{\text{DWS}} = 10.3 \mu\text{rad}, \quad (6.37)$$

$$\phi_2^{\text{DWS}} = -33.01 \mu\text{rad}. \quad (6.38)$$

Ongoing analysis showed that there was a consecutive correction needed on DOY177, setting



DOY	$\bar{S}_{\eta_1}^{1/2 \text{DWS}}$	$\bar{S}_{\phi_1}^{1/2 \text{DWS}}$	$\bar{S}_{\eta_2}^{1/2 \text{DWS}}$	$\bar{S}_{\phi_2}^{1/2 \text{DWS}}$	all in prad/ $\sqrt{\text{Hz}}$
074, 2016-03-14	100.45	96.90	124.29	120.73	
103, 2016-04-12	105.61	205.02	128.69	138.32	
172, 2016-06-20	117.96	277.78	188.61	204.32	
192, 2016-07-10	142.63	379.92	233.67	206.38	

Table 6.1.: DWS performance in between test mass alignment procedures at various times during the mission for $0.8 \text{ Hz} \leq f \leq 2.8 \text{ Hz}$. It can be seen that the values vary depending on the test mass alignment, but stay in the order of a few 100 prad/ $\sqrt{\text{Hz}}$. The relative standard error is below 0.2 %.

the test masses to their current

$$\eta_1^{\text{DWS}} = -4.9 \mu\text{rad} \quad (6.39)$$

$$\phi_1^{\text{DWS}} = -61.2 \mu\text{rad} \quad (6.40)$$

$$\eta_2^{\text{DWS}} = -3.3 \mu\text{rad} \quad (6.41)$$

$$\phi_2^{\text{DWS}} = -9.7 \mu\text{rad}. \quad (6.42)$$

offsets. They are commanded directly as DFACS controller calibration setpoints. The dates chosen here are in between each of the hardware calibration days on DOY74, DOY103, DOY172 and DOY192. Table 6.1 gives the resulting average noise levels for each of the setpoints given above. To estimate the average noise levels their power spectral densities are calculated with Welch's averaged periodogram algorithm, using 30 averages per bin and subsequent averaging in the frequency band from 0.8 Hz to 2.8 Hz. The lowest noise level is reached in ϕ_1^{DWS} with 96.9 prad/ $\sqrt{\text{Hz}}$ at a DWS alignment close to zero. The performance is well below the requirements for all ranges where test mass motion is not dominating the spectrum. Figure 6.30 shows the distribution of measured noise over test mass position. Especially for larger misalignments the an increased noise can be observed, while most configurations close to zero yield similar linear densities. However, especially around $-60 \mu\text{rad}$ in ϕ_1^{DWS} the noise level increases by a large amount. Here it is suspected that beam clipping on the quadrant photodiode slits influences the measurement for different relative alignments between test mass one and test mass two. Also, the Relative Intensity Noise (RIN) of the laser is known to change over time and couples noise into the phase readout.

6.9.3. The DWS step experiment

The test mass alignment procedures have shown that it is possible to measure a varying noise floor for different orientations of the test masses. This gives the possibility to systematically analyse the noise behaviour of DWS, also with regard to ESA's L3 Laser Interferometer Space Antenna (LISA) mission.

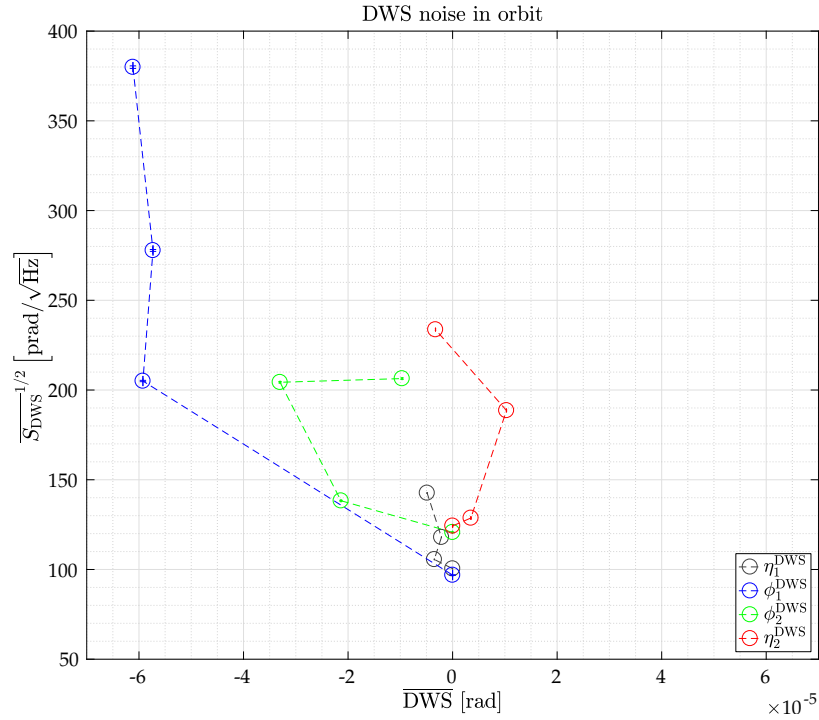


Figure 6.30.: DWS average noise spectral density before and after alignment procedures throughout the mission. The values have been calculated for $0.8 \text{ Hz} \leq f \leq 2.8 \text{ Hz}$ using every fourth sample after applying Blackman-Harris windows with 50 % overlap and 30 averages. Their relative standard error is below 0.2 %.

Motivation and overview

In LISA, non-vanishing DWS signals will originate from motion between the three satellites in combination with their long arm lengths. A mechanism to compensate for out-of-plane angles between the received and emitted beams of the satellites is planned, and the angular alignment is expected to contribute readout noise through DWS, especially because beam tilts are magnified by telescopes aboard the LISA satellites, causing relatively large DWS phase differences on the quadrants.

The DWS noise behaviour was investigated with LISA Pathfinder through a dedicated investigation. The experiment is designed to quantify different noise levels and investigate their coupling. It assesses the phase noise in the DWS readout regarding its amplitude and phase (or, test mass angle) dependence and estimates possible noise sources and coupling mechanisms, helping to draw conclusions for requirements on the LISA point-ahead configuration.

Experimental concept

The experimental concept can be summarized as a number of angular test mass offsets, commanded via the electrostatic controller, for which the test mass orientation is measured. Afterwards the resulting amplitude spectral noise density for each of the offsets (steps) is calculated. LISA Pathfinder has proven to be quiet enough to reach a quasi-flat noise floor

within the high frequency regime in the angular test mass readout, where no test mass motion is apparent.

For this experiment test mass two is actuated. It is located closer to the differential interferometer measurement diodes and causes a smaller lateral beam offset when tilted. Another benefit is that the differential interferometer is less susceptible to environmental disturbances.

The somewhat randomly chosen test mass tilts are shown in figure 6.31. With these

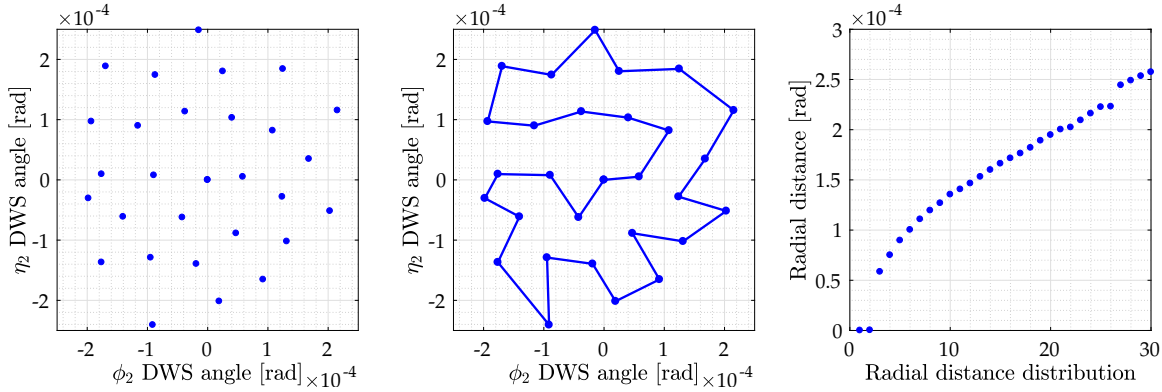


Figure 6.31.: The commanded test mass two tilts are shown in the ϕ_2, η_2 parameter space. All points are randomly placed such that the maximum radial distance is smaller than $260 \mu\text{rad}$. The middle plot shows the shortest connecting path of all points, calculated by a travelling salesman algorithm (courtesy of G. Heinzel). It reduces test mass trajectories between set points and the risk of larger overshoots.

set-points a large parameter space can be sampled. During the nominal mission it has not been possible to rotate the test masses to larger angles due to spacecraft safety considerations. A more sophisticated version of this experiment was only planned for the mission extension and is therefore not part of this report.

Investigation summary

The experiment was run on DOY154 of the nominal mission. The resulting time series can be found in figure 6.32. Both the angular DWS and the longitudinal interferometer readout are shown for the whole 24 hours of the experiment. It can be seen that every step, which has a combined commanding and holding duration of 45 min, is reached in less than 30 min, followed a quiet measurement period of various length. In comparison, tilt-to-length coupling in x12 motion, introduced by the commanded torques, experiences a slower impulse response of the suspension controller and is actuated back to its zero position. Furthermore, every set point shows an overshoot of different length, when the test mass rotates further than commanded, due to the relatively high slew velocities picked up on the way to a new point. The controllers are not designed to counteract them quickly enough, from which an upper limit of set points is deduced. The maximal overshoot is just below $30 \mu\text{rad}$ in η_2 . They are analysed in figure 6.33.

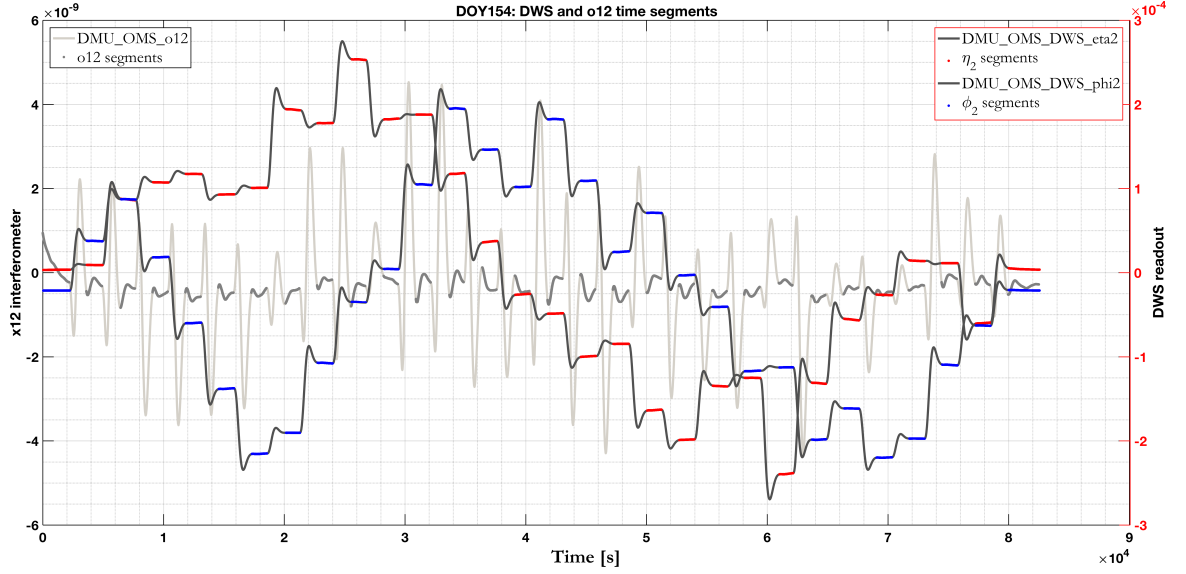


Figure 6.32.: Time series of the measured slews in the DWS step experiment.

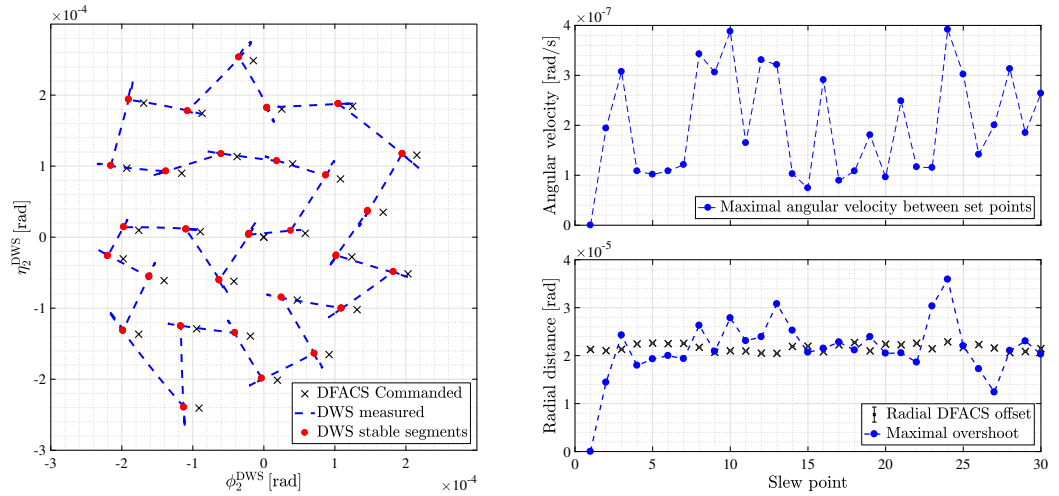


Figure 6.33.: The left plot shows the test mass two trajectory in the angular parameter space as measured by DWS. Stable segments that are used in subsequent analysis are marked in red, as well as the commanded slews to the DFACS control. The offset to those is shown in the bottom right figure and has a mean of $21.7 \mu\text{rad}$. The maximal radial overshoot related to its commanded slew is shown. An overall maximal overshoot is reached at slew point 24 with a deviation of $36 \mu\text{rad}$. The net angular velocity was maximal during the transition from set point 23 to 24 with $0.39 \mu\text{rad/s}$, as can be seen in the top right plot.



The analysis shows a different amplitude spectral density for every set-point. It increases for larger misalignments, i.e. larger phase differences on the measurement diodes. For angles between $-250\,\mu\text{rad}$ to $250\,\mu\text{rad}$ the contrast remains in the range of 59.4 % to 97.9 % (not shown here). A publication with more in-depth results using a corresponding coupling model is in preparation.

6.10. OMS timing investigation

The OMS on LPF is operating on the Data Management Unit (DMU) clock. The phasemeter is synchronised to the same clock as the DMU and sends its phase measurements at 100 Hz to be processed by the DMU.

In science mode the Drag Free and Attitude Control System (DFACS) uses 10 Hz OMS science data from the DMU for the attitude control of the Spacecraft (SC). The DFACS is running on the time of the Onboard Computer (OBC) which is called Onboard Time (OBT). Because the independent clocks drift against each other, a synchronisation is required for the data transfer between both timing domains.

This section explains the timing of the relevant OMS parameters, synchronisation methods and challenges that showed up during mission operations.

6.10.1. OMS science data timing

The OMS science parameters (also called telemetry TM(128,3)) are generated with high priority at 10 Hz. This is done with a moving average (10 taps FIR) filter.

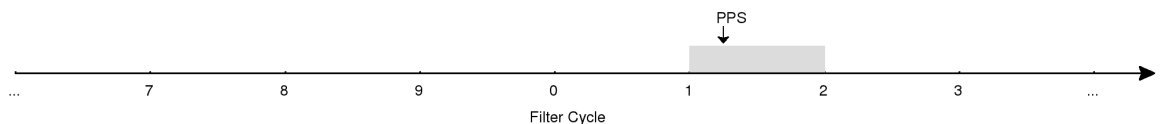


Figure 6.34.: The cycle counter is incremented at 100 Hz. When it reaches 10 it is set back to 0 and an averaged 10 Hz sample is computed from the last 10 samples. The 1 PPS signal from the OBC is used for synchronisation. The grey area marks the time when the 1 PPS signal is expected to occur.

The digital filter is computed at 100 Hz - for every sample that comes from the phasemeter. The cycle counter starts at 0 and a filtered value is added to the buffer. At the end of one cycle the counter is incremented. If it reaches 10 the buffer is added up and the OBC can fetch the data. This data transfer happens 10 times per second.

The DMU gets a synchronise command from the OBC via a 1 PPS (pulse per second) signal. Then the cycle counter is checked to be 1. Because the DMU and OBC clocks drift and there is some timing jitter the counter can be 0 or 2 when the check occurs.

A value 0 means that the DMU clock is slower than the OBC clock. The filter uses an old sample from the last block of 10 samples. So, only 9 new samples are in the filtered data that goes to the OBC. In addition, this data arrives about 90 ms after the data before.

When the 1 PPS arrives and the cycle counter is 2 the DMU clock is faster than the OBC clock. From the 2 samples that already were in the buffer only the second one is kept and the cycle counter is set back to 1. When the counter reaches 10 the data gets transmitted to the OBC at about 110 ms after the data before.

The OMS science data has OBC timestamps that are correlated to UTC (via the ground time correlation) before the parameters are stored in the LTP Data Analysis Software Toolbox (LTPDA) repository. In the OMS science parameter packet (CDM99255) there is also a timing parameter (CDT96255) included. It is used by the LTPDA preprocessing to correct the timestamps. The original timestamps are the OBC time when the data was



fetches by the OBC. The corrected timestamp is the OBC time when the data was created which is then correlated to UTC.

6.10.2. HK data timing

The HK parameters from the laser control loops (TM(3,25), packet LSM10054) are created as described in [47] chapter 4.4. The 1 Hz data is generated in the DMU by averaging 100 samples. The OBC then picks up this low priority data and applies its timestamp.

In the LTPDA repository the HK parameters have already a timestamp that is correlated to UTC (achieved via the ground time correlation).

Since the 15th of April 2016 a parameter (LST99021) to allow the correlation back to OBT was added to the LSM10054 packet. At the same time LST91001 .. LST91006 parameters were introduced to allow the calculation of the delay between the creation of the 1 Hz data in the DMU and the time when the parameters were picked up by the OBC. Because these parameters get updated once a day, it could be verified that the delay is about 0.7 s over a longer period of time. This information was supposed to help correcting the HK parameter timing for TF measurements (see section 6.10.3). But, it turned out that HK and OMS science parameters do drift and can not be corrected by a static daily delay term.

Furthermore, a bug in the DMU software was identified that resulted in 101 samples being averaged instead of 100 samples (one sample was processed twice). The problem was not corrected.

6.10.3. Mixed timing OMS TFs

To characterise and verify the performance of the digital OMS control loops investigations were designed before the launch of LPF. These investigations mainly base on TF measurements between 2 points in the loop while injecting sine waves (see sections 6.6.1 and 6.7). Unfortunately, these points are represented by parameters from different packets with different timestamps.

The obvious method to get the HK and OMS parameters on the same timing grid is to use the LTPDA preprocessing. Because the resulting TFs showed physically impossible negative delays with an additional drift the preprocessing was not used. Another drawback was the beat-note like amplitude modulation as discussed in section 6.10.4.

The following solutions were investigated.

Timing correction by fixed values

With the daily timing parameters (section 6.10.2) a delay between the generation of the HK data and the final timestamp from the OBC could be determined to be about 0.7 s. After correcting the HK parameters by subtracting this delay they should match with the OMS science parameters that were LTPDA preprocessed.

The correction works but showed at least the following drawbacks.

- Timing jitter (about 25 ms) of the HK parameters. This is a result of the low priority processing of HK data by the OBC.
- The correction doesn't work over some hours. There seems to be an additional timing drift.

- The matching of the amplitudes of the corrected parameters gets worse over time. Probably, an effect of the preprocessing as described in section 6.10.4.

Timing correction by cross-correlations and TFs

The OPD and laser frequency loops (in nominal state) use the longitudinal phase read-out of their IFOs as the input of their control loops. The phase read-outs (PSI_R and PSI_F) are OMS science parameters whereas the controller inputs (DMU_OMS_FAST_FREQ_CTRL_ERROR and DMU_OMS_OPD_CTRL_ERROR) are HK parameters. Because both IFO read-outs and controller inputs have the same data (with a sign change) we can use cross-correlations or TFs to determine the delay / timestamp mismatch between the parameters.

The same drawbacks as for the correction by a fixed value were found.

But, the cross-correlations and TFs are used as tests to prove that the next method (correlating to DMU time) works correctly. Therefore, the tests were done on the timing corrected data before and after the loop injections.

Correlating to DMU time

Correlating the parameters to DMU time has some advantages.

- The 1 Hz HK parameters are generated by averaging 100 samples in the DMU. So, they are already at DMU time. Only the timestamps have to be replaced by a 1 s grid. No interpolation has to be done.
- The 10 Hz OMS parameters have the slips of samples as described in section 6.10.1. The slips can be found with the timestamp differences between 10 Hz samples and allow to put the samples back on a (100 Hz) DMU time grid.

Before correcting the 10 Hz OMS parameters timestamps they get the recovered OBT (GST39999) timestamps applied to get rid of the additional correlation to UTC (via the ground time correlation).

Unfortunately, the 10 Hz OMS parameters still have to be interpolated coming from the 100 Hz DMU time grid to the 1 Hz DMU time grid.

Furthermore, every 10 Hz OMS sample is averaged from (usually) ten 100 Hz samples. When ten of the 10 Hz samples get averaged to one 1 Hz sample it doesn't mean it includes the same 100 samples as the 1 Hz HK sample. This is because the HK and the OMS data generating processes did not start at exactly the same time.

In addition, the mentioned problems still apply.

- The 1 Hz HK parameters are generated by averaging 101 samples (one is doubled). So, the amplitude is not correct.
- The 10 Hz OMS parameters lose or double one 100 Hz sample when a timing slip between DMU and OBC clock occurs (every ≈ 3700 s). So, the amplitude is not correct.

The correlation with DMU time is useful for the TF measurements because it only involves DMU parameters. For experiments with non-DMU parameters it is less useful because this data then has to be interpolated onto the DMU timing grid.

6.10.4. Resampling artefacts

During operations beat-note like artefacts in the spectrograms of OMS parameters were observed. They appear at the high frequencies close to the Nyquist frequency (simulated example in Figure 6.35).

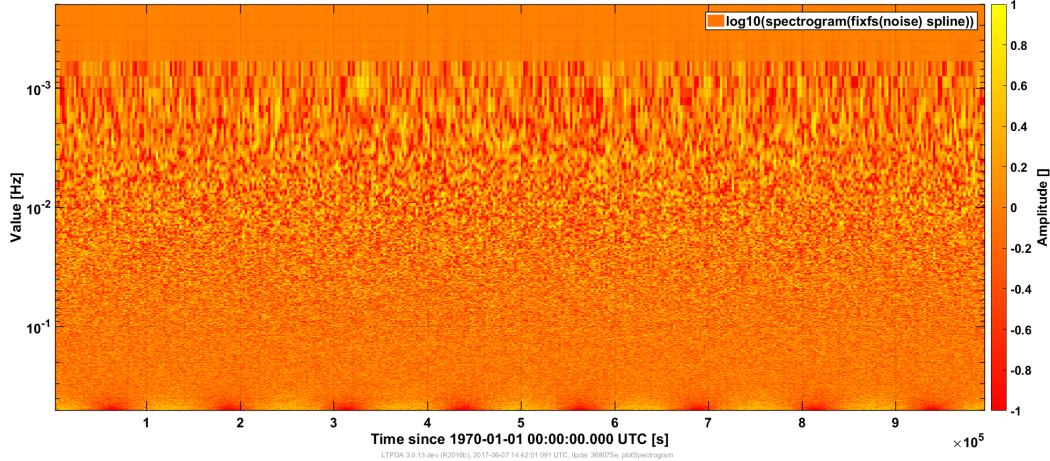


Figure 6.35.: Simulated noise with a sampling frequency close to 1 Hz. It was then preprocessed to 1 Hz using the standard fixfs method with spline interpolation. Note the beat-note like structure at the bottom.

The problem here is that the DMU clock at which the samples were acquired runs at a slightly different frequency than the official UTC clock on ground. That results in different timestamps for a 1 Hz parameter as illustrated in Figure 6.36 (exaggerated).

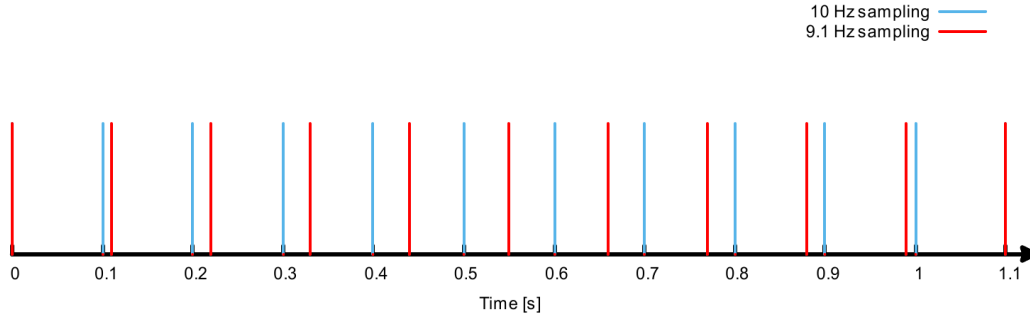


Figure 6.36.: The time grid of two different sampling frequencies.

One can see that the timestamps of the samples from both sampling frequencies are sometimes overlapping and sometimes are far apart.

Figure 6.37 shows the sampling of a 3 Hz sine wave. This is an example of a parameter received from LPF. For linear interpolation it can be seen that any resampling of this sampled sine wave will produce new samples with lower amplitudes than the maximum of the two surrounding old samples. The effect is least dominant if the new sample time is close to the old sample with the maximum value. As shown in Figure 6.36 the new sample time will be close to the old sample time at the start. Then, as the clocks drift the sample times will

drift apart and later approach each other again.

This was simulated with white noise and a clock that is 8 ppm off the 1 Hz clock (Figure 6.35). The amplitude maxima close to the Nyquist frequency appear about every 120000 seconds as expected.

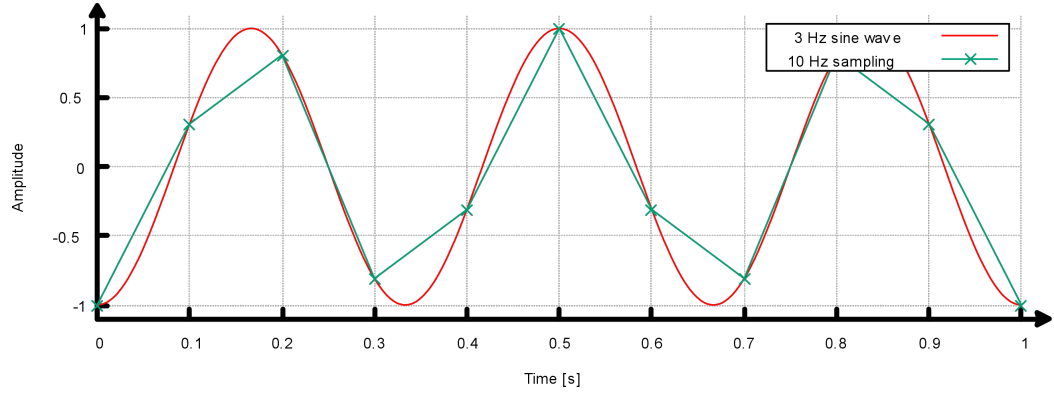


Figure 6.37.: 10 Hz sampling of a 3 Hz sine wave.

It could be seen that the affected frequency range (x .. Nyquist frequency) is larger for linear interpolation (Figure 6.38) than for the spline interpolation that is the standard for LTPDA preprocessing.

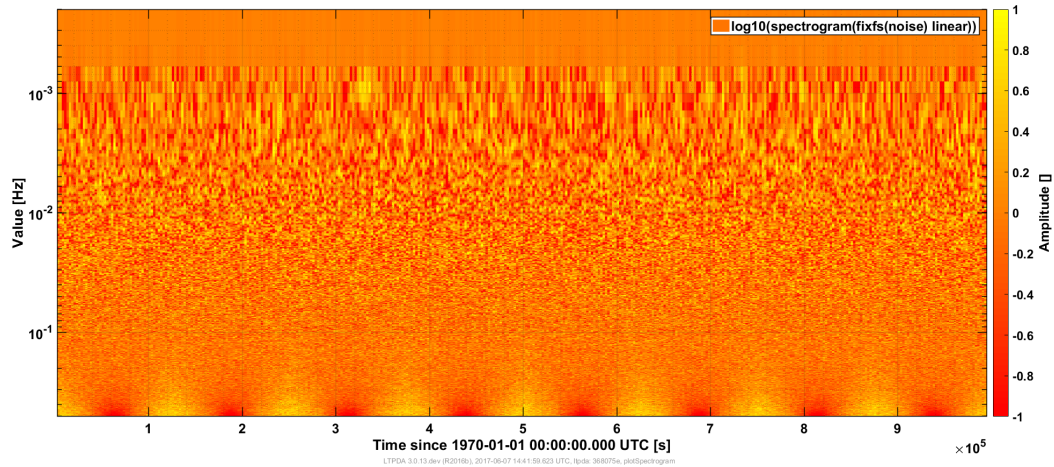


Figure 6.38.: Simulated noise with a sampling frequency close to 1 Hz. It was then pre-processed to 1 Hz using the fixfs method with linear interpolation. Note: the beat-note like structure at the bottom reaches lower frequencies compared to the spline interpolated data.

Therefore, when comparing signal amplitudes close to the Nyquist frequency one should not preprocess the data or use the nearest neighbour interpolation.

6.11. Longterm monitoring of PD sensitivity and TM reflectivity

6.11.1. Introduction

The active surface of a PD is sensitive to cosmic rays. An increase of dark current and a decrease in sensitivity is the consequence of radiation induced displacement damage and ionisation.

On LPF the shielding protects the PDs in the OMS to a great extend of cosmic radiation damage. However monitoring the PD sensitivity during mission is important to ensure their functionality for a LISA like lifetime.

Since every power measurement in the OMS is dependent of its particular PD, it is impossible to derive the PD efficiencies from its own power measurements. To calibrate the PDs and monitor their efficiencies over the mission duration a reference measurement of the beam power without a PD is necessary. On LPF we can use the relative acceleration of the TMs induced by a radiation pressure modulation to calibrate the power hitting the TMs.

For the calculation of the applied force by radiation pressure, the reflectivity of the TMs need to be known. Therefore a measurement of the TM reflectivity and in particular its changes over the mission duration are crucial.

6.11.2. TM reflectivity measurement

Experimental planning

For the estimation of the TM reflectivity the optical properties (reflectivity, transmissivity and absorption) of the beamsplitters and mirrors on the OB are assumed to stay constant over the mission duration. Hence the optical bench reduces to

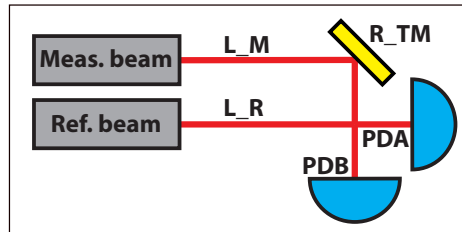


Figure 6.39.: OB measurements, assuming constant L_i

$$\Sigma_{ij} = 0.5 \cdot (P_M \cdot L_{iM} \cdot R_i + P_R \cdot L_{iR}) \cdot E_{ij} \quad (6.43)$$

with power P in measurement and reference beam, reflectivity R , PD sensitivity E and a constant term L_i regarding the losses in measurement and reference beam path of the corresponding interferometer (excluding the TM reflectivity and optical window transmittance). The indices correspond to:

$$\begin{Bmatrix} i \\ j \end{Bmatrix} = \begin{Bmatrix} R, F, 1, 12 \\ a, b \end{Bmatrix} \quad (6.44)$$

$$\begin{Bmatrix} R_r \\ R_f \\ R_{x1} \\ R_{x12} \end{Bmatrix} = \begin{Bmatrix} 1 \\ 1 \\ R_{TM1} \\ R_{TM1} \cdot R_{TM2} \end{Bmatrix} \quad (6.45)$$

$$(6.46)$$

R_{TM} is for real not only the TM reflectivity but the combination of TM reflectivity and optical window transmittance.

The TM reflectivity can then be deduced by an adequate combination of single beam power measurements, where the PD-sensitivity and therefore its changes over mission duration cancel.

$$\Sigma_i(P_M = 0) = 0.5 \cdot P_R \cdot L_{iR} \cdot E_i \quad (6.47)$$

$$\Sigma_i(P_R = 0) = 0.5 \cdot P_M \cdot L_{iM} \cdot R_i \cdot E_i \quad (6.48)$$

$$R_{TM1} = \frac{\Sigma_1(P_R = 0) \cdot \Sigma_R(P_M = 0)}{\Sigma_1(P_M = 0) \cdot \Sigma_R(P_R = 0)} \cdot \frac{L_{1R} \cdot L_{RM}}{L_{1M} \cdot L_{RR}} \quad (6.49)$$

$$R_{TM2} = \frac{\Sigma_{12}(P_R = 0) \cdot \Sigma_1(P_M = 0)}{\Sigma_{12}(P_M = 0) \cdot \Sigma_1(P_R = 0)} \cdot \frac{L_{12R} \cdot L_{1M}}{L_{12M} \cdot L_{1R}} \quad (6.50)$$

$$= \frac{\Sigma_{12}(P_R = 0) \cdot \Sigma_R(P_M = 0)}{\Sigma_{12}(P_M = 0) \cdot \Sigma_R(P_R = 0) \cdot R_{TM1}} \cdot \frac{L_{12R} \cdot L_{RM}}{L_{12M} \cdot L_{RR}} \quad (6.51)$$

Therefore the optical properties of the OB components need to be known in advance to compute the L_i s. The optical properties are known within an uncertainty of 0.49% for the beamsplitters and 0.24% for the mirrors. This gives an uncertainty for the measurement of R_{TM} of 2.62% for TM1 and 2.78% for TM2. This error is very high compared to the changes in reflectivity we want to measure.

But next to the measurement of the absolute value for the TM reflectivity, the change of this quantity between several measurements can be detected with much higher accuracy if we expect the L_i s to stay constant. Laser fluctuations cancel out by equation 6.49 to 6.51. The electronic readout of the channels has uncorrelated noise, which therefore does not cancel in the analysis.

So the uncertainty for the comparison between two measurements propagates to twice the uncertainty of the readout for Σ .

Hence we can measure the TM reflectivity changes over mission duration with high accuracy having an unknown offset of up to 2.78%.

Performed measurements

The beams were shut off one after another for about 4 Minutes minutes each. The DC-data of every PD-quadrant was then downloaded with 10 Hz for 1 minute each.

During nominal mission this measurement was performed 65 times . Figure 6.40 shows one of those measurements.

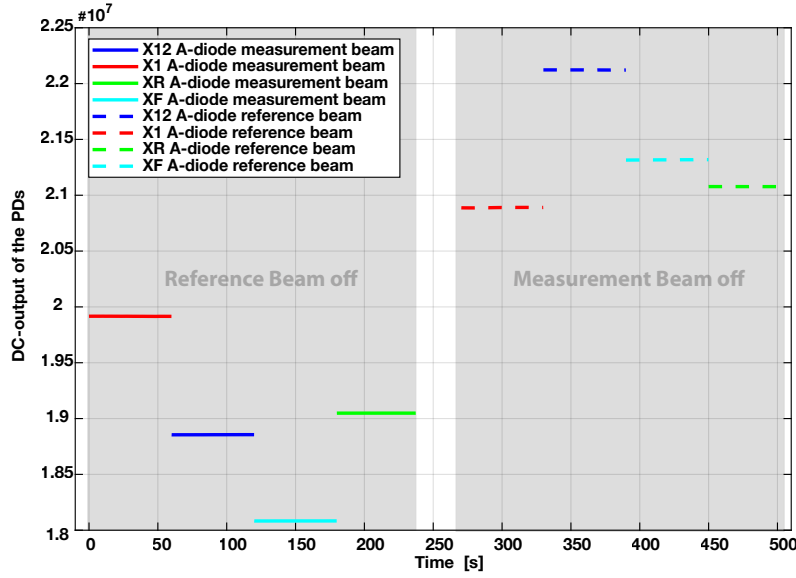


Figure 6.40.: Measurement of single beam powers on all QPDs. The beams are shut off one after another and the power on the single QPDs is downloaded with 10 Hz for 1 minute each.

The experiment was continued in the extensions period and the analysis is ongoing. Results will be published soon.

6.11.3. Photodiode sensitivity measurement

Experimental planning

The PD sensitivity E can be expressed as the ratio of measured power to the actually applied power to the PD:

$$P_{\text{meas}} = E \cdot P_{\text{real}} \quad (6.52)$$

The power hitting the TMs applies a constant force via photon pressure:

$$F_{\text{TM1}} + F_{\text{TM2}} = (1 + R_{\text{TM1}}) \cdot \frac{P_{\text{TM1}}}{c} + (1 + R_{\text{TM2}}) \cdot \frac{P_{\text{TM2}}}{c} \quad (6.53)$$

This force is compensated by the capacitive actuators with a DC force. A power modulation pushes the TMs more and less than nominal and hence leads to a back and forth TM displacement around its center at frequencies with low suspension control:

$$x_{\text{TM1}} + x_{\text{TM2}} = \left((1 + R_{\text{TM1}}) \cdot \frac{P_{\text{TM1}}}{m_{\text{TM1}}} + (1 + R_{\text{TM2}}) \cdot \frac{P_{\text{TM2}}}{m_{\text{TM2}}} \right) \cdot \frac{a_{\text{mod}}}{c \cdot (\omega_{\text{mod}}^2 - \omega_{\text{stiff}}^2)} \quad (6.54)$$

The measured displacement in the science interferometer is used to compute Δg and compensate for suspension control and stiffness.

With $P_{\text{TM1}} = 2 \cdot P_{\text{TM2}}$ we can compute the calibration factor c_{PD} between applied acceleration in Δg and measured power modulation in Σ

$$\Sigma(@ f_{\text{mod}}) = P_{\text{TM1}} \cdot \lambda \cdot a_{\text{mod}} \cdot c_{\text{PD}} \quad (6.55)$$

$$c_{\text{PDR}} = \frac{\Sigma(@ f_{\text{mod}}) \cdot \left(\frac{1+R_{\text{TM1}}}{c \cdot m_{\text{TM1}}} + \frac{1+R_{\text{TM2}}}{2 \cdot c \cdot m_{\text{TM2}}} \right)}{\Delta g(@ f_{\text{mod}})} \quad (6.56)$$

The factor λ corresponds to the ratio of power hitting the TM and power hitting the PDs.

With equation (6.52) and:

$$P_{\text{meas}} = \Sigma(@ f_{\text{mod}}) \quad \text{and} \quad P_{\text{real}} = P_{\text{TM1}} \cdot \lambda \cdot a_{\text{mod}} \quad (6.57)$$

we get the PD-sensitivity:

$$\rightarrow c_{\text{PD}} = E_{\text{PD}} \quad (6.58)$$

Performed measurements

On LPF we have the possibility to modulate the beam power individually for reference and measurement beam with the fast amplitude control loop. Since there is no possibility to add a time-varying signal to this analog loop, we need to change the set point.

Accordingly we modulate the beam power with a square wave and gain the harmonic frequencies by this.

Measurements for longterm monitoring:

The Experiment was performed twice during nominal mission on DOY 152/153 in 2016 and DOY 021 in 2017. This lets us compare the PD-sensitivity between beginning and end of the nominal mission.

- modulated beam: **measurement beam**
- modulation depth: 0.1 %
- modulation frequency: 1.67 mHz
- duration: 10000 seconds, giving a sufficient signal to noise ratio

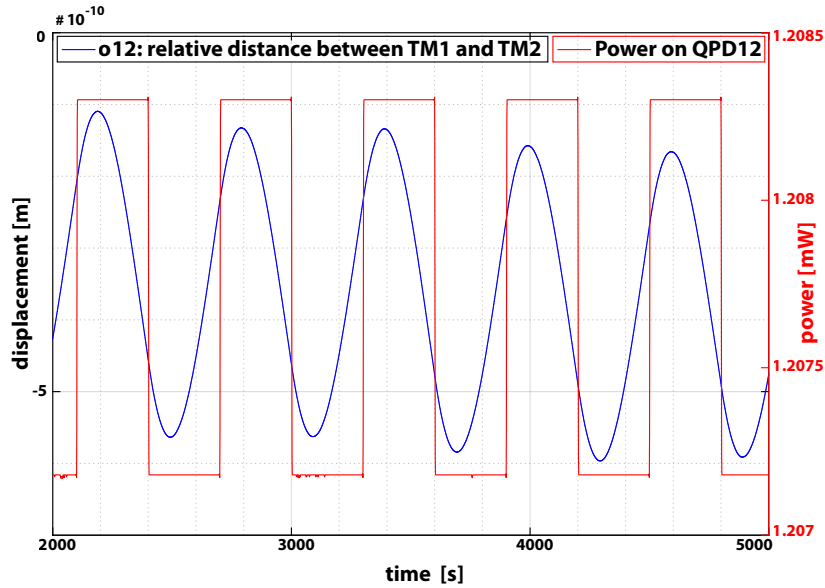


Figure 6.41.: Displacement of TM1 and TM2 due to power modulation of the measurement beam

Figure 6.41 shows a time-series of the modulation with power and displacement in the science interferometer.

Measurements for characterisation of the modulation:

For characterisation of the power modulation further experiments were performed on DOY 021.

The reference beam was modulated individual to investigate coupling of amplitude modulation to Δg .

Furthermore the reference and the measurement beam were modulated contrariwise to keep the sum of the beam powers constant and therefore get rid of temperature effects at the PD.

To look for nonlinearities the modulation depth was increased to 1 % and 2% for all three different modulations.

So the following measurements were made:

- modulated beam: **reference beam**
 - modulation depth : 0.1%, 1 % and 2 %
 - modulation frequency: 1.67 mHz
 - duration: 10000 seconds

- modulated beam: **measurement beam**
 - modulation depth : 0.1%, 1 % and 2 %
 - modulation frequency: 1.67 mHz
 - duration: 10000 seconds
- modulated beam: **measurement beam and reference beam, contrariwise**
 - modulation depth : 0.1%, 1 % and 2 %
 - modulation frequency: 1.67 mHz
 - duration: 10000 seconds

The analysis of the characterisation effects is further ongoing and results will be published soon.

6.12. Long term monitoring of LTP hardware

6.12.1. Introduction

The responsibility for equipment and on-board software monitoring as defined in [48]. This monitoring was undertaken during the In Orbit Operations Phase (IOOP), beginning after commissioning and spanning the LTP nominal operational phase, the DRS nominal operational phase, as well as extended operations. As such, the AEI was responsible for monitoring the systems provided by the DLR:

- The LTP System
- The Optical Metrology System, (excluding the Laser Modulator Unit, the Optical Bench Assembly, Phasemeter Assembly and Diagnostic Equipment)
- The Optical Metrology SCOE

Therefore, the AEI monitored the Laser Assembly (LA), consisting of the Reference Laser Unit (RLU) and the Laser Control Unit (LCU).

The telemetry from these subsystems was available at 0.2 Hz, and was in two forms, as continuous housekeeping data and as flags with a binary 0 or 1 value that defined whether system operation was nominal or non-nominal. For most of the continuous housekeeping telemetry, the parameters had defined nominal operational ranges, as well as high and low warning and critical levels. These values, and the conditions that defined the flag as being nominal or non-nominal, can be found in [49].

6.12.2. Monitored parameters

The ID, short name, description, and LTPDA name for each of the telemetry parameters monitored by the AEI are listed in Table 6.2, the LA hardware flag parameters are listed separately, in Table 6.3.



System ID	Short Name LTPDA Name	Description
LLT10001	RLU_Current_Bench	RLU laser diode current, for the laser diode bench in use.
LLT10002	RLU_OUTPUT_Pwr	Power of the laser head photodiode
LLT10003	RLU_TEMP	Temperature of the RLU
LLT10004	LA_SPARE_ANALOG_TM_LU2	Spare channel: Power of the laser head photodiode
LLT10005	RLA_P5V_REF_CAL_IF	Monitors the 5 V reference on the LA I/F
LLT10006	LA_NULLV_IF	Monitors the 0 V reference on the LA I/F
LLT10009	LA_PV15V	LA +15 V voltage HK, serving the RLU and LME
LLT10010	LA_PC15V	LA +15 V current HK, serving the RLU and LME
LLT10011	LA_NV15V	LA -15 V voltage HK, serving the RLU and LME
LLT10012	LA_NC15V	LA -15 V current HK, serving the RLU and LME
LLT10013	LA_PV5V	LA +5.1 V HK, serving the LME
LLT10014	LA_PC5V	LA +5.1 V current HK, serving the LME
LLT10017	LA_PWR_TEMP_1	Monitors the temperature of the PSUX (X = 1 or 2) at point 1
LLT10018	LA_PWR_TEMP_2	Monitors the temperature of the PSUX (X = 1 or 2) at point 2
LLT10019	LA_REF_4V_POW	Monitors the 4 V reference on the power supply
LLT10020	LA_REF_1V_POW	Monitors the 1 V reference on the power supply
LLT10021	LA_SPARE_ANALOG_TM_LU1	Monitors the laser head photo diode power
LLT10022	LA_FPGA_VERSION	Hard-coded FPGA version counter
LLT10023	LA_NULLV_POW	Monitors the 0 V reference on the power supply

Table 6.2.: An overview of the LA hardware telemetry parameters that will be monitored by the AEI.



System ID	Short Name	Bit Position	Description
LLT10024	LA_DIG_STAT_WRD	0	Error in previous command status
LLT10025	LM_Err_PRE_CMD		
LLT10026	LM_TIMEOUT_Err	1	Timeout error for previous command status
LLT10027	LM_CMD_INTPR_Err	2	Command interpreter error status
LLT10028	LM_ADC_LATCHUP_Err	3	HK ADC latch-up error status
LLT10029	LM_NEW_HK_DATA	4	New HK data status
LLT10030	LM_FHET_ACTIVE	5	Heterodyne freq. redundant or active status
LLT10031	LM_SUM_DIFF_LOOP_STAT	6	Sum loop and difference loop locked status
LLT10032	LM_HV_POW_STAT	7	HV supply working status
LLT10033	LA_POW_STAT	8	Nominal or redundant power supply on
LLT10035	LA_TM_COUNT_2Bit	9 to 10	Counter
LLT10036	LA_SPARE_DIGITAL_TM_LU2	11	Spare
LLT10037	LA_SPARE_DIGITAL_TM_LU1	12	Spare
LLT10038	RLU_XTAL_TEMP_OK	13	Laser X-tal temp. status
LLT10039	RLU_ON_OK	14	Status of nominal optical output power
LLT10040	LA_HK_VALID	15	HK packet status

Table 6.3.: An overview of the LA hardware telemetry flags that will be monitored by the AEI.

6.12.3. The monitoring activities

Prior to launch, the monitoring activities were defined in the AEI monitoring plan [50] as being:

- To observe the housekeeping telemetry, including flags, from the LA subsystems as defined in Tables 6.2 and 6.3.
- To identify anomalies in the parameters (see Figure 6.42) and to provide analysis and correction support to the STOC and MOC as appropriate, and within one working day.
- To produce monitoring reports on a daily, weekly and monthly basis, in addition to a longterm overview for the full duration of the mission.
- To prepare the analysis scripts and software required for these activities, in advance of launch.

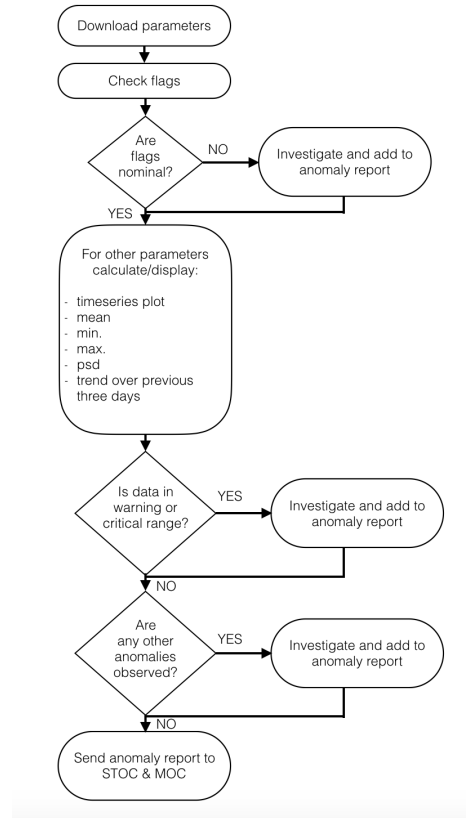


Figure 6.42.: A flowchart illustrating the LA hardware monitoring procedure [50].

To meet these requirements MATLAB scripts and functions were developed that:

- Downloaded the telemetry in a defined timespan from the housekeeping data repository.
- Calculated the minimum, maximum and mean values for that timespan.
- Produced plots of the timeseries, trend and a spectrum (with a reference spectrum for comparison).
- Identified whether the parameter was within the nominal range, the upper or lower warning range, or the upper or lower critical range. If the parameter was in either the warning or critical range, then the time at which that occurred was also output.
- Output whether the flags were nominal or non-nominal.
- Compiled all of the above into an automatically generated html report.

Initially, daily reports were produced locally at the AEI by running the scripts manually. The reports were checked, and the findings recorded in a separate document, one for each mission day. This was time consuming, and was therefore incorporated into an online reporting tool run by the IEEC in Barcelona. With this tool, the daily monitoring script



was run automatically, and the output report was made available to the full collaboration via a password protected webpage. The hardware monitoring team at the AEI could then monitor the LA subsystem more easily, and the full collaboration were able to easily check the status of the LA subsystem, in addition to the subsystems being monitored by other institutions. In this way, the manual daily reporting requirement was removed. Where any anomaly was observed, then a manual analysis was performed. This involved using the LPF telecommand software to check whether the anomaly occurred as a result of a commanded action on the satellite.

Scripts to produce the plots and outputs for the monthly monitoring were run by hand throughout the mission, and the results were logged in one document. This substantial document provides a progressive month-by-month view of the system operation for the duration of the mission.

6.12.4. Results

In general, the LA hardware functioned well throughout the duration of the mission. Analysis of the data, and the reporting of the full mission overview, is ongoing [49].

Acknowledgements

This work has been made possible by the LISA Pathfinder mission, which is part of the space-science program of the European Space Agency. We acknowledge the support of the German Space Agency, DLR. The work is supported by the Federal Ministry for Economic Affairs and Energy based on a resolution of the German Bundestag (FKZ 50OQ0501 and FKZ 50OQ1601). The following industries have supplied an excellent hardware under this grant: Airbus DS GmbH in Friedrichshafen, OHB-System AG in Munich (previously Kayser-Threde GmbH) and TESAT Spacecom GmbH & Co. KG in Backnang. We also would like to thank all participating and supportive agencies, institutes and companies all over Europe, as well as the US contribution of the Disturbance Reduction System.

List of Figures

2.1.	LPFsatt	6
2.2.	LPF coordinates	6
2.3.	LPF coordinates	7
2.4.	OMS block diagram	8
2.5.	The four interferometers on the OB shown separately. TM1 is above the top and TM2 below the bottom of each picture. Top left: x_1 , top right: x_{12} , bottom left: Reference and bottom right: Frequency.	9
2.6.	A flow chart depicting the signal processing in the DMU [2] [3] [4].	10
3.1.	A schematic view of the data flow and responsibilities and interactions between STOC, MOC and the scientists.	16
4.1.	A view of the main web interface of one of the operational LTPDA repositories, showing the large number of databases populated and used throughout mission development and operations.	19
4.2.	Commits to the LTPDA git repository per month over the course of the development of LTPDA.	20
4.3.	Lines of code in LTPDA over the course of the development.	21
4.4.	The number of commits to the LTPDA git repository grouped by institution.	21
5.1.	An flowdiagram of one of the pipelines used during science operations. This particular pipeline describes the analysis needed to estimate the charge on each test mass having performed the associated investigations on-board. . . .	25
5.2.	A process flow of the steps needed to go from a conceptual physical experiment through a series of investigations executed on the satellite and finally to the data analysis results. Each of the boxes represents a Pipeline Step, and all flows shown in the diagram can be executed via dedicated driver scripts. . . .	26
5.3.	A schematic view of the steps needed to validate an experiment from concept to execution.	27
5.4.	A calendar view of the nominal operations phase showing the breakdown of the time into classes of investigation.	28
5.5.	A schematic of the interactions and activities testing in STOC Simulation 1. . .	32
6.1.	System identification experiments during nominal mission operations	37
6.2.	Batteries of injections during the system identification experiment.	38
6.3.	(a): Result taken from [1], showing that the bulge at 200-20 mHz can be subtracted. (b) In this figure, no subtraction was performed. Instead the reduction was achieved by a realignment of the test masses prior to the second noise run. ²	40



6.4.	Injection of common mode motion of both test masses in y-direction. The raw differential readout $o12$ shown in black comprises an oscillation caused by cross coupling of the injected lateral motion.	43
6.5.	Injection of a differential motion of both test masses in y-direction. The raw differential readout $o12$ shown in black comprises a strong oscillation caused by cross coupling of the injected motion.	43
6.6.	Example of $z_{1,2}$ injections performed during the engineering days cross-talk experiment performed on 2016-March-16. The labels ‘GRS $z_{1,2}$ ’ indicate, that the shown vertical test mass displacement (z_1, z_2) is taken from the Gravitational Reference Sensor readout. This figure has been previously published in [22].	44
6.7.	Example for drift mode data.	47
6.8.	Drift Mode windowing approach: the window goes to zero during the kick. . .	49
6.9.	The time series of OMS measurement of $o1$ (red) and $o12$ (purple), and the guidance injection into DFACS on the x axis of TM1 (blue) and TM2 (green). The motion measured in $o12$ is the result of the simultaneous movement of TM1 and TM2, both test masses move in the same x direction initially. . . .	50
6.10.	The time series of the injection in $\eta1$, performed on DOY049. Plotted is the injected signal (green), and the measured value of DWS (blue) and DC (red). .	51
6.11.	The time series of the injection in $\phi1$, performed on DOY049. Plotted is the injected signal (green), and the measured value of DWS (blue) and DC (red).t	52
6.12.	The time series of the injection in $\eta2$, performed on DOY050. Plotted is the injected signal (green), and the measured value of DWS (blue) and DC (red). .	52
6.13.	The time series of the injection in $\phi2$, performed on DOY050. Plotted is the injected signal (green), and the measured value of DWS (blue) and DC (red). .	53
6.14.	The correlation between GRS injection and DWS measurement of $\eta1$, after the DWS is calibrated.	54
6.15.	The correlation between GRS injection and DWS measurement of $\phi1$, after the DWS is calibrated.	54
6.16.	The contrast of $o1$, plotted over the angular displacement of $\eta1$ measured by the OMS and GRS, after the calibration. The difference between the different measurement schemes for bigger test mass offsets is easily visible.	55
6.17.	The contrast of $o1$, plotted over the angular displacement of $\phi1$ measured by the OMS and GRS, after the calibration.	56
6.18.	The contrast of $o12$, plotted over the angular displacement of $\eta1$ measured by the OMS and GRS, after the calibration.	56
6.19.	The contrast of $o12$, plotted over the angular displacement of $\phi1$ measured by the OMS and GRS, after the calibration.	57
6.20.	The contrast of $o12$, plotted over the angular displacement of $\eta2$ measured by the OMS and GRS, after the calibration.	57
6.21.	The contrast of $o12$, plotted over the angular displacement of $\phi2$ measured by the OMS and GRS, after the calibration.	58
6.22.	Calibration between GRS and DWS in the DWS step experiment	59



6.23. The concept of the arm length mismatch experiment. The black trace (corresponding to the left y -axis) shows the laser frequency noise measurement. The two sets of two injections are clearly discernible. The DC value of the signal is at a lower level during the open-loop measurement. The distance between the two test masses is shown in red (refer to right y -axis). The second set of modulations is taking place at the offset position. Some transients are discernible.	61
6.24. The time series of the first step experiment, plotted in blue. At each step we select a quiet timespan, shown in red, and calculate average the noise level. The uncertainty on the test mass position comes from the drift during each step, the error is small compared to the range of test mass offsets.	65
6.25. Example spectra for test mass offsets between 0 nm and 120 nm, the spectra were calculated with 300 samples in each fft with an overlap of 50% and an Hanning window. The rise in noise for offsets towards a phase difference of π between the measurement and reference signal is visible, for the later analysis the average noise was calculated in the band between 0.55 Hz and 0.9 Hz. The analysis for higher frequencies is still ongoing.	66
6.26. An example step of the second step experiment. The timespan where balanced detection is on is shown in red, the shorter timespan in red is recorded at 100 Hz. Balanced detection is off in the green segments, again the shorter timespan is recorded at 100 Hz.	67
6.27. The spectra were calculated with 700 samples in each fft with an overlap of 50% and BH92 window. In red is the measurement with balanced detection on, both 10 Hz data and 100 Hz data. Shown in green is the measurement with balanced detection off, also with 10 Hz and 100 Hz. The peaks visible for in the single side spectra are normally suppressed by balanced detection. . . .	67
6.28. DWS principle	69
6.29. DWS noise performance	72
6.30. DWS noise performance at alignments	74
6.31. Parameter space during the first DWS step experiment	75
6.32. Timeseries of the DWS step experiment	76
6.33. Parameter space during the DWS step experiment	76
6.34. The cycle counter is incremented at 100 Hz. When it reaches 10 it is set back to 0 and an averaged 10 Hz sample is computed from the last 10 samples. The 1 PPS signal from the OBC is used for synchronisation. The grey area marks the time when the 1 PPS signal is expected to occur.	78
6.35. Simulated noise with a sampling frequency close to 1 Hz. It was then preprocessed to 1 Hz using the standard fixfs method with spline interpolation. Note the beat-note like structure at the bottom.	81
6.36. The time grid of two different sampling frequencies.	81
6.37. 10 Hz sampling of a 3 Hz sine wave.	82
6.38. Simulated noise with a sampling frequency close to 1 Hz. It was then preprocessed to 1 Hz using the fixfs method with linear interpolation. Note: the beat-note like structure at the bottom reaches lower frequencies compared to the spline interpolated data.	82
6.39. OB measurements, assuming constant L_i	83



6.40. Measurement of single beam powers on all QPDs. The beams are shut off one after another and the power on the single QPDs is downloaded with 10 Hz for 1 minute each.	85
6.41. Displacement of TM1 and TM2 due to power modulation of the measurement beam	87
6.42. LAMonflow	91

List of Tables

6.1.	DWS calibration performance	73
6.2.	An overview of the LA hardware telemetry parameters that will be monitored by the AEI.	89
6.3.	An overview of the LA hardware telemetry flags that will be monitored by the AEI.	90

Bibliography

- [1] M. Armano, H. Audley, G. Auger, J. T. Baird, M. Bassan, P. Binetruy, M. Born, D. Bortoluzzi, N. Brandt, M. Caleno, L. Carbone, A. Cavalleri, A. Cesarini, G. Ciani, G. Congedo, A. M. Cruise, K. Danzmann, M. de Deus Silva, R. De Rosa, M. Diaz-Aguiló, L. Di Fiore, I. Diepholz, G. Dixon, R. Dolesi, N. Dunbar, L. Ferraioli, V. Ferroni, W. Fichter, E. D. Fitzsimons, R. Flatscher, M. Freschi, A. F. García Marín, C. García Marirrodiga, R. Gerndt, L. Gesa, F. Gibert, D. Giardini, R. Giusteri, F. Guzmán, A. Grado, C. Grimaldi, A. Grynagier, J. Grzysch, I. Harrison, G. Heinzel, M. Hewitson, D. Hollington, D. Hoyland, M. Hueller, H. Inchauspé, O. Jennrich, P. Jetzer, U. Johann, B. Johlander, N. Karnesis, B. Kaune, N. Korsakova, C. J. Killow, J. A. Lobo, I. Lloro, L. Liu, J. P. López-Zaragoza, R. Maarschalkerweerd, D. Mance, V. Martín, L. Martin-Polo, J. Martino, F. Martin-Porqueras, S. Madden, I. Mateos, P. W. McNamara, J. Mendes, L. Mendes, A. Monsky, D. Nicolodi, M. Nofrarias, S. Paczkowski, M. Perreut-Lloyd, A. Petiteau, P. Pivato, E. Plagnol, P. Prat, U. Ragnit, B. Raïs, J. Ramos-Castro, J. Reiche, D. I. Robertson, H. Rozemeijer, F. Rivas, G. Russano, J. Sanjuán, P. Sarra, A. Schleicher, D. Shaul, J. Slutsky, C. F. Sopuerta, R. Stanga, F. Steier, T. Sumner, D. Texier, J. I. Thorpe, C. Trenkel, M. Tröbs, H. B. Tu, D. Vetrugno, S. Vitale, V. Wand, G. Wanner, H. Ward, C. Warren, P. J. Wass, D. Wealthy, W. J. Weber, L. Wissel, A. Wittchen, A. Zambotti, C. Zanon, T. Ziegler, and P. Zweifel. Sub-Femto-g Free Fall for Space-Based Gravitational Wave Observatories: LISA Pathfinder Results. *Physical Review Letters*, 116(23):231101, June 2016.
- [2] H. E. Audley. *Preparing for LISA Pathfinder Operations: characterisation of the optical metrology system*. PhD thesis, Leibniz Universität Hannover, 2014.
- [3] R. Wegener, R. Gerndt, N. Gradmann, and D. Kolbe. LTP user manual. Technical Report S2-ASD-MA-3004_LTP, ASD, 2014.
- [4] U. Denskat, R. Gerndt, G. Link, and U. Johann. Phasemeter processing and laser control. Technical Report S2-ASD-RS-3018, ASD, September 2009.
- [5] Michael Tröbs. Test plan for LTP reference laser unit EM characterization at AEI. S2-AEI-TN-3029, Issue 1, Revision 5, 2006.
- [6] LISA Project. LTP Requirement Specification cw1-Heine-comments-2006-01-31. Draft A, 2006.
- [7] Technical drawing of the LTP PFM RLU. 63.7395.400.00MB, 2005.
- [8] Michael Tröbs. LTP reference laser unit engineering model characterization. S2-AEI-TN-3032, Issue 1, Revision 1, 2006.
- [9] Reference Laser Unit Requirements Specification. S2-ASD-RS-3021, 2006.



- [10] G. Heinzel, V. Wand, A. Garcia, O. Jennrich, C. Braxmaier, D. Robertson, K. Middleton, D. Hoyland, A. Rüdiger, R. Schilling, U. Johann, and K. Danzmann. The LTP interferometer and phasemeter. *Class. Quantum Grav.*, 21:S581–S587, 2004.
- [11] Michael Tröbs and Gerhard Heinzel. Improved spectrum estimation from digitized time series on a logarithmic frequency axis. *Measurement*, 39(2):120 – 129, 2006.
- [12] Michael Tröbs and Gerhard Heinzel. Corrigendum to "Improved spectrum estimation from digitized time series on a logarithmic frequency axis" [Measurement 39 (2006) 120-129]. *Measurement*, 42(1):170, 2009.
- [13] Gerhard Heinzel. Generation of Random time series with prescribed spectra. S2-AEI-TN-3034, Draft 0.2, 2006.
- [14] M Hewitson, M Armano, M Benedetti, J Bogenstahl, D Bortoluzzi, P Bosetti, N Brandt, A Cavalleri, G Ciani, I Cristofolini, M Cruise, K Danzmann, I Diepholz, R Dolesi, J Fauste, L Ferraioli, D Fertin, W Fichter, A García, C García, A Grynagier, F Guzmán, E Fitzsimons, G Heinzel, D Hollington, J Hough, M Hueller, D Hoyland, O Jennrich, B Johlander, C Killow, A Lobo, D Mance, I Mateos, P W McNamara, A Monsky, D Nicolini, D Nicolodi, M Nofrarias, M Perreux-Lloyd, E Plagnol, G D Racca, J Ramos-Castro, D Robertson, J Sanjuan, M O Schulte, D N A Shaul, M Smit, L Stagnaro, F Steier, T J Sumner, N Tateo, D Tombolato, G Vischer, S Vitale, G Wanner, H Ward, S Waschke, V Wand, P Wass, W J Weber, T Ziegler, and P Zweifel. Data analysis for the lisa technology package. *Classical and Quantum Gravity*, 26(9):094003, 2009.
- [15] F Antonucci, M Armano, H Audley, G Auger, M Benedetti, P Binetruy, C Boatella, J Bogenstahl, D Bortoluzzi, P Bosetti, M Caleno, A Cavalleri, M Cesa, M Chmeissani, G Ciani, A Conchillo, G Congedo, I Cristofolini, M Cruise, K Danzmann, F De Marchi, M Diaz-Aguilo, I Diepholz, G Dixon, R Dolesi, J Fauste, L Ferraioli, D Fertin, W Fichter, E Fitzsimons, M Freschi, A García Marin, C García Marirrodiga, L Gesa, D Giardini, C Grimaldi, A Grynagier, B Guillaume, F Guzmán, I Harrison, G Heinzel, M Hewitson, D Hollington, J Hough, D Hoyland, M Hueller, J Huesler, O Jeannin, O Jennrich, P Jetzer, B Johlander, C Killow, X Llamas, I Lloro, A Lobo, R Maarschalkerweerd, S Madden, D Mance, I Mateos, P W McNamara, J Mendes, E Mitchell, A Monsky, D Nicolini, D Nicolodi, M Nofrarias, F Pedersen, M Perreux-Lloyd, A Perreca, E Plagnol, P Prat, G D Racca, B Rais, J Ramos-Castro, J Reiche, J A Romera Perez, D Robertson, H Rozemeijer, J Sanjuan, M Schulte, D Shaul, L Stagnaro, S Strandmoe, F Steier, T J Sumner, A Taylor, D Texier, C Trenkel, D Tombolato, S Vitale, G Wanner, H Ward, S Waschke, P Wass, W J Weber, and P Zweifel. Lisa pathfinder data analysis. *Classical and Quantum Gravity*, 28(9):094006, 2011.
- [16] A Monsky, M Hewitson, L Ferraioli, G Wanner, M Nofrarias, M Hueller, I Diepholz, A Grynagier, M Armano, M Benedetti, J Bogenstahl, D Bortoluzzi, P Bosetti, N Brandt, A Cavalleri, G Ciani, I Cristofolini, M Cruise, K Danzmann, R Dolesi, J Fauste, D Fertin, W Fichter, A García, C García, F Guzmán, E Fitzsimons, G Heinzel, D Hollington, J Hough, D Hoyland, O Jennrich, B Johlander, C Killow, A Lobo, D Mance, I Mateos, P W McNamara, D Nicolini, D Nicolodi, M Perreux-Lloyd, E Plagnol, G D Racca, J Ramos-Castro, D Robertson, J Sanjuan, M O Schulte, D N A Shaul, M Smit,



- L Stagnaro, F Steier, T J Sumner, N Tateo, D Tombolato, G Vischer, S Vitale, H Ward, S Waschke, P Wass, W J Weber, T Ziegler, and P Zweifel. The first mock data challenge for lisa pathfinder. *Classical and Quantum Gravity*, 26(9):094004, 2009.
- [17] M Nofrarias, L Ferraioli, G Congedo, M Hueller, M Armano, M Diaz-Aguiló, A Grynagier, M Hewitson, and S Vitale. Parameter estimation in lisa pathfinder operational exercises. *Journal of Physics: Conference Series*, 363(1):012053, 2012.
 - [18] Daniele Vetrugno, Nikolaos Karnesis, and on behalf of the LPF collaboration. Calibrating lisa pathfinder raw data into femto-g differential accelerometry. *Journal of Physics: Conference Series*, 840(1):012002, 2017.
 - [19] Stefano Vitale, Giuseppe Congedo, Rita Dolesi, Valerio Ferroni, Mauro Hueller, Daniele Vetrugno, William Joseph Weber, Heather Audley, Karsten Danzmann, Ingo Diepholz, Martin Hewitson, Natalia Korsakova, Luigi Ferraioli, Ferran Gibert, Nikolaos Karnesis, Miquel Nofrarias, Henri Inchauspe, Eric Plagnol, Oliver Jennrich, Paul W. McNamara, Michele Armano, James Ira Thorpe, and Peter Wass. Data series subtraction with unknown and unmodeled background noise. *Phys. Rev. D*, 90:042003, Aug 2014.
 - [20] M. Nofrarias, C. Röver, M. Hewitson, A. Monsky, G. Heinzl, K. Danzmann, L. Ferraioli, M. Hueller, and S. Vitale. Bayesian parameter estimation in the second lisa pathfinder mock data challenge. *Phys. Rev. D*, 82:122002, Dec 2010.
 - [21] Christian Röver. Student- t based filter for robust signal detection. *Phys. Rev. D*, 84:122004, Dec 2011.
 - [22] Gudrun Wanner, Nikolaos Karnesis, and LISA Pathfinder collaboration. Preliminary results on the suppression of sensing cross-talk in lisa pathfinder. *Journal of Physics: Conference Series*, 840(1):012043, 2017.
 - [23] F Antonucci, M Armano, H Audley, G Auger, M Benedetti, P Binetruy, J Bogenstahl, D Bortoluzzi, P Bosetti, N Brandt, M Caleno, P Cañizares, A Cavalleri, M Cesa, M Chmeissani, A Conchillo, G Congedo, I Cristofolini, M Cruise, K Danzmann, F De Marchi, M Diaz-Aguilo, I Diepholz, G Dixon, R Dolesi, N Dunbar, J Fauste, L Ferraioli, V Ferrone, W Fichter, E Fitzsimons, M Freschi, A García Marin, C García Marirrodiga, R Gerndt, L Gesa, F Gilbert, D Giardini, C Grimaldi, A Grynagier, B Guillaume, F Guzmán, I Harrison, G Heinzl, V Hernández, M Hewitson, D Hollington, J Hough, D Hoyland, M Hueller, J Huesler, O Jennrich, P Jetzer, B Johlander, N Karnesis, C Killow, X Llamas, I Lloro, A Lobo, R Maarschalkerweerd, S Madden, D Mance, I Mateos, P W McNamara, J Mendes, E Mitchell, A Monsky, D Nicolini, D Nicolodi, M Nofrarias, F Pedersen, M Perreux-Lloyd, E Plagnol, P Prat, G D Racca, J Ramos-Castro, J Reiche, J A Romera Perez, D Robertson, H Rozemeijer, J Sanjuan, A Schleicher, M Schulte, D Shaul, L Stagnaro, S Strandmoe, F Steier, T J Sumner, A Taylor, D Texier, C Trenkel, H-B Tu, S Vitale, G Wanner, H Ward, S Waschke, P Wass, W J Weber, T Ziegler, and P Zweifel. The LISA Pathfinder mission. *Classical and Quantum Gravity*, 29(12):124014, 2012.
 - [24] F Antonucci, M Armano, H Audley, G Auger, M Benedetti, P Binetruy, C Boatella, J Bogenstahl, D Bortoluzzi, P Bosetti, N Brandt, M Caleno, A Cavalleri, M Cesa,

- M Chmeissani, G Ciani, A Conchillo, G Congedo, I Cristofolini, M Cruise, K Danzmann, F De Marchi, M Diaz-Aguilo, I Diepholz, G Dixon, R Dolesi, N Dunbar, J Fauste, L Ferraioli, D Fertin, W Fichter, E Fitzsimons, M Freschi, A García Marin, C García Marirrodriga, R Gerndt, L Gesa, D Giardini, F Gibert, C Grimani, A Grynagier, B Guillaume, F Guzmán, I Harrison, G Heinzl, M Hewitson, D Hollington, J Hough, D Hoyland, M Hueller, J Huesler, O Jeannin, O Jennrich, P Jetzer, B Johlander, C Killow, X Llamas, I Lloro, A Lobo, R Maarschalkerweerd, S Madden, D Mance, I Mateos, P W McNamara, J Mendes, E Mitchell, A Monsky, D Nicolini, D Nicolodi, M Nofrarias, F Pedersen, M Perreux-Lloyd, A Perreca, E Plagnol, P Prat, G D Racca, B Rais, J Ramos-Castro, J Reiche, J A Romera Perez, D Robertson, H Rozemeijer, J Sanjuan, A Schleicher, M Schulte, D Shaul, L Stagnaro, S Strandmoe, F Steier, T J Sumner, A Taylor, D Texier, C Trenkel, D Tombolato, S Vitale, G Wanner, H Ward, S Waschke, P Wass, W J Weber, and P Zweifel. From laboratory experiments to LISA Pathfinder: achieving LISA geodesic motion. *Classical and Quantum Gravity*, 28(9):094002, 2011.
- [25] R. Giusteri for the LPF collaboration. The free-fall mode experiment on LISA Pathfinder: first results. In *Journal of Physics Conference Series*, volume 840 of *Journal of Physics Conference Series*, page 012005, May 2017.
- [26] A. Schleicher. DFACS requirement specifications - S2-ASD-RS-2001. Technical report, Astrium, 2013.
- [27] M Armano, H Audley, G Auger, J Baird, P Binetruy, M Born, D Bortoluzzi, N Brandt, A Bursi, M Caleno, et al. Free-flight experiments in LISA Pathfinder. In *Journal of Physics: Conference Series*, volume 610, page 012006. IOP Publishing, 2015.
- [28] A. Grynagier. The Drift Mode for LISA Pathfinder. Technical report, Institute of Flight Mechanics and Flight Control, Universität Stuttgart, 2009.
- [29] A. Schleicher. DFACS External ICD. Technical report, Astrium, 2012.
- [30] A. Grynagier, W. Fichter, and S. Vitale. The LISA Pathfinder drift mode: implementation solutions for a robust algorithm. *Classical and Quantum Gravity*, 26(9):094007, May 2009.
- [31] G. Russano. A torsion pendulum ground test of the LISA Pathfinder Free-fall mode. *ArXiv e-prints*, August 2016.
- [32] G Russano, A Cavalleri, A Cesarini, R Dolesi, V Ferroni, F Gibert, R Giusteri, M Hueller, L Liu, P Pivato, H B Tu, D Vetrugno, S Vitale, and W J Weber. Measuring fN force variations in presence of constant nN forces: a torsion pendulum ground test of LISA Pathfinder free fall mode. submitted.
- [33] A. Grynagier. The Drift Mode Data Analysis Method for parameteric and Spectral estimation. Technical report, Institute of Flight Mechanics and Flight Control, Universität Stuttgart, 2010.
- [34] Gerhard Heinzl. SMART-2 interferometer - S2-AEI-TN-3010. Technical report, AEI Hannover, 2002.



- [35] D. Robertson. 3OB As Built OptoCAD Model - S2-UGL-TN-3045. Technical report, University of Glasgow, 2013.
- [36] Sarah Paczkowski on behalf of the LPF collaboration. Laser Frequency Noise Stabilisation and Interferometer Path Length Differences on LISA Pathfinder. *Journal of Physics: Conference Series*, 840(1):012004, 2017.
- [37] Michael Kersten. OMS- control loop stability analysis and filter design - S2-ASD-TN-3107. Technical report, Astrium, 2011.
- [38] Michael Born and LPF collaboration. LISA Pathfinder: OPD loop characterisation. *Journal of Physics: Conference Series*, 840(1):012036, 2017.
- [39] Euan Morrison, Brian J. Meers, David I. Robertson, and Henry Ward. Automatic alignment of optical interferometers. *Appl. Opt.*, 33(22):5041–5049, Aug 1994.
- [40] Hartmut Grote, Gerhard Heinzel, Andreas Freise, Stefan Goßler, Benno Willke, Harald Lück, Harry Ward, Morag M. Casey, Kenneth A. Strain, David Robertson, Jim Hough, and Karsten Danzmann. Automatic beam alignment for the mode-cleaner cavities of geo 600. *Appl. Opt.*, 43(9):1938–1945, Mar 2004.
- [41] Xiangzhi Yu, S R Gillmer, and J D Ellis. Beam geometry, alignment, and wavefront aberration effects on interferometric differential wavefront sensing. *Measurement Science and Technology*, 26(12):125203, 2015.
- [42] E. Fitzsimons. Optical characterisation of 3ob. Technical note S2-UGL-TN-3039, University of Glasgow, 2013.
- [43] Lennart Wissel. In-orbit performance and behaviour of the LISA Pathfinder Optical Metrology System. Master’s thesis, Leibniz Universität Hannover, 2017.
- [44] Lennart Wissel and LPF collaboration. Lisa pathfinder: Understanding dws noise performance for the lisa mission. *Journal of Physics: Conference Series*, 840(1):012044, 2017.
- [45] M. Armano, H. Audley, G. Auger, J. T. Baird, M. Bassan, P. Binetruy, M. Born, D. Bortoluzzi, N. Brandt, M. Caleno, L. Carbone, A. Cavalleri, A. Cesarini, G. Ciani, G. Congedo, A. M. Cruise, K. Danzmann, M. de Deus Silva, R. De Rosa, M. Diaz-Aguiló, L. Di Fiore, I. Diepholz, G. Dixon, R. Dolesi, N. Dunbar, L. Ferraioli, V. Ferroni, W. Fichter, E. D. Fitzsimons, R. Flatscher, M. Freschi, A. F. García Marín, C. García Marirrodriga, R. Gerndt, L. Gesa, F. Gibert, D. Giardini, R. Giusteri, F. Guzmán, A. Grado, C. Grimaldi, A. Grynagier, J. Grzysch, I. Harrison, G. Heinzel, M. Hewitson, D. Hollington, D. Hoyland, M. Hueller, H. Inchauspé, O. Jennrich, P. Jetzer, U. Johann, B. Johlander, N. Karnesis, B. Kaune, N. Korsakova, C. J. Killow, J. A. Lobo, I. Lloro, L. Liu, J. P. López-Zaragoza, R. Maarschalkerweerd, D. Mance, V. Martín, L. Martin-Polo, J. Martino, F. Martin-Porqueras, S. Madden, I. Mateos, P. W. McNamara, J. Mendes, L. Mendes, A. Monsky, D. Nicolodi, M. Nofrarias, S. Paczkowski, M. Perreux-Lloyd, A. Petiteau, P. Pivato, E. Plagnol, P. Prat, U. Ragnit, B. Raïs, J. Ramos-Castro, J. Reiche, D. I. Robertson, H. Rozemeijer, F. Rivas, G. Russano,

- J. Sanjuán, P. Sarra, A. Schleicher, D. Shaul, J. Slutsky, C. F. Sopena, R. Stanga, F. Steier, T. Sumner, D. Texier, J. I. Thorpe, C. Trenkel, M. Tröbs, H. B. Tu, D. Vetrugno, S. Vitale, V. Wand, G. Wanner, H. Ward, C. Warren, P. J. Wass, D. Wealthy, W. J. Weber, L. Wissel, A. Wittchen, A. Zambotti, C. Zanon, T. Ziegler, and P. Zweifel. Sub-femto- g free fall for space-based gravitational wave observatories: Lisa pathfinder results. *Phys. Rev. Lett.*, 116:231101, 2016.
- [46] H Audley, K Danzmann, A García Marín, G Heinzel, A Monsky, M Nofrarias, F Steier, D Gerardi, R Gerndt, G Hechenblaikner, U Johann, P Luetzow-Wentzky, V Wand, F Antonucci, M Armano, G Auger, M Benedetti, P Binetruy, C Boatella, J Bogenstahl, D Bortoluzzi, P Bosetti, M Caleno, A Cavalleri, M Cesa, M Chmeissani, G Ciani, A Conchillo, G Congedo, I Cristofolini, M Cruise, F De Marchi, M Diaz-Aguilo, I Diepholz, G Dixon, R Dolesi, J Fauste, L Ferraioli, D Fertin, W Fichter, E Fitzsimons, M Freschi, C García Marirrodiga, L Gesa, F Gibert, D Giardini, C Grimaldi, A Grynagier, B Guillaume, F Guzmán, I Harrison, M Hewitson, D Hollington, J Hough, D Hoyland, M Hueller, J Huesler, O Jeannin, O Jennrich, P Jetzer, B Johlander, C Killow, X Llamas, I Lloro, A Lobo, R Maarschalkerweerd, S Madden, D Mance, I Mateos, P W McNamara, J Mendes, E Mitchell, D Nicolini, D Nicolodi, F Pedersen, M Perreux-Lloyd, A Perreca, E Plagnol, P Prat, G D Racca, B Rais, J Ramos-Castro, J Reiche, J A Romera Perez, D Robertson, H Rozemeijer, J Sanjuan, M Schulte, D Shaul, L Stagnaro, S Strandmoe, T J Sumner, A Taylor, D Texier, C Trenkel, D Tombolato, S Vitale, G Wanner, H Ward, S Waschke, P Wass, W J Weber, and P Zweifel. The lisa pathfinder interferometry—hardware and system testing. *Classical and Quantum Gravity*, 28(9):094003, 2011.
- [47] U. Denskat. Phasemeter Processing and Laser Control - S2-ASD-RS-3018. Technical report, Astrium, 2009.
- [48] LPF Team. Requirements for LTP equipment providers support in operations - S2-ESAC-RS- 5006, Iss. 1, Rev. 0, 19. Technical report, ESAC, 2012.
- [49] H. Audley et al. Laser assembly payload monitoring - Draft. Technical report, AEI, 2017.
- [50] H. Audley and A. Wittchen. Laser assembly payload monitoring plan. Technical report, AEI, 2016.